

Self-organized Criticality in Neural Networks by Inhibitory and Excitatory Synaptic Plasticity

Von der Fakultät für Mathematik und Informatik
der Universität Leipzig
angenommene

D I S S E R T A T I O N

zur Erlangung des akademischen Grades
DOCTOR RERUM NATURALIUM
(Dr.rer.nat.)

im Fachgebiet
Informatik
vorgelegt

von M.Sc. Masud Ehsani
geboren am 01.07.1990 in Mashhad (Iran)

Die Annahme der Dissertation wurde empfohlen von:
(1) Professor Dr. Jürgen Jost (MPIMIS Leipzig)
(2) Professor Dr. Jochen Triesch (Frankfurt Institute for Advanced
Studies)

Die Verleihung des akademischen Grades erfolgt mit Bestehen der Verteidigung am
22.11.2021 mit dem Gesamtprädikat magna cum laude.

Abstract

Neural networks show intrinsic ongoing activity even in the absence of information processing and task-driven activities. This spontaneous activity has been reported to have specific characteristics ranging from scale-free avalanches in microcircuits to the power-law decay of the power spectrum of oscillations in coarse-grained recordings of large populations of neurons. The emergence of scale-free activity and power-law distributions of observables has encouraged researchers to postulate that the neural system is operating near a continuous phase transition. At such a phase transition, changes in control parameters or the strength of the external input lead to a change in the macroscopic behavior of the system. On the other hand, at a critical point due to critical slowing down, the phenomenological mesoscopic modeling of the system becomes realizable. Two distinct types of phase transitions have been suggested as the operating point of the neural system, namely active-inactive and synchronous-asynchronous phase transitions. In contrast to normal phase transitions in which a fine-tuning of the control parameter(s) is required to bring the system to the critical point, neural systems should be supplemented with self-tuning mechanisms that adaptively adjust the system near to the critical point (or critical region) in the phase space.

In this work, we introduce a self-organized critical model of the neural network. We consider dynamics of excitatory and inhibitory (EI) sparsely connected populations of spiking leaky integrate neurons with conductance-based synapses. Ignoring inhomogeneities and internal fluctuations, we first analyze the mean-field model. We choose the strength of the external excitatory input and the average strength of excitatory to excitatory synapses as control parameters of the model and analyze the bifurcation diagram of the mean-field equations. We focus on bifurcations at the low firing rate regime in which the quiescent state loses stability due to Saddle-node or Hopf bifurcations. In particular, at the Bogdanov-Takens (BT) bifurcation point which is the intersection of the Hopf bifurcation and Saddle-node bifurcation lines of the 2D dynamical system, the network shows avalanche dynamics with power-law avalanche size and duration distributions. This matches the characteristics of low firing spontaneous activity in the cortex. By linearizing gain functions and excitatory and inhibitory nullclines, we can approximate the location of the BT bifurcation point. This point in the control parameter phase space corresponds to the internal balance of excitation and inhibition and a slight excess of external excitatory input to the excitatory population. Due to the tight balance of average excitation and inhibition currents, the firing of the individual cells is fluctuation-driven. Around the BT point, the spiking of neurons is a Poisson process and the population average membrane potential of neurons is approximately at the middle of the operating interval $[V_{Rest}, V_{th}]$. Moreover, the EI network is close to both oscillatory and active-inactive phase transition regimes.

Next, we consider self-tuning of the system at this critical point. The self-organizing parameter in our network is the balance of opposing forces of inhibitory and excitatory populations' activities and the self-organizing mechanisms are long-term synaptic plasticity and short-term depression of the synapses. The former tunes the overall strength of excitatory and inhibitory pathways to be close to a balanced regime of these currents and the latter which is based on the finite amount of resources in brain areas, act as an adaptive mechanism that tunes micro populations of neurons subjected to fluctuating external inputs to attain the balance in a wider range of external input strengths.

Using the Poisson firing assumption, we propose a microscopic Markovian model which captures the internal fluctuations in the network due to the finite size and matches the macroscopic mean-field equation by coarse-graining. Near the critical point, a phenomenological mesoscopic model for excitatory and inhibitory fields of activity is possible due to the time scale separation of slowly changing variables and fast degrees of freedom. We will show that the mesoscopic model corresponding to the neural field model near the local Bogdanov-Takens bifurcation point matches Langevin's description of the directed percolation process. Tuning the system at the critical point can be achieved by coupling fast population dynamics with slow adaptive gain and synaptic weight dynamics, which make the system wander around the phase transition point. Therefore, by introducing short-term and long-term synaptic plasticity, we have proposed a self-organized critical stochastic neural field model.

Acknowledgement

First and foremost I want to thank my advisor Jürgen Jost. He is both professionally and personally an inspiring character for me. I appreciate his style of supervision which has provided me with both the freedom to choose my research topic and the essential coordination to find my way in research. He has been supporting me in every aspect of my doctoral work and I am glad that I had the opportunity to work with him and learn from him. Our regular meetings and his lectures on different topics during every semester have been very instructive for me.

It has been an honor to be a member of Professor Jost's group and being surrounded by many experts on different topics which helped me to be exposed to many research topics and has broadened my view on mathematics and physics. I gratefully thank Pau Aceituno, Ivan Yamshchikov, and Zachary Adams for fruitful discussions during regular weekly meetings. I am grateful to all people in our group who were always welcoming for scientific discussions. In particular, many thanks to Armin Pournaki for proofreading parts of the thesis and his kind support and presence.

I acknowledge the financial support of the International Max Planck Research School "Mathematics in the Sciences". MPI MIS has been an excellent environment for me to pursue my doctoral studies. I am very thankful to Antje Vandenberg, Heike Rackwitz and Laura Pallagi for helping me with several personal and administrative tasks during my time at the institute. I am grateful to the librarians whose help always came faster than I imagined.

Lastly, I would like to thank my friends Navid, Fati, Farokh, Mahsa, Ina, Luise, and Armin for all the help during my years in Leipzig.

Contents

List of Figures	vii
1. Introduction	1
1.1. Scale-free Spontaneous Activity	2
1.1.1. Nested Oscillations in the Macro-scale Collective Activity	3
1.1.2. Up and Down States Transitions	5
1.1.3. Avalanches in Local Neuronal Populations	7
1.2. Criticality and Self-organized Criticality in Systems out of Equilibrium	9
1.2.1. Sandpile Models	9
1.2.2. Directed Percolation	11
1.3. Critical Neural Models	14
1.3.1. Self-Organizing Neural Automata	15
1.3.2. Criticality in the Mesoscopic Models of Cortical Activity	17
1.4. Balance of Inhibition and Excitation	21
1.5. Functional Benefits of Being in the Critical State	24
1.6. Arguments Against the Critical State of the Brain	25
1.7. Organization of the Current Work	25
2. Single Neuron Model	28
2.1. Impulse Response of the Neuron	30
2.2. Response of the Neuron to the Constant Input	34
2.3. Response of the Neuron to the Poisson Input	35
2.3.1. Potential Distribution of a Neuron Receiving Poisson Input	37
2.3.2. Firing Rate and Interspike intervals' CV Near the Threshold	45
2.3.3. Linear Poisson Neuron Approximation	52
3. Interconnected Homogeneous Population of Excitatory and Inhibitory Neurons	56
3.1. Linearized Nullclines and Different Dynamic Regimes	58
3.2. Logistic Function Approximation of Gain Functions	64
3.3. Dynamics Near the BT Bifurcation Point	70
3.4. Avalanches in the Region Close to the BT Point	75
3.5. Stability Analysis of the Fixed Points in the Linear Regime	77
3.6. Characteristics of Avalanches	81
4. Long Term and Short Term Synaptic Plasticity rules Tune the EI Population Close to the BT Bifurcation Point	87
4.1. Long Term Synaptic Plasticity by STDP Tunes Synaptic Weights Close to the Balanced State	87
4.2. Short-term plasticity and Up-Down states transition	91

5. Interconnected network of EI populations :Wilson-Cowan Neural Field Model	98
6. Stochastic Neural Field	105
6.1. Finite size fluctuations in a single EI population	105
6.2. Stochastic Neural Field with a Tuning Mechanism to the Critical State	110
7. Conclusion	114
Bibliography	117

List of Figures

1	Alpha oscillations show 1/f-like power spectra for their amplitude modulation	4
2	UP-down state transition in anesthetized rat recorded from somatosensory cortex.	6
3	Probability distribution of neural avalanche size.	8
4	Scaling Law for Avalanche Shape function.	9
5	Directed percolation in 1+1 dimensions	13
6	Firing condition for synchronuous excitation and inhibition input.	32
7	Minimum Excitation causing firing vs. stationary voltage level	34
8	Firing condition in case of delay between inhibition and excitation impulses	35
9	Output Firing rate in response to constant input.	36
10	Output firing and interspikes interval CV vs. Poisson input rates.	37
11	Diffusion Approximation of Poisson Input	39
12	Gaussian Approximation of membrane potential probability density	44
13	Output firing rate using Gaussian approximation.	44
14	Stationary Membrane Potential Variance	46
15	Membrane potential variance and mean evolution using τ -expansion.	47
16	CV of Interspike Intervals	52
17	Response of the neuron to the balanced current near the threshold.	53
18	Linear Poisson Neuron approximation.	54
19	Linearized gain functions and nullclines.	59
20	Nullclines' arrangements corresponding to different regimes of activity.	62
21	EI Nullclines in the case of Hopf Bifurcation.	63
22	EI simulation at the oscillatory regime.	63
23	Nullclines in the Saddle-node bifurcation case.	64
24	EI population:Asynchnous state.	65
25	Output rate near Saddle-node bifurcation point.	65
26	Output rate at threshold vs. input excitatory rate.	66

27	Nullclines at bifurcation points for the Logistic gain function.	68
28	Local bifurcation diagram using Logistic gain function.	70
29	Zoom in on the local bifurcation diagram.	71
30	Nullclines' arrangements near the BT point.	72
31	Phase space near BT points	74
32	Nullclines' configurations around avalanche dynamic region.	76
33	Avalanche style dynamics close to the BT point.(1)	77
34	Avalanche style dynamics close to the BT point.(2)	78
35	Stability of fixed points in the linear regime.	79
36	Frequency of avalanches.	82
37	Membrane potential track of a single neuron during the avalanche dynamics.	82
38	Avalanche characteristics(1).	83
39	Avalanche characteristics(2).	83
40	Phase Transition in EI population.	85
41	Phase Transition in the EI population(2).	85
42	STDP tunes synaptic weights.	90
43	Saddle-node and Hopf bifurcation in network with STP.	93
44	Population output in the network with STP	94
45	STP as a gain control mechanism.	94
46	Avalanche characteristics and Branching ratio in the final state of a network with STP.	95
47	Input-output function vs. STP curves.	95
48	EI population with STP.(2)	96
49	Nullclines plot in the network with STP.(1)	98
50	Nullclines plot in the network with STP.(2)	98
51	Final states of weights in the system with STDP satisfy condition for the Turing instability	102
52	Simulation of 20 interconnected EI population.	103
53	Nullclines' graphs for the system in the Poisson firing regime.	108
54	Characteristics of the network activity in the Poisson regime.	110
55	Variance of output population firing rate	111

1. Introduction

Neuronal networks show diverse activity patterns in different spatiotemporal scales such as oscillations, propagating waves and fronts, stable spatial Turing patterns, and avalanches. Based on the method of probing the activity, different aspects of the dynamics can be investigated in the presence or the absence of task-driven stimuli.

Experiments have shown that in the absence of stimuli, the cortical population of neurons shows rich dynamical patterns, called spontaneous activity, which do not look random and entirely noise-driven but are structured in specific spatiotemporal patterns. Spontaneous activity is assumed to be the substrate or background state of the neural system which is crucial for its function, i.e. processing information. This intrinsic brain activity has been recorded and analyzed in different spatial and temporal resolutions. Large-scale MRI recordings reveal highly coherent functional networks called resting states corresponding to spontaneous (not task-driven) brain activity. Microelectrode recordings, on the other hand, track the intrinsic activity in a small population of neurons. Altogether, experimental findings on different temporal and spatial resolutions highlight the scale-free characteristic of the spontaneous activity which we will discuss in detail.

Dynamic and functional characteristics of the spontaneous activity are connected to the structural architecture of the brain as well as the ongoing self-organization process. Through multi-scale neural modulations and plasticity, the dynamics of the neural network affects and shapes its structure and vice versa, the network structure coordinates the dynamics. The interplay of dynamics and structural organization on different spatiotemporal scales is coordinated and framed by multi-scale self-organization mechanisms that emerged in the organism during evolution. There exist opposing forces that shape the structure and activity such as excitation and inhibition currents produced by excitatory and inhibitory neuron types, depression and potentiation of the connection between neurons, modulation of the concentration of chemicals, and homeostatic consideration on energy consumption and information processing performance. As we will see later in this introduction, balancing and coordinating these opposing forces are considered to be one explanation for the scale-free characteristic of spontaneous activity.

Even micro-level local populations of neurons are never completely silent but are located in the state close to the phase transition from an inactive to an active state. Therefore, it is hypothesized that the brain organizes itself to be close to such a phase transition and spontaneous activity is the signature of this dynamical state. There exist several motivations besides experimental findings on the scale-free characteristic of spontaneous activity that makes this hypothesis appealing. On one hand, close to the edge of an active-inactive phase transition, local populations of neurons in the cortex would be in an idle state ready for processing information, but at the same time away from overactivation. On the other hand, close to the phase

transition, order parameter, a macroscopic state different from the inactive state, came into existence. The emergence of a macroscopic mode of activity acts as the coordinator of individual neurons which are enumerated in quantity and prone to various kinds of noise to produce a cooperative large-scale activity. Macroscopic states of activity, in turn, enslave the individual neurons. These active states in the spontaneous mode in the absence of meaningful information processing tasks can be seen as either a random sequence of active neurons or activation of a sequence of already inscribed patterns of co-activity in the connectivity map.

Being at the edge of an active-inactive phase transition requires a mechanism that prohibits the system from overloading. The presence of inhibitory currents that maintains a balance in the local neural populations besides general regulatory mechanisms that control the gain of the network can perform this job. The hypothesis is that the system is locally tuned to be in a specific dynamic range in local populations of neurons.

In this introduction, we try to shed light on three main questions. Firstly, what are the characteristics of the background activity in different spatio-temporal scales? Secondly, what model parameters or organizing mechanisms are responsible for the specific patterns of spontaneous activity? And finally, how and why the system is self organized to this regime of parameters and the corresponding patterns of activity?

We will start by presenting the experimental result in parallel with some of the most important modeling approaches which try to explain the corresponding phenomenon. Afterward, we present the idea of self-organized criticality and its relevance to brain dynamics. We present the canonical model of phase transitions from active to a single inactive state in non-equilibrium systems, namely the directed percolation universality class, and discuss how mesoscopic models of brain activity match the continuum field description of the directed percolation process close to the critical point. Finally, we discuss the self-tuning mechanism that is responsible for bringing the system close to the transition point.

1.1. Scale-free Spontaneous Activity. There exist different methods of recording activity with distinct resolutions and applications. Early investigations were conducted by surface electrodes known as electroencephalography (EEG) which record large-scale brain activity from the surface of the scalp. Similarly, in magnetoencephalography (MEG), magnetic fields produced by neuronal currents are recorded, which is known to produce activity maps with higher spatial sensitivity compared to EEG. Moreover, the Functional Magnetic Resonance Imaging (fMRI) method detects changes and contrasts in the blood flow to different regions of the brain by using blood-oxygen-level-dependent (BOLD) signals to probe the neural activity. Although it suffers from a poor temporal resolution, fMRI enables us to noninvasively record the activity of deeper areas of the brain which has been used excessively for studying brain functional maps. Researchers also

use thin microelectrodes or microelectrode arrays to record the activity of a single neuron or a group of them by tracking voltage change in the extracellular environment. Local Field Potential (LFP) recordings by implanted micro-electrodes arrays track the electric potential in the extracellular region within the cortical tissue. Besides, more recent optical methods such as calcium imaging are being used to record the activity or inhibit/activate a selected number of neurons. Experiments are either conducted in vivo or in cultured slices of brain tissue in vitro. Spontaneous activity is recorded and analyzed through all these methods. In the following, we will present some of the most relevant experiments and modeling approaches.

1.1.1. *Nested Oscillations in the Macro-scale Collective Activity.* When recorded by coarse-grained methods like EEG and MEG, spontaneous brain activity shows nested oscillations with a power spectrum that indicates scale-free properties, i.e. $P(f) \propto 1/f^\beta$. In the paper by Linkekaer-Hansen et al. [1], amplitude modulation of alpha oscillation was shown to have $1/f^\beta$ power spectra with $\beta \approx 0.5$, reflecting the lack of a characteristic time scale for the duration of oscillation, see Fig.1. Furthermore, the auto-correlation of the MEG and EEG signals are reported to decay by power-law $AC(t) \approx t^{-\gamma}$. In Miller et al. [2], a power-law spectral density with exponent -2.5 below 80 Hz and with a transition to $1/f^4$ scaling above this frequency is reported.

Moreover, the scale-free character of neuronal oscillations, i.e. self similarities in time series of neural activity, has been studied by Detrended Fluctuation Analysis (DFA) of EEG/MEG data in Hardstone et al. [3]. Self-similarity can be seen as power-law scaling of fluctuations. Consider that the mean standard deviation of the signal calculated in the time window of Δt scales as $\sigma(L\delta t) = L^H \sigma(\delta t)$. Here, H is called the Hurst exponent and it indicates the strength and type of correlation in the time serie. The value of $H = 0.5$, in this case, means that the process has no memory and it has neither correlation nor anticorrelation in time. Values of $0 < H < 0.5$ indicate anti-correlation and $0.5 < H < 1$ is associated with the process having memory and temporal correlations. DFA applied to the envelop of the alpha band (8-13 Hz) filtered EEG signal, shows long-range temporal correlations with $H \approx 0.71$ [3] [1]. It implies that at the critical point, correlations extend over long distances and decay more slowly.

Neural oscillations spontaneously generated by the brain show large frequency, amplitude, and duration variabilities. To investigate this fact, Kitzbichler et al. [4] obtained approximations for the probability density of phase lock intervals (PLI) between pairs of fMRI and MEG signals. The phase difference of two time series is calculated by using Hilbert transforms. Locking intervals are defined as periods where this phase difference is lower than a threshold. The authors have found that $P(PLI) \approx PLI^{-\alpha}$ with $\alpha \approx 3$. The variability of the synchronization in the spatial domain can also be calculated by considering the distribution of the difference in the

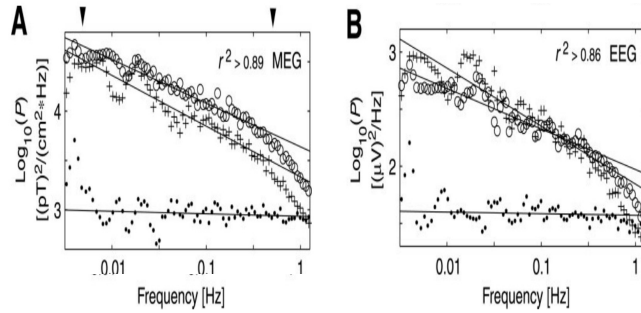


FIGURE 1. The grand averaged ($n = 10$) power spectral density of alpha rhythm amplitude fluctuations are plotted in double-logarithmic coordinates for MEG (A) and EEG (B) data. Circles, Eyes-closed condition. Crosses, Eyes-open condition. The dots represent the reference recording and the surrogate data for the MEG and EEG power spectra, respectively. Arrowheads mark the interval used for the estimation of slopes. From Linkenkaer et. al Linkekaer-Hansen et al. [1].

number of phase-locked time series at two distinct points in time. Oscillations in the coarse-grained data reflects an optimal level of synchrony in the population of neurons, a scale-free behavior, a high variability in the level of synchrony, and long-range correlations both in time and space through local interactions. These can be taken as signs for being close to the onset of synchronization, i.e. a critical phase transition separating synchronized and non-synchronous states. Medium level of synchrony has been shown to play a crucial role in the information transmission and processing [5]. For example, the level of synchrony in the gamma band (20-80Hz) is higher during task-driven activity [6]. On the other hand, a high level of synchrony can cause persistence of activity and epileptic seizures. Therefore, being at the threshold of synchronization enables the network to switch between synchronized and desynchronized states.

One way to model synchronization in the brain is by identifying local populations of excitatory and inhibitory neurons as nonlinear oscillatory building blocks which are connected to each other to form a larger network of coupled oscillators. Each interconnected population of inhibitory and excitatory neurons can generate oscillations due to delay in synaptic transitions between inhibitory and excitatory feedbacks or even, in the absence of delay, through the Hopf bifurcation of the quiescent state. Considering periodic activity at each local EI block, one can define ϕ_i as the phase of the i_{th} oscillator with uncoupled intrinsic frequency ω_i . A phase model for coupled oscillators would assume that the connection strength among oscillators depends on their phase difference. Considering the case that the strength of

the connection between oscillators is homogenous, one can write down the evolution of the phase of the i_{th} oscillator as :

$$\dot{\phi}_i = \omega_i + \frac{R}{N} \sum_k J(\phi_k - \phi_i) \quad (1.1)$$

This is the Daido model for weak coupled oscillators [7, 8]. R denotes the strength of connections between oscillators and intrinsic frequencies, ω_i , are drawn from a probability density function, $g(\omega)$, with the mean value $\bar{\omega}$. Moreover, suppose J is an odd function with Fourier expansion $J(\theta) = \sum_n a_n \sin(n\theta)$. A synchronous state would emerge if R is strong enough and if there is a positive a_n . In this case, an asynchronous state destabilizes at $R_c = \frac{2}{\pi g(\bar{\omega}) a_n}$. When the intrinsic frequency distribution is uni-modal, at $R = R_c$, the system shows a second order phase transition.

The Kuramoto model with a simple sinusoidal coupling function (J) is the simplest model for coupled oscillators. Meisel et al. [10] showed the Kuramoto model to have a PLI power-law probability density at $R = R_c$. Moreover, fluctuations in the Kuramoto order parameter peak at this point. Gong et al. [9] and Meisel et al. [10], have reported the same power-law PLI distribution in the awake brain.

1.1.2. *Up and Down States Transitions.* Another phenomenon observed in the spontaneous activity is the alternation between low rate firing states (Up-states) and periods of quiescence (Down-states). In Steridae, et al. [11] intra-cellular and EEG recordings in cats during slow-wave sleep(SWS), awake, REM sleep, and anesthetized states showed patterns of oscillations of the membrane potential between these up and down states. The SWS state is distinguished from both waking and REM sleep by the presence of cyclic, long-lasting (0.3–0.5 s), and high-amplitude (8–20 mV) hyperpolarizations during which neurons do not fire. In another in-vivo experiment, Hahn. et al [12] showed that hippocampus interneurons membrane potential in anesthetized mice shows $\approx 0.5 - Hz$ up-down state oscillations. This slow oscillation occurs in cortical slices in vitro as well [13], which suggests cortical EI populations are intrinsically able to generate slow oscillations.

In Compte et al. [14], authors have proposed that the competition between the buildup of outward conductances, such as Ca^{2+} and Na^+ -activated K^+ currents and positive feedback of excitatory neurons is responsible for the Up-down state transition. The transition from Up-state to down-state is attributed to the opening up of slow Na-dependent K^+ conductance which generates slow negative activity-dependent feedback. Therefore, the periodicity of the slow oscillation is determined largely by the balance between the recurrent excitation and inhibition inherent in cortical networks, and the time course of the outward currents which generate the slow hyperpolarization. Recurrent excitation produces bi-stability in the network in response to current injection to the cell and k^+ current switches the state

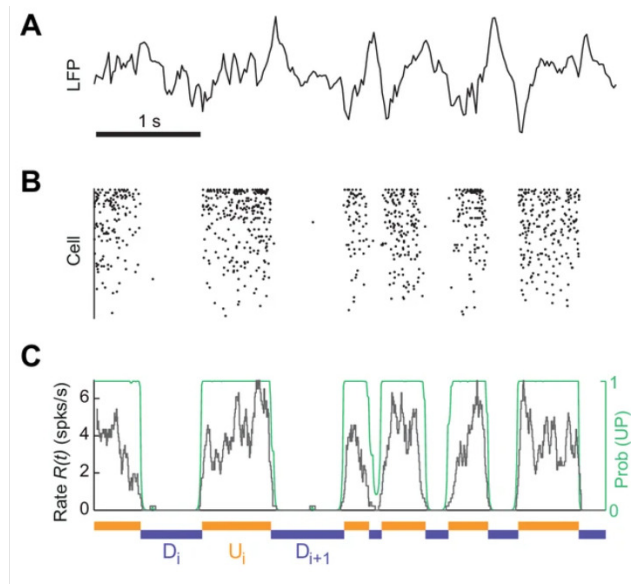


FIGURE 2. (A) 5 second local field potential(LFP) signal (B) Raster plot for activity of 96 single neurons (C) Instantaneous population rate. From Jercog et.al [19].

of the system. In another in-vitro experiment on cortical slices using two-photon calcium imaging, Cossart et.al. [15] found that the Up-state happens as synchronized activity in an ensemble of neurons. In asleep and awake animals in-vivo the Up-state resembles a synchronous firing state with constant population activity and irregular single neuron firings. It has been known that low-frequency oscillations are related to sleep or inattentive states while high-frequency oscillations are usually attributed to information processing. Therefore, in the absence of stimuli, neural circuits should have the capacity of low-frequency oscillations and up-down states transitions. Kenet et al. [16] showed that spontaneous activity in the part of the cat visual cortex responsible for the orientation selectivity is composed of spontaneously occurring states that correspond to cortical representations of orientations. This leads to the hypothesis that during Up-states, cortical populations wander around established activity patterns. Although experimental studies presented so far reported rhythmical oscillatory alternations of up-down states, there exist other studies which indicate that during light anesthesia or awareness these transitions are much more variable and random, [17, 18] (see Fig.2).

There exist many computational models for Up-Down states transitions mostly based on either network bistability of quiescent and low (or high) firing states, [19–22], or bistability of voltage based current to individual neurons [23]. In the first case, the network switches between the mentioned states either by finite-size internal fluctuations or by the slow change of a model parameter mainly due to depression of synapses or both of

these mechanisms. In Milman et.al [21], short-term plasticity of excitatory synapses leads to a switch between high firing fixed point and quiescent state in a population of excitatory neurons. In this model, during the Up-state, the branching parameter is close to one and the firing rate is approximately 80 Hz. Therefore, the Up-state is critical and the Down-state is sub-critical. Tartaglia et al. [22] investigated the bi-stability of the low firing state and quiescent state in an Excitatory-Inhibitory population in a balanced network and showed that adaptive excitatory current leads to a switch between these two fixed points. Similarly, Jercog et al. [19] studied EI networks in the inhibition-dominated regime with a focus on external input fluctuations as the source for irregular transitions of Up and Down states.

In summary, Up-down transitions might indicate that the system resides near a bi-stable regime. On the other hand, without a self-regulating mechanism, bi-stable states should be close to each other in phase space so that stochastic transition or minimal regulatory effects cause the switch among them. This can serve as another motivation to consider neural systems close to a critical point, i.e. a saddle-node bifurcation that generates separate fixed points close to each other.

1.1.3. *Avalanches in Local Neuronal Populations.* Apart from oscillatory and wave-like activity patterns, in microcircuits of the brain during spontaneous activity, we observe avalanche dynamics. This mode of activity was first closely investigated by Beggs and Plenz [24] in cultured slices of the rat cortex by using a multi-electrodes array with an inter-electrode distance of $200 \mu\text{m}$ to record local field potentials(LFP). An avalanche is defined as almost synchronized epochs of activity usually separated by long periods of inactivity. At higher temporal resolutions, these seemingly synchronized patterns appear as cascades of activity in micro-electrodes array initiated from one (or few) local sites that propagate through the network and finally terminate. To define avalanche from LFP data, they have binned the signals of the whole electrode. Avalanches are identified as the cascade of events between quiescent time bins. The size of an avalanche is then measured as the total number of micro-electrodes with LFP peaks during that avalanche. It must be noticed that activity does not spread in a wave-like manner, i.e. activity in one site is not necessarily preceded by the activity of nearest neighbors. The main finding of this seminal experimental paper is the power-law scaling of the probability density function of size and duration of avalanches, see Fig.3. Furthermore, they have found that the application of excess excitatory-inhibitory provoking drugs destroys the power-law scaling. Further studies approve these results in different setups such as awake monkeys (Petermann.et.al. [25]), cerebral cortex and hippocampus of anesthetized, asleep, and awake rats(Ribeiro et al. [26]) and visual cortex of anesthetized cat (Hahn et al. [27]). Besides LFP data, several studies reported the scale-free avalanche size distribution based on the spike data such as Friedman et al. [28], Hahn et al. [27], Mazzoni et al. [29]. Friedman

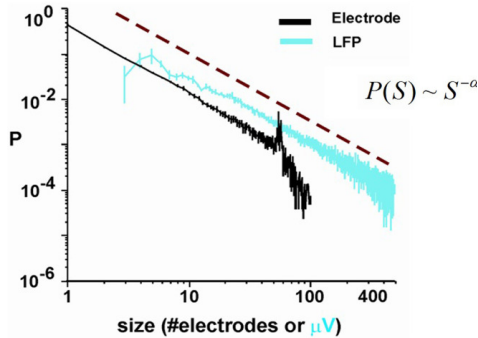


FIGURE 3. (Black) The size of avalanche is defined by the total number of activated electrodes during avalanches and in (Blue) size measures from LFP amplitude. From Beggs and Plenz,2003. [24]

et al. [28] analyzed cultured slices of the cortical tissue and collected data at individual neurons with different spacings. Besides power-law scaling of size and duration of avalanches with exponents $\tau \sim -1.5$ and $\alpha \sim -2$, respectively, they showed that the temporal profile of avalanches is described by a single universal scaling function. The average size versus average duration of avalanches is also a power-law with $\langle s \rangle = \langle T \rangle^\delta$ with a scaling relation between critical exponents as $\frac{\tau - 1}{\alpha - 1} = \delta$. Besides, the mean temporal profile of avalanches follows a scaling form as in non-equilibrium critical dynamics :

$$S(t, T) \sim T^{\delta-1} F(t/T) \quad (1.2)$$

They showed that their data sets collapse to the above scaling function, see Fig.4. Scaling relations suggest stronger evidence for critical dynamics as an explanation for the power laws observed in the observables of the system. In another paper by Klaus et al. [30], it has been shown that power law is the best fit for neural avalanches collected from in vivo and in vitro experiments.

Karimpanah et al. [31] investigated how stimulus might change the scale-free behavior in vivo experiments in the primary visual cortex of mice during visual stimulation. They found out that avalanche size and duration distributions, under three different stimuli conditions, show the same critical exponents. However, spatiotemporal patterns of activity as measured by pairwise cross-correlation are different among these stimulation setups. This study suggests that the system operates near criticality even in the presence of the stimulus. Spontaneous activity is modulated negligibly by stimulus, although it is responsible for the observed variability in the response. Tetzlaff et al. [32] analyzed how synaptic modification in developing neural networks in vitro tunes the system close to the critical regime. In the synaptic growth phase, activity will increase, new synapses appear and the

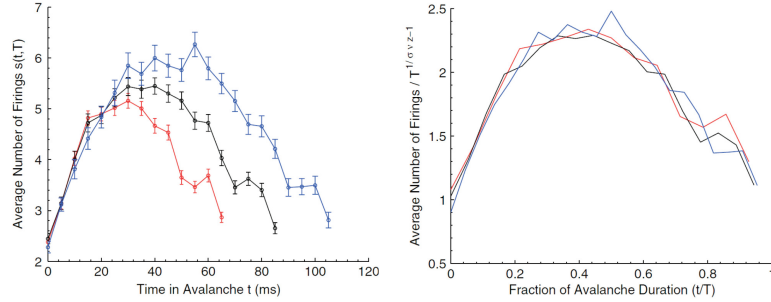


FIGURE 4. (Left) Average avalanche shape for avalanches of three different durations.(Right) Scaled avalanche shape collapses to the scaling function of equation (1.2). From Friedman et al.2012 [28].

system shows supercritical behavior, however by pruning of synapses the system will reach a critical state at a low firing rate state.

The appearance of power laws, scaling relations among their exponents, data collapse, and sensitivity to the imbalance of excitation and inhibition led to the hypothesis that the brain is somehow poised near criticality by a self-organization mechanism with the balance of excitatory and inhibitory rates as the self-organizing parameter. In the following, we will discuss the concept of self-organizing to a critical state in physical systems and introduce the canonical universality class of phase transitions to a single absorbing state, namely directed percolation.

1.2. Criticality and Self-organized Criticality in Systems out of Equilibrium.

1.2.1. *Sandpile Models.* Self-organized criticality in sandpile models was first introduced by Bak and Tang [33]. Consider a system of n threshold elements on a d -dimensional lattice, for example, a sand pile with a discrete number of sand grains on discrete sites. We assign a parameter like height at each point which has discrete values $0 \leq h_i \leq m$. Dynamics on the lattice is driven by two mechanisms, external driving in the form of adding sand grains to an arbitrary randomly chosen site and internal relaxations, i.e. when the height of sand column at a site becomes greater than a threshold value then it would release one grain to each of its neighbors. Consider an open boundary, which means sand relaxation at the boundary leads to the dissipation of sands. Self-organized criticality hypothesizes that if we start the dynamics on the lattice from any initial configuration of heights, the interplay of loading and relaxation will self-organize the system to a critical state. At this state, upon adding external sand to arbitrary sites, cascades of relaxations occur in the neighboring sites, i.e. avalanches. They reported power-law distributions of size and duration of avalanches. Numerical simulation in 2D resulted in $D(s) \approx s^{-\tau}$, $\tau \approx 1$ and $D(t) \approx t^{-\alpha}$, $\alpha \approx 1$.

After relaxation, the system lands in one of the meta-stable inactive configurations. The important point is that the critical state is independent of the initial configuration and no fine-tuning is needed for critical behavior. The authors originally introduced this model as a mechanism to generate $1/f$ noise and claimed that in case that the time scale of the driven force is much larger than the time scale of relaxation dynamics, superposition of random events generates a $1/f$ power spectrum. However, this claim was refuted in Jensen et al. [34]. There, it has been shown that the linear superposition of signals from avalanches starting at random times leads to spectrum falling off like $1/f^2$. In Manna(1991) [35], critical exponents for sandpile models based on height and slope in two dimensions are obtained on larger data sets and with smaller errors.

In the sandpile models discussed above, avalanches are deterministic. In another viewpoint, avalanches can be produced as realizations of a branching process with a stochastic dynamics. In a branching process each active node(ancestor) reproduces n number of descendants with probability $p(n)$. The average number of descendants of a single active node is called branching ratio, $\sigma = \sum_n np(n)$. When $\sigma > 1$, the probability of an infinite size avalanche is non-zero. On the other hand, for $\sigma < 1$, avalanches are finite and for the marginal value $\sigma = 1$, avalanche size is power-law distributed with $P(s) = s^{-3/2}$ and $P(t) = t^{-2}$. In Zapperi et al.(1995) [36], a simple self-organizing branching process is introduced in which the branching parameter is self tuned to critical value with update dynamics for σ by counting the number of descendants reaching an arbitrary boundary at the k generation of avalanches.

In Bak et al.(1998) [37], the authors derived exponents analytically for a mean-field model of sandpile dynamics which matches critical branching process exponents. It has been shown that for cellular automata of sandpile models to show scale invariance, two ingredients are necessary: time scale separation between load and relaxation and local conservation law, i.e. no dissipation of sands during avalanches [38–40].

The relation of the self-organizing of BTW and Manna models to normal forms of critical dynamics, especially to absorbing state phase transitions has been explored in recent years. The absorbing state is a quiescent state that the system settles in and cannot escape from because internal fluctuations are zero in the absorbing state. Directed percolation is the canonical universality class for phase transitions into a single absorbing state which we will discuss briefly later. The sandpile model of BTW resembles a system with an infinite number of micro-state absorbing states to which the system relaxes after producing an avalanche. Avalanches occur by an external drive that transfers the system from one absorbing state to another. However, at first sight, there is a fundamental difference between ordinary absorbing state phase transitions and SOC. For a system to show absorbing phase transitions, we need fine-tuning of control parameters, however, in SOC models like BTW sand pile, there is a self-tuning mechanism that

brings the system to a critical point implicit in the description of the dynamics of the system. Based on this fact SOC in BTW or Manna model was not automatically categorized in the DP universality class. Several types of research have been conducted to study the relation of self-organized criticality to well-established dynamical criticality models.

Vespignani et al. [41] introduced a model of absorbing state phase transition coupled to a conservation field with separation of time scales that shows self-tuning to criticality. There exists a critical density of sands, ρ_c , above which the active state survives, while below this critical level, the system's activity would decay and it reaches a stable inactive configuration.

Similarly, Dickman et al. [42] linked SOC with DP by equipping a model of absorbing-state phase transitions, with the method for forcing the model to its critical point, by adding (removing) particles when the system is frozen (active). They concluded that in the limit of slow drive and slow removal (i.e. time scale separation), the system shows SOC behavior. Therefore, the SOC mechanism in sandpile models is not inherently distinguished from well-known continuous absorbing state phase transitions in the sense that likewise in the BTW sandpile model there is a fine-tuning of the order parameter which in this case is the vanishing rate of an external drive ($h \rightarrow 0^+$). Following this line, one can formally write down conservative sandpile models as the mesoscopic Langevin equation of DP coupled with conserving energy field. In this case, the universality class of this SOC type dynamic is of C-DP (conserving directed percolation) type [43].

In the following subsection, we introduce the DP model and its critical behavior which is of particular importance for our upcoming neural critical models.

1.2.2. Directed Percolation. The directed percolation universality class has been claimed to describe many non-equilibrium systems showing dynamic criticality. DP belongs to a larger class of critical open systems called absorbing state phase transitions. An absorbing state is a steady state in which there are no internal fluctuations and therefore, the system can not escape from it. Continuous phase transitions to a unique absorbing state fall generically in the universality class of directed percolation. To be more precise, the existence of more than one absorbing state does not automatically destroy the DP conjecture. Non-DP critical behavior appears only if there is symmetry among different absorbing states.

The simplest microscopic model of DP is a binary creation, annihilation and diffusion on a lattice. Particles diffuse with rate D to neighboring site, $A + 0 \rightarrow 0 + A$, coagulate with rate κ , $A + A \rightarrow A$, reproduce with rate λ , $A \rightarrow A + A$ and spontaneously decay with rate σ , $A \rightarrow 0$.

The mean field equation for the average density of particles corresponding to the above reaction-diffusion process, ignoring spatial inhomogeneities in the field and considering the average field as $a(t)$ can be written as follows:

$$\frac{da(t)}{dt} = (\lambda - \sigma)a(t) - \kappa a^2(t)$$

Considering diffusion and defining $a(x, t)$ as the local mean density of activity and ignoring fluctuations around this mean value, the density field obeys:

$$\frac{\partial a(x, t)}{\partial t} = (\lambda - \sigma)a(x, t) - \kappa a^2(x, t) + D\Delta a(x, t)$$

As can be seen already from the above mean field equation at $\sigma = \lambda$ a phase transition occurs. For $\sigma < \lambda$, the system approaches the inactive state with the trend $a(t) \sim e^{-(\lambda-\sigma)t}$. For $\sigma > \lambda$, there would be an active state of density $a_\infty = \frac{\sigma - \lambda}{\kappa}$. At the balanced state, when production and decay rates are equal, the equation reads as :

$$\frac{da(t)}{dt} = -\kappa a^2(t)$$

and initial state of a_0 will decay as $a_0 t^{-1}$.

Including reaction noise to the above field, the equation would require careful integration of microscopic fluctuations. One possible way is through the functional representation of the microscopic master equation through the coherent state path integral formalism [44, 45]. This procedure ends up in an effective action describing the directed percolation universality class also known as Reggeon Field Theory. Reggeon Field theory can be interpreted as the Janssen-De Dominicis response functional, which is formally equivalent to the following Langevin description of directed percolation close to the absorbing phase transition [46, 47]:

$$\begin{aligned} \frac{\partial a(x, t)}{\partial t} &= ra(x, t) - \kappa S^2(x, t) + D\Delta S(x, t) + \psi(x, t) \\ < \psi(x, t)\psi(x', t') > &= 2na(x, t)\delta(x - x')\delta(t - t') \end{aligned} \quad (1.3)$$

where $r := \lambda - \sigma$.

The variance of the noise is proportional to the field strength. This reflects that the number of creations and annihilations of particles at any point are Poisson random variables. To investigate the relevance of the noise in large-scale dynamics we have to study the scaling behavior of the system under coarse-graining of space and time. In the renormalization process, we adjust the parameters of the system under coarse-graining of length scales to keep the physical description of it unchanged. Applying coarse-graining and renormalizing parameters leads to a flow in parameter space which is called renormalization flow. Fixed points of the renormalization flow are critical points of the system in which the system is unchanged by scaling transformation and therefore shows scale invariance. Based on the scale

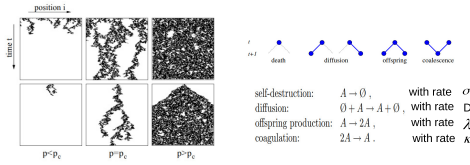


FIGURE 5. Directed bond percolation in 1(spatial)+1(temporal) dimensions starting from a random initial configuration of active sites (top) and from a single active seed (bottom). From Hinrichsen 2000, [48]

transformation of parameters, which themselves are coefficient of interaction or noise terms, close to renormalization fixed point, we can define the relevance of the corresponding terms in the dynamics. Suppose upon coarse-graining by $x \rightarrow \Gamma x$ and $t \rightarrow \Gamma^\eta t$ a coefficient scales as $c \rightarrow \Gamma^\eta c$, then the corresponding dynamic term would be relevant, irrelevant or marginal if $\eta > 0$, $\eta < 0$ or $\eta = 0$, respectively.

In the mean field approximation, the Langevin equation (1.3) might be renormalized by a scaling transformation $x \rightarrow \Gamma x, t \rightarrow \Gamma^z t, a(x, t) \rightarrow \Gamma^{-\xi} a(\Gamma x, \Gamma^z t)$ where z denotes the dynamic exponent. Under these transformations, the parameters of the model scale as:

$$r \rightarrow \Gamma^z r, \quad \kappa \rightarrow \Gamma^{z-\xi} \kappa, \quad D \rightarrow \Gamma^{z-2} D, \quad n \rightarrow \Gamma^{z+\xi-d} n$$

Therefore, at the critical point, $r = 0$, the Langevin equation(1.3) is scale-invariant by assigning $z = 2$ and $\xi = 2$. Thus, the noise amplitude n scales as $n \rightarrow \Gamma^{4-d} n$, where d is the spatial dimension. Approaching the fixed point, the noise amplitude may diverge, vanish or stay finite, corresponding to $d < 4$, $d > 4$ and $d = 4$, respectively. we refer to the value of d where the noise becomes marginal as the upper critical dimension, d_c . For the directed percolation model, the upper critical dimension is $d_c = 4$. Furthermore, higher-order interaction terms like a^3 and $\Delta^2 a$ are irrelevant at the critical point under coarse-graining.

In a non-equilibrium system showing scale invariance at a continuous phase transition, universal scaling laws emerge. In the mean-field DP analysis, the density in the active phase close to the critical point, $r_0 = 0$, reaches $a_{stat} = |r - r_0|^\beta$, where β is a universal exponent and in our case $\beta_{MF} = 1$. In the inactive phase, the density would decay as $a = e^{-|r-r_0|t} \sim e^{-t/\xi_T}$ where ξ_T is correlation length of temporal dimension and scales as $\xi_T = |r - r_0|^{-\nu_T}$. In the mean field approximation of DP, $\nu_T^{MF} = 1$. In contrast to equilibrium critical phenomena, in non-equilibrium phase transitions two independent correlation lengths for temporal(ξ_T) and spatial(ξ_S) dimensions are present in the system. These values are respectively proportional to average lifetime and lateral size of an avalanche started from a single seed at time $t = 0$. Close to the critical point, correlation lengths diverge with different exponents for spatial and temporal dimensions which

are related to the dynamic exponent z as $\nu_T/\nu_S = z$. Therefore, $\nu_s^{MF} = \frac{1}{2}$ for DP.

Scale invariance and divergence of spatial and temporal correlation lengths can be used to derive general scaling laws for observables of the system. Critical exponents for other observables can be derived by aforementioned independent exponents (β, ν_T, ν_s) . For example, the mean size of an avalanche (total number of activated sites) in the inactive phase scale as $\langle S \rangle = (r - r_c)^{-(\sigma - \nu_T)}$ with $\sigma = (z + d)\nu_s - \beta$ or the stationary density in response to external field of creation of particles with rate h scales as $a_{stat} = h^{\beta/\sigma}$. Moreover, the avalanche size density obeys a power-law as $P(s) = s^{1-\tau}$ with $\tau = 2 + \frac{\beta}{\sigma}$. In the mean-field approximation of DP, $\sigma = 2$ and $\tau = 5/2$. Furthermore, the mean field power spectrum follows a power-law decay, $f(\omega) = \omega^{-2}$. It is worth noting that the mean field exponents of self-organized sand pile models and the critical branching process coincide with the critical exponents of the mean-field DP.

In $d \leq 4$ where noise is relevant, critical exponents differ from the mean field exponents and the fluctuation effect is strong enough to affect power-laws near critical point. To investigate critical behavior, in $d < 4$ we have to follow the renormalization process. With the simple re-scaling, $S(x, t) = \sqrt{\frac{\kappa}{\sigma}} a(x, t)$, and introduction of $u = \sqrt{\sigma\kappa}$, Langevin equation(1.3) can be rewritten as:

$$\begin{aligned} \frac{\partial S(x, t)}{\partial t} &= -D(r - \Delta)S(x, t) - uS^2(x, t) + \psi(x, t) \\ \langle \psi(x, t)\psi(x', t') \rangle &= 2uS(x, t)\delta(x - x')\delta(t - t') \end{aligned}$$

Integrating fluctuation and nonlinear interaction terms proportional to u produces infrared divergent terms in one-loop corrections to two-points and three points vertex functions at the critical point for $d < d_c$. Same terms produce ultraviolet divergence in the perturbation expansion at $d > d_c$. Therefore, at $d = d_c$ both UV and IR divergences are combined in the logarithmic singularities. The standard approach of renormalization is to absorb artificial UV singularities of the model(in the limit that lattice spacing goes to zero) into renormalized parameters and study their flow under coarse-graining to obtain a renormalization group equation. Fixed points of RG flow equations are the critical points and linearizing RG flow near this fixed point determines critical exponents. For $d < 4$ defining $\epsilon = 4 - d$, critical exponents are as follows :

$$\beta = 1 - \frac{\epsilon}{6} + O(\epsilon^2), \quad \nu_S = \frac{1}{2} + \frac{\epsilon}{16} + O(\epsilon^2), \quad \nu_T = 1 + \frac{\epsilon}{12} + O(\epsilon^2)$$

1.3. Critical Neural Models.

1.3.1. *Self-Organizing Neural Automata.* Neural avalanches might resemble sandpile models with the burst-like sudden release of energy and transmission of activity to neighboring sites when their membrane potential is being raised above a certain threshold. Neurons play the role of site elements that receive both external and internal input. The membrane potential of the neuron is usually taken as the energy variable. Upon reaching a voltage threshold, the neuron resets and sends input to its neighboring neurons. [49–51]. Eurich et al. [51] modeled globally coupled threshold elements driven by external noise with time scale separation between the internal relaxation and the driven force. Internal input to all elements is proportional to the number of active neurons, $I_i(t) = \frac{\alpha V}{N} M(t-1)$, where α is the coupling strength, V is the threshold above which neuron fires and $M(t-1)$ is the number of active neurons at time $t-1$. At critical coupling strength, $\alpha_c \approx 1 - N^{-\mu}$, which corresponds to a conservative model, the avalanche size obeys a power-law, $P(L, \alpha_c) = L^{-\eta} \exp(-L/\gamma)$ with $\eta = -3/2$, with system-size dependent cut-off. Here, the avalanche dynamic is deterministic and the only stochasticity in the model arises from the random arrival of the external input at a randomly selected site. Larremore et al. [52] investigated avalanches in a stochastic binary network by assigning matrix element, A_{nm} , to the probability that node m becomes activated at time $t+1$ if node n is active at time t . They have shown that if the largest eigenvalue of A is exactly one, the size and duration distributions of avalanches are power-laws with branching process exponents.

To tune the system at the critical point, many modeling approaches and adaptive mechanisms have been suggested during the decades of research on critical brain hypothesis. A SOC model for a non-conservative neuronal model that attracted much attention is introduced by Levina et al. [53, 54]. They have claimed that self-organization by short-time synaptic plasticity drives the system to the critical regime. They used excitatory neurons with separation of time scale for the external drive and the membrane potential dynamics. Dynamics of globally coupled integrate and fire neurons with $0 \leq V_i \leq 1$ as the internal state parameter and synaptic strength J_{ij} between neurons i and j follow:

$$\begin{aligned} \frac{dV_i}{dt} &= \sum_j \frac{uJ_{ij}}{N-1} \delta(t-t_s^j) + I^{Ext} \delta(t-t_{Ex}^i) \\ \frac{dJ_{ij}}{dt} &= \frac{1}{\tau_j} \left(\frac{\alpha}{u} - J_{ij} \right) - uJ_{ij} \delta(t-t_s^j) \end{aligned} \quad (1.4)$$

Here, I^{Ext} is the external input to cell i at random moments t_{Ex}^i . Each neuron upon firing at the threshold value $V = 1$ resets to $V = 0$ while increasing membrane potential of other $N-1$ neurons by the amount of $\frac{uJ_{ij}}{N-1}$. After each spike of neuron j , the weight of outgoing synapses

is depressed by the amount of uJ_{ij} , which recovers toward the value $\frac{\alpha}{u}$ with the time constant τ_j . In the static regime ($\tau_j \rightarrow 0$), J_{ij} reaches its maximum value $\frac{\alpha}{u}$. The average size of the avalanche is calculated to be $\langle s \rangle = \frac{1}{1 - uJ}$. Defining $uJ = \alpha_{static}$, at value $\alpha_{static} = 1$ in the static limit, which corresponds to the conservative dynamic, system shows scale free avalanches as a sign for critical dynamics.

In the case of dynamical synapses (i.e. slow synaptic recovery time), they showed that the population average of synaptic strength, $u\bar{j}$, is self tuned by the coupled dynamics of equation (1.4) to values around one, which makes the system critical for any $\alpha > 1$. Therefore, using the mean-field equation for self-consistency for the average firing rate and the average synaptic strength, they showed that STP can cause the average utility to be close to the critical point for a wide range of maximum utility α and it leads to a branching ratio very close to 1 in a large area of phase space.

In addition to self-organization by short-term depression in synapses which is also used in Peng et.al. [55] and di Santo et al. [56], self-organization by other control parameters like degree of connectivity or synaptic strength has been studied. Adaptive rewiring of asymmetric synaptic connections with fixed strength ($J_{ij} = \pm 1$) by the average input correlation was introduced in the spin models of neural networks [57, 58]. In these works, the authors have claimed that insertion and deletion of the links based on adaptive rewiring regulate the network toward criticality by tuning the branching ratio to unity.

In line with the methods used in mentioned articles, Meisel and Gross [59] introduced a self-organizing neural network by STDP. In Brochini et al., [60] self-organization in stochastic spiking neuron model by short term plasticity of the gain function instead of synaptic weights is introduced. Benayoun et al. [61] proposed a model composed of stochastic single neurons which shows avalanche dynamics in the regime of closely balanced input.

Despite the success of some of the aforementioned works to produce and explain power-law distributed observables, there are two fundamental differences between neural SOC models and sandpile models that cast doubt on the truly generic scale invariance of these models. Firstly, the BTW SOC model obeys conservation law, i.e. sands will not be eliminated and energy level is conserved, however, the neural network is dissipative due to leaky currents. Secondly, in the SOC model of sandpiles, separation of time scales is critical for the power-law behavior, but the neuronal system is constantly stimulus-driven without separation between internal mechanism and external noise, i.e. there can be additional driving while the system producing an avalanche. In general, for nearly every well-known nonconservative SOC model, there exist counterarguments on the nature and truth of their scale invariance [38, 40]. The Olami Feder Christensen(OFC) model [62] and

the Drossel-Schwable forest fire [63] are among the most studied nonconservative models that are claimed to show SOC dynamics mainly based on computer simulations. However, it has been shown that in non-conserving regions they do not show generic scale invariance but instead they wander around the absorbing phase transition point [64, 65].

In general, in systems with dissipation, a loading mechanism is required to bring the system close to the critical point and compensate for the loss of energy. Another approach to model neural networks close to the critical point is by constructing field equations for population activity rates. In the next subsection, we follow this path to build a mesoscopic model of neural activity which captures the coarse-grained dynamic of average activity fields and takes into account the relevant internal noise originating from finite-size effects. We will show how neural population models can be mapped to the directed percolation model of critical dynamics at the bifurcation points of mean-field equations. Afterward, we discuss tuning or loading mechanisms that bring the system close to this phase transition point.

1.3.2. *Criticality in the Mesoscopic Models of Cortical Activity.* Up until now, we have discussed neural models based on automata dynamics resembling sandpile models. Another approach to critical dynamics in the neural network is by constructing and analyzing the mesoscopic model of the neural activity which accounts for internal fluctuations in coarse-grained field equations. In general, it is not straightforward to bridge from microscopic dynamics to a mesoscopic phenomenological description. However, it is possible in systems which show criticality and scale invariance to arrive at a phenomenological mesoscopic model close to the critical point. Due to time scale separation and scale invariance, we can track the temporal evolution of the system by the evolution of a few slow mesoscopic degrees of freedom and model the effect of fast microscopic variables as noise. However, in systems out of equilibrium, in the absence of detailed balance, internal noise of the system cannot be deduced from a fluctuation-dissipation equation. Therefore, one cannot simply add a noise term to macroscopic mean-field equations because noise correlations cannot be determined.

However, studying macroscopic mean-field equations is still beneficial. Critical points are the bifurcation points of the mean-field equations and close to these points system dynamics can not be well described by mean-field equation because of amplification of internal noise and finite-size effect which were neglected in building mean-field model. Internal fluctuations in the system caused by stochasticity of each element and finite-size effects have to be included in the noise term which can be determined applying either a heuristic approach or systematic integration using a path integral representation of the stochastic process close to the critical point.

In the following, we first introduce rate models for a single excitatory-inhibitory population which describes the evolution of population's average

activity based on external drive to the cells, and then present continuum neural field equation as an interconnected network of EI units.

Modeling population activity by the dynamics of the average activity of neurons defined as rate $r(t) = \lim_{N \rightarrow \infty} \frac{n_{activ}}{N \delta t}$ is called rate models. Consider an interconnected network consisted of multiple homogeneous sub-networks with all to all connections between neurons of population i and population j with synaptic strength denoted by W_{ij} . Further, assume that identical neurons fire asynchronously in each sub-network. There are two ways of writing rate dynamics depending on the magnitude of membrane potential and synaptic current decay time constants.

The first method is by modeling synaptic input to population i , $I_i(t)$, and its dynamic based on nonlinear gain function F which gives instantaneous population rate in terms of the synaptic current it receives, i.e. $r_j = F_j(I_j)$. Here, the main assumption is that the synaptic current rise and decay time constants are much smaller than the membrane potential decay time constant, and therefore, output firing rate can be written as an instantaneous function of the input current. In this case, the evolution of the current to population i can be written as:

$$\frac{dI_i}{dt} = -\frac{I_i(t)}{\tau_I} + \sum_j w_{ij} F_j(I_j(t))$$

If the input to the cell only depends on presynaptic parameters then we can write down the activity model as follows:

$$\frac{dr_i}{dt} = -\frac{r_i(t)}{\tau_i} + F_i\left(\sum_j w_{ij}(r_j(t))\right) \quad (1.5)$$

In case of either fully connected or sparsely connected network, one can explicitly determine the gain function F . Suppose τ_m is the membrane potential decay time constant, τ_r and τ_d are the synaptic current rise and decay time constants, then if $\tau_m \gg \tau_d, \tau_r$, the first model with $\tau_I = \tau_m$ and if $\tau_d \gg \tau_r, \tau_m$, the second model with $\tau_i = \tau_d$ are appropriate rate models. In most cases, the activity-based model (equation (1.5)) is more suitable.

Rate models can accurately describe neural networks in all-to-all or sparsely connected networks. The appropriateness of mean-field solutions for the all-to-all network in the limit of large size should be clear by the above-mentioned assumptions. In a sparsely connected network, correlations among the input to two different neurons, beyond the average population rate, are assumed to be negligible, and correspondingly also the magnitude of cross-correlation between spike trains of neurons is small. Therefore, in the population of neurons in low firing regimes and in the sparsely connected network in which neurons fire with Poisson statistics but asynchronously, the total population rate dynamics can be modeled by

a mean-field equation. The asynchronous state of population rate in the EI population can itself be oscillatory. In Brunel and Hakim [66, 67], a sparsely connected network with synaptic delay between inhibitory feedback and the excitatory rate has been studied using a Fokker Planck formalism for the evolution of the membrane voltage in the asynchronous state. By finding the membrane potential stationary probability distribution and probing its linear stability, they identified saddle-node bifurcation lines and bistable regions and Hopf bifurcation lines separating oscillatory and non-oscillatory asynchronous states. *SI* (Synchronous Irregular) with oscillation in population-level but irregular firing and *AI* (Asynchronous Irregular) states in the region of strong inhibition are of most relevance as the operating region of phase space for the cortical activity. In general, oscillatory instability occurs by increasing average external input. On the other hand, an increase in the variance of the input moves the system towards a stationary firing state. Oscillations of order $\omega_c \propto \sqrt{\frac{\tau}{\delta}}$ appear at the Hopf bifurcation line where δ is the synaptic delay between inhibitory and excitatory population rates and τ is the membrane potential time constant. On the other hand, sub-threshold oscillation of the membrane voltage can lead to a resonance amplification of the input at a sub-threshold frequency. For a low amplitude signal this would be more evident when the average mean input is close to the threshold. Brunel and Hakim [68] also studied fast global oscillations in neural networks operating at a low rate.

The above-mentioned rate equations, also called Neural Mass Models, can be extended to the continuum limit. The cortical organization of the brain suggests that there are cortical columns of thickness $50\mu\text{m}$ to 10mm which are densely interconnected with sparser connectivity between columns. It has been suggested that these columns can be taken as units of information processing [69]. In this case, the average activity of the population of neurons and not the activity pattern of single neurons are taken as a dynamic parameter in the modeling. Continuum neural field models as nonlinear integrodifferential equations with the integral kernel representing the connectivity strength between different neural populations have been introduced by Wilson and Cowan [70, 71].

Neural field models can show wave propagation in terms of a front solution in a bistable network (see Amari (1977) [72, 77]), propagating pulses in an excitable medium (see [73]), and spatially localized oscillations and spiral waves in the oscillatory regime of a local EI population([74]). They can also have localized bump solution [75] and spatially periodic patterns called Turing patterns [76]. Weakly nonlinear analysis, singular perturbation methods, symmetric bifurcation theory, homogenization theory, and stochastic process are the analytic tools for investigating these patterns of activity. (See Bressloff (2011) [78], for a comprehensive review.)

Mean-field solutions can only exist in the limit of $N \rightarrow \infty$ and are based on neglecting correlations among neurons and finite-size effects. Stochastic neural networks have been proposed to account for fluctuations in the asynchronous state of firing and studying their correlations and finite-size effects in different studies [79, 82–84]. These networks model microscopic neural dynamics as a Markov process based on the assumption that neural dynamics is Markovian. Truncation at the first moment of the mentioned Markov process is compatible with the mean-field equation. By truncation of the higher moments based on the assumption that pairwise correlations are of order $1/N$ and p -moments are of order $1/N^{p-1}$, we can derive closed-form equations for higher moments of activity of neurons or subpopulations of neurons. The main assumption is that in the asynchronous state auto-correlations are of order $1/N$. Bressloff [87] utilized system size expansion of master equation to systematically truncate moment hierarchy based on the system size.

Moreover, the stochastic version of the continuum neural field has been discussed in Buice et al. [85] and Bressloff [87]. In general, the mesoscopic description of dissipative systems in which the flow of energy and fluctuations of energy is not based on the equilibrium fluctuations, such as general reaction-diffusion systems, is very complicated. The absence of detailed balance in microscopic dynamics and the fluctuation-dissipation theorem would make a straightforward phenomenological mesoscopic approach like the Langevin dynamics for systems close to equilibrium impossible. However, for the non-equilibrium system which has a steady-state close to a critical point and shows generic scale invariance, effective dynamical description in terms of mesoscopic field equation is in general possible. In the critical state, the perturbation in the system spread in all length and time scales of the system with power-law distributions of size and duration.

In this case, we can write down the dynamics of the system out of equilibrium in terms of the microscopic master equation, like for interacting particle systems. Using the well-known coherent path integral procedure first introduced in the context of reaction-diffusion equation by Doi and Peliti [44, 45] to form non-hermitian bosonic Hamiltonian and continuum field representation, internal fluctuations are automatically taken into account. By using the perturbation approach and renormalization group method, we can study the scale invariance and critical behavior of the model. Subsequently, the field theory representation in terms of path integral over stochastic paths can be translated to the Langevin equation with appropriate noise term using Janssen-Dedomonic functional representation.

Buice and Cowan [85] used coherent path formalism named as Doi-Peliti functional representation [44, 45] to translate the microscopic master equation to a path integral representation for activity fields. One advantage of their method is that the study of scale invariance at criticality in the functional representation is possible. They proposed that the stochastic neural field equation for the excitatory system at a critical point can be written

in the form of Langevin’s description of directed percolation. Cowan et al. [88] used the method of path integral representation in the stochastic model of spiking neurons supplemented by anti-Hebbian synaptic plasticity as the self-organizing mechanism. Their network possesses bistability close to the saddle-node bifurcation point which is the origin of the avalanche behavior in the system.

In the next section, we introduce the balance of inhibition and excitation as the control parameter that tunes the system near the critical point.

1.4. Balance of Inhibition and Excitation. The role of feedback inhibitory currents and tuning the strength of this feedback in the EI population is of significant importance for studying spontaneous activity. Inhibition is generated by a specific type of neurons called inter-neurons which comprise only about 20% of the total number of neurons and are generally forming short-ranged connections in comparison with excitatory synapses. Local inhibitory feedback shapes the activity of the excitatory population by restricting the spatial propagation and prohibiting the persistence of a high level of activity in the local population of neurons.

There must be a balance of excitation and inhibition which prohibits the network from high firing synchronized active state while poising the system close to the edge of the activity. At this dynamical regime, neurons show rapid response to the change in the input.

Inhibitory-Excitatory balance can lead to the oscillatory or the avalanche-type activity in local populations and the emergence of waves and fronts in larger scales of cortical activity. At the level of individual neurons, this balance leads to a highly irregular firing of neurons with a coefficient of variation (CV) of the inter-spike intervals being close to one resembling Poisson point process [89]. Studies using the voltage clamp method that track conductance of excitatory and inhibitory synapses on neurons both in vivo and in vitro, confirmed that there exist proportionality and balance of inhibitory and excitatory currents during Up-state [91], sensory input [90] and spontaneous activity [93].

Van Vreusjik and Simpolinski [80, 81] introduced a sparsely balanced network with strong synapses in which in a balanced state (time and population-) average excitatory and inhibitory inputs cancel each other and the neurons’ firings are fluctuation driven with excitatory and inhibitory rates linearly related to the external input strength. In their model, each neuron is connected to k other presynaptic neurons and synaptic connections are of order $O(1/\sqrt{k})$ which means that the mean inhibitory and excitatory currents are of order $O(\sqrt{k})$. Synaptic strengths are selected, so that only \sqrt{k} number of excitatory spikes are needed to cross the threshold. In order to have solutions for the mean population activity, i.e. $R_E = F(I_E)$ and $R_I = F(I_I)$, apart from zero(inactive) and one(saturated), the total input to excitatory population $I_E = E_{Ext} + m_E - J_E m_I = O(1/\sqrt{k})$ and accordingly inhibitory neurons should vanish to leading order in k . In the

large k limit, both m_E and m_I depend linearly on the external input to the cell. They argue that for the network to reach a balanced state, saturated and quiescent states have to be unstable, which is satisfied by certain conditions on weights. Previously mentioned works of Brunel and Hakim on sparsely connected networks also pinpoint a balanced regime for excitatory and inhibitory current strengths [66, 67]. Because the network is settled in a balanced state, a small deviation from the balanced input leads to a local change in firing rate. Therefore, the system is highly sensitive to input while maintaining a low firing rate and highly variable spike trains at the individual neuron level.

Organizing principles that cause the balanced state and conditions on weights and external input that give rise to it are of particular importance. The main hypothesis is that activity-dependent synaptic plasticity rules, which change the connection strengths of both inhibitory and excitatory synapses according to the activation of their presynaptic or/and postsynaptic neurons, are the regulating mechanisms for reaching the balanced state. Using only inhibitory plasticity, Vogels et al. [94] investigated how Synaptic Time-dependent Plasticity, balances excitation and inhibition in local sub-populations of an EI-interconnected network. This will lead to a receptive field counterpart for the inhibitory subpopulation that is of the same shape as an excitatory one. Detailed balance of excitation and inhibition leads to a sparse and low amplitude output for stimuli, which is in agreement with experimental results. In the network architecture they have used, excitatory stimuli reach the target region through an excitatory pathway and an indirect inhibitory pathway, therefore, the inhibitory signal in each sub-population is a delayed shadow of excitation. In contrast, in this work, we consider the case of local inhibitory connections, and therefore the inhibitory feedback is originated from the target population activity and not the stimuli. Deco et al. [18] investigated that strong local feedback can compensate longer-range excitatory excess in input and lead to a stable asynchronous state at the EI sub-population. Furthermore, combining both balanced states and up and down transitions Kumar et al. [95] investigated the clustering effect in a balanced network which introduces a bi-stability in local clusters with a discrete transition between low and high firing rates. Here, dynamic fluctuation causes transitions between these states.

Neurons can still be in a fluctuation-driven state at which total average currents set the average stationary membrane potential to a value less than the threshold, but fire with a high rate. To speculate on the regime of parameters that would match characteristics of spontaneous activity, we hypothesize that the spontaneous activity results from being close to the bifurcation point of the mean-field equation from the quiescent state to a balanced low activity state. In this state, neuron firing has high variability and the balance of inhibition and excitation causes the network to show avalanche dynamics. Near the phase transition of the macroscopic model, due to the time scale separation of slow dynamic on the center manifold and

fast modes of activity, the nonlinear Langevin equation with noise term that is activity-dependent can be a plausible mesoscopic model for the neural network. Critical slowing down near the bifurcation point of the mean-field equation results in the separation of time scale between critical degrees of freedom and fast parameters, the emergence of the order parameter, and critical fluctuations. The hypothesis is that the neural system is poised at the critical point separating active and inactive states with noise intensity that is proportional to the activity rate. Once choosing the noise term heuristically and constructing the Langevin type mesoscopic equation, we can use field theoretical representations of Langevin equation using Janssen-Dedomonic response functional make it possible to investigate scaling properties of the model in the critical regime. Perturbation theory and renormalization group methods can be used to study critical dynamics.

As we stated before, for the system to show absorbing phase transitions, we need to fine-tune the coefficient of the linear term, i.e. $r := \lambda - \sigma = 0$ in equation (1.3). We have suggested that synaptic plasticity for both inhibitory and excitatory synapses and also short-term synaptic plasticity which operates on much longer time scales than rate dynamics, can bring the system close to this bifurcation point. However, the region of the parameter space corresponding to the critical behavior can be enlarged if we consider the inhomogeneity and modular structure of the neural network. As we know, the anatomical structure of the brain influences critical dynamics and vice versa. As structure and dynamics have reciprocal relations, self-organization of the structure into the hierarchical modular structure can be an important ingredient for the critical dynamic that we observe. In modular self-similar networks, specialized neural clusters contain smaller and more specialized neural clusters at many spatial scales. In systems with generic scale invariance, criticality appears over a region of the parameter space with nonzero measure.

Moretti and Munoz [96] showed that hierarchical modular structure in neural networks extends the region of criticality. Below the critical point and in the sub-critical region of the mean-field equation there is a region of the parameter space that shows scale-invariance and power laws called the Griffith phase. Heterogeneity brings about regions that are more connected and accordingly more active. In the Griffith phase, while the whole network is in a quiescent state, activity in regions with more connectivity decay with a longer time constant. Wang et al. [97] showed that modularity in the SOC model of Levina et al.(Eq.(1.4)) can widen the range of coupling strength that leads to criticality. Similarly, Massobrio et al. [98] showed that the scale-free network architecture (i.e. power-law distribution of degree) and larger standard deviation of weights will widen the region for the critical state. Robinov et al. [99] investigated in a simulation analysis the interplay of modular connectivity, synaptic plasticity, and the emergence of power laws. As in previous studies, they have asserted that hierarchical modularity

enables a broader critical regime while STDP tunes the system to reach the critical regime.

Being at a critical regime, besides explaining the scale-free characteristic activity of the neural network, may be seen as serving functional and computational purposes. In the next section, we review some of the most important works in this direction.

1.5. Functional Benefits of Being in the Critical State. Criticality has been claimed to be an optimal state for computation and information processing. Shew et al [101] showed that the cultured cortex slice which operates in the avalanche regime possesses maximum dynamic range. Moreover, an imbalance of excitation and inhibition would cause the network to respond weaker to the input. They used the following indicator for the dynamical range :

$$\Delta = \log\left(\frac{S_{0.9}}{S_{0.1}}\right)$$

where $S_{0.9}$ is the input amplitude that leads to the output firing rate of value $0.9R_{max}$. In another work, Shew et al. [102], show that information capacity measured as the entropy of binary LFP patterns (defined by assigning 1 to active sites and 0 to inactive ones) of spontaneous and stimulus-evoked states, and information transmission capability defined as mutual information of input and output are maximized when the EI system resides in the balanced regime with avalanche dynamics. Yang et al. [103] reported maximized variability of synchrony at the onset of synchronization. They used Hilbert transform to obtain the phase trace for LFP signals and defined Kuramoto order parameter as a synchrony measure during bursts. The entropy of this random variable is maximized at the regime of the balance of inhibition and excitation. This indicates a moderate level of synchrony with high variability at the critical point.

Poil et al. [104] used DFA analysis to study long-range temporal correlations and show that in the regime of the balance of excitation and inhibition, oscillations have scale-free amplitude modulation. Lombardi et al. [105] showed that the power spectral density $s(f) = F(C(\tau))$ scale as $S(f) \propto f^{-\beta}G(f/L^{-\gamma})$ with $\beta = 1.1$ and $\gamma = 0.2$. In Timme et al. [106], authors utilized the Tononi measure of complexity considering sub-sampling effects in both a simplified cortical branching model and culture data and find out that complexity is maximized in the critical systems. Yang et al. [5] showed that maximal information capacity is achieved in the region of the dynamical space that shows the excitation and inhibition balance, oscillation, and avalanche patterns. Dynamical balance of excitation and inhibition leads to irregular firing, which results in high accuracy and speed of information relay in terms of firing rate. On the other hand, synchrony reduces redundant spikes. Although strong or weak synchrony is pathological, a moderate level of synchrony is crucial for information transfer. Moreover, neural avalanches are shown to be the state which optimizes

the response range of stimulus intensities, the amount of information that can be transferred, and the variability of spontaneous synchrony. Therefore, in an avalanche oscillatory regime, a low firing rate and maximal energy efficiency can be achieved simultaneously. The neural firing rate corresponding to maximal energy efficiency is constrained in the range of $1 - 10Hz$.

1.6. Arguments Against the Critical State of the Brain. It should be noted that despite mentioned experimental results there exist reports which claim that power-law distributions might not be the best fit for neural data. In a paper by Priesemann et al. [107] by parallel spike recording and LFP signal analysis in vivo found out that the avalanche distribution matches a log-normal distribution better than power-laws. Even by considering the effects of sub-sampling, simplified critical models fail to match the empirical data. They found that simplified SOC models would fit the data if they are in a slight sub-critical regime and are subject to a sufficient external drive, which allows a melange of avalanches and destroys the separation of time scales. Priesemann et al. [108] investigated the case in which a neural model driven by an inhomogeneous Poisson process can show pseudo power laws without being at criticality. In this case, inhomogeneous Poisson process produces avalanches with statistics of the sum of exponential which leads to a power-law size distribution with exponential cut-off.

Martinello et al. [109] proposed a model for casual avalanches based on a simple contact process for avalanches. In this model, each active site is assigned to an avalanche A_k . The dynamics of a just created avalanche in their setting follows $\dot{\rho}_k = \sqrt{\rho_k} \xi_k(t)$, which is the Langevin equation for mean-field description of a branching process.

In another work, Villegas et al. [110] argued that power laws can be an artifact of time series thresholding. Touboul et al. [111] claimed that spiking neural networks in the asynchronous irregular state can show scaling and power-laws of avalanche size and time distribution without being critical. Destexhe and Touboul [112] in a recent work summed up arguments against some methods of collecting and interpreting the experimental results. These arguments should be taken into account in the study of critical dynamics both in experiments and modeling. In general, scaling relations between exponents are stronger indications of critical state than power laws.

1.7. Organization of the Current Work. The majority of self-organizing critical neural models are based on an excitatory population of neurons with slow drive accompanied by adaptive weight or degree of connectivity which tunes the non-conservative system close to the critical point. In this work, we investigate a network of both excitatory and inhibitory neurons and also abandon the time scale separation between internal dynamics and external drive. We start by studying mean-field equations for the dynamic of average excitatory and inhibitory rates. Supplementing the EI population dynamics with long-term and short-term plasticity rules, we observe that the system

is self-tuned to the region corresponding to the balance of average excitation and inhibition arriving at each neuron. This state is very close to the Bogdanov-Takens bifurcation point of the mean-field equations for EI population rates. We observe that the activity pattern in this region of the parameter space is in the form of irregular bursts of activity (i.e. avalanches). Close to the BT bifurcation point, the avalanche size and time distributions are of the power-law form with exponents matching those from the branching process. Therefore, in summary, the self-organizing parameter in our system is the balance of excitation and inhibition, and the self-organizing principle is the long-term and short-term synaptic plasticity. Furthermore, reduced dynamics for an excitatory population close to the BT bifurcation point and the balanced regime are of the form of the Langevin equation for directed percolation.

In chapter 2, we will introduce the conductance-based model neuron and its response to the impulse and Poisson input. Using the Fokker-Planck equation for the dynamics of membrane potential and the first passage time distribution, we approximate the neuron's gain function in the limit of low firing rate and at the point where the stationary average membrane potential is near the firing threshold. We have investigated the condition for the output spike train to be of Poisson point process type in response to Poisson input. Linear Poisson approximation is introduced as a linearization of the gain function at values of (E, I) input rates that puts the stationary average membrane potential at an optimal value V_{OPT} . At this level of average membrane potential close to the middle of the membrane potential range, $[V_{rest}, V_{th}]$, which is reached by the balance of average excitatory and inhibitory currents, the firing of the neurons by the fluctuations in the input shows the highest variability.

In chapter 3, we consider a population of excitatory and inhibitory neurons both sparsely and all-to-all homogeneously connected, i.e. network of identical neurons with the input to all neurons having the same statistics. Considering homogeneity in the spatial domain and neglecting temporal fluctuations, one can write down mean-field dynamics for the average excitatory and inhibitory rates. Analyzing bifurcations of the coupled equation for population rates by selecting the external drive to excitatory population and strength of average excitatory connections as control parameters, we focus on the region in parameter space that allows a low firing rate of single neurons. Therefore, in this regime in which average input currents are canceling each other, neurons' firing is due to fluctuations in the input, and therefore, interval times between spikes show high variability. It is important to note that the external drive alone does not lead to the firing of the neurons. Instead it is the internal synaptic connections among neurons which are tuned to deliver a balance of excitation and inhibition input that cause the firing. Low firing rate state and quiescent state can coexist and form a bi-stable system that shows stochastic jumps between these states due to internal or external fluctuations. On the other hand, the quiescent state in

the absence of bi-stability may also lose stability through Hopf bifurcation and low amplitude and slow oscillations emerge in the system. Saddle node bifurcation producing the low firing fixed point and Hopf bifurcation line destabilizing quiescent state meet each other at the BT bifurcation point. We will discuss both by simulation and analytic discussion that close to this point, avalanches with power-law size distribution besides oscillations emerge in the system. We will discuss that the BT point coincides with the condition on the balanced input to excitatory and inhibitory cells and condition on Poisson firing statistics.

For the neural network to operate in a balanced regime, there must be a mechanism that adaptively tunes connection strengths. In chapter 4, we propose a mean-field synaptic dynamics based on Long-term Synaptic Time Dependent Plasticity(STDP) for both inhibitory and excitatory synapses that delivers the network close to the BT bifurcation point of the mean-field equation. Plasticity occurs in a very slow time scale compared to the synaptic dynamic and this enables us to apply averaging on the input and output spike trains. Furthermore, we discuss how short-term synaptic(STP) depression of excitatory synapses can broaden the region of the phase space, here the external excitatory input and the average connection strength between excitatory neurons, in which avalanche dynamics occur. Therefore, even at higher input rates, STP acts as a homeostasis mechanism that self-tunes the network in a shorter time scale compared to long-term plasticity. On the other hand, STP can cause bi-stable alternation between the quiescent and active state as a mechanism to produce Up-Down states transition.

In chapter 5, we introduce the Wilson-Cowan model and study conditions on Turing instabilities and Local Hopf bifurcation.

To study the finite-size effect as the internal noise which can make the system show behavior different than mean-field solutions especially near bifurcation points, we either have to heuristically specify noise characteristics near a mean-field solution, or start from a description of the system at a microscopic level which is compatible with the mean-field equation upon coarse-graining. In the former case, the fact that in a sparsely connected network, neurons' spike trains are weakly correlated and the spiking process is Poisson, leads us to assume that the fluctuations are local and the magnitude of them is proportional to the activity rate. Therefore, heuristically, we can model the internal noise by a white noise with a variance of $\frac{R(x, t)}{\sqrt{N}}$ and add this fluctuating term to the mean-field equation for the average population rate of activity. In Chapter 6, we introduce a microscopic model based on Poisson neurons and derive fluctuations in the stationary state which depend linearly on the activity rates. Afterward, we present a mesoscopic model for the neural activity near phase transition that includes a noise term and a loading mechanism that regulate it near to BT bifurcation point. The hypothesis is that the neural system wanders around this phase transition point.

2. Single Neuron Model

We start by introducing and analyzing the single neuron model as the basic computational element in the neural network and its response to various patterns of input. Neurons are the elementary information processing units in the nervous system. They are enormous in quantity with a density of 10^4 per $1mm^3$ and connected to each other in a complex way. They are located in a sea of ions and when at rest(not active), they maintain a potential difference between internal and external ion concentrations through numerous ion gates on their membranes. Membrane voltage, the difference of electric potential between inside and outside of the cell, has the rest value around $V_{rest} = -65mv$. Ion channels maintain concentration gradients with a higher concentration of Na^+ and Ca^{2+} outside the cell and a higher concentration of K^+ inside the cell. In most neurons, three main components can be distinguished: dendrite, soma, and axon. Input from other neurons in form of ion currents is collected by dendrite and transmitted to soma, if the total input is larger than a threshold then the neuron goes through a process called spiking and sends a signal to other neurons via the axon. Spikes are immediate depolarization that is generated by depolarizing synaptic input which gradually activates sodium channels and causes an inflow burst of sodium ions leading to a spike, at this high potential level, K^+ ion channels will open, and with an outflow of K^+ neuron's membrane potential decrease toward rest values.

Integrating input and producing the spike is conducted in a complicated nonlinear way. The process of generation of a spike can be well described by the Hodgkin-Huxley model which is a set of coupled equations for voltage-dependent k^+ and Na^+ channels and leak current which models other ion channels activity. This model based on the ion current flow is very complicated to work with in the case we want to investigate the network of spiking neurons. Therefore, many simplifications have been presented to model spiking behavior. Here, we discuss one of them, namely integrate and fire model neuron in which the change in the membrane voltage of the neuron receiving time dependent synaptic current $i(t)$ follows :

$$C \frac{dv(t)}{dt} = g_{Leak}(v_{Leak} - v(t)) + i(t), \quad (2.1)$$

for $v(t) < v_{th}$. When the membrane voltage reaches $v_{th} = -50mv$ neuron spikes and immediately its membrane voltage resets to v_{rest} which is equal to $v_{Leak} = -65mv$.

There are two main types of neurons called excitatory and inhibitory. Thus, currents to each cell may have inhibition or excitation effects depending on the type of the presynaptic neuron. The incoming signal from other neurons is in the form of diffusive ions called neurotransmitters. These molecules would bind to receptors on the postsynaptic neuron which through

some intermediate molecular mechanism causes voltage-dependent ion channels on the membrane to open up by changing the conductance of them. Inhibitory currents would ultimately cause to open up k^+ or cl^- channels and therefore have hyper-polarization effect (when the membrane potential of the neuron is above $-80mv$), vice versa excitatory input current leads to depolarization through opening up of Na^+ and Ca^{+2} channels. Time course of opening and closing these channels can be modeled as the evolution of the conductances and is dependent on the type of synapses with their specific type of neurotransmitters and receptors. Mainly there exist two types of Inhibitory synaptic currents, fast GABA-A synapse with very short rise time and relatively small decay time of $5ms$ and slow GABA-B synapses working through secondary messenger ions, with a rise time of about $30ms$ and much longer decay times around $100 - 300ms$. Similarly, based on receptors existing in an excitatory synapse two types of excitatory synaptic currents exists, fast AMPA current with negligible rise time and decay constant of around $3 - 5ms$ and slower NMDA receptor acting mainly through the inflow of Ca^{+2} which have a much longer rise ($\sim 10ms$) and decay ($40 - 100ms$) time constants [113]. Slow excitatory synapses are believed to have effects on long-term potentiation and depression of synapses through Ca^{+2} influx and probably are less important in models of spiking activity.

In the following, we would concentrate on a model with just one type of inhibitory and one type of excitatory synapses, which can be seen as the average effect of the two types of synapses. We can write the synaptic inhibitory and excitatory current as :

$$i(t) = g_{inh}(t) * (V_{Rinh} - v(t)) + g_{exc}(t) * (V_{Rexc} - v(t)) \quad (2.2)$$

V_{Rinh} and V_{Rexc} are reverse potentials of excitatory and inhibitory ion channels and based on experimental studies we choose values of $-80mv$ and $0mv$ for them, respectively [113]. $g_{inh}(t)$ and $g_{exc}(t)$ are the conductances of inhibitory and excitatory ion channels respectively. These conductances are changing by the inhibitory and excitatory input to the cell. Each spike of a presynaptic inhibitory or excitatory neuron j to a postsynaptic neuron k that is received by the neuron k at time t_0 , will change the inhibitory or excitatory ion channels' conductance of postsynaptic neuron for $t > t_0$ according to :

$$g_{Inh}^k(t) = w_{kj} * g_0^{inh} * \exp\left(-\frac{t - t_0}{\tau_{syn}^{inh}}\right) \quad (2.3)$$

$$g_{Exc}^k(t) = w_{kj} * g_0^{exc} * \exp\left(-\frac{t - t_0}{\tau_{syn}^{exc}}\right)$$

Here, we assumed that the rise time of synaptic conductances are very small compared to other time scales in the model and therefore, we have

modeled the synaptic current by a decay term with the synaptic decay time constant, τ_{syn} , which we assume to be the same value of $5ms$ for both inhibitory and excitatory synapses.

The fact that effect of presynaptic spikes on the membrane voltage of the postsynaptic neuron is dependent on the membrane voltage of the postsynaptic neuron makes neuron behavior different than integrate and fire model with passive membrane, in which:

$$i(t) = w_{kj} * q_0 * exp(-\frac{t - t_0}{\tau_{syn}})$$

As can be seen from equation (2.2), when the membrane potential is close to V_{rest} , the effect of excitatory input will be stronger than when the neuron membrane potential is close to V_{th} . Vice versa, close to V_{th} effect of an inhibitory input would be more profound. As V_{Reexc} is much greater than the interval $[V_{Rinh}, V_{th}]$, the excitatory ion channels' conductance will depend minimally on the membrane potential. With the mentioned values for reverse potentials, an excitatory spike will cause a $\frac{V_{Reexc} - V_{rest}}{V_{Reexc} - V_{th}} = 30\%$ higher change in the postsynaptic potential when V is close to the reset value compared to being at the threshold. On the other hand, the inhibitory input leads to a two times greater membrane potential change when it arrives at a neuron whose membrane potential is near V_{th} :

$$\frac{V_{Rinh} - V_{th}}{V_{Rinh} - V_{rest}} = 200\%$$

In the case of feedforward inhibition to the cell which arrives after excitatory input with a transition delay, the mentioned fact makes inhibition more effective and can compensate for the delay to an extent and sharpen the time window for the excitation. This would eliminate late excitations and facilitate synchronization of the neurons in the excitatory pool. A longer decay time for inhibition such as GABA-B receptor type would also eliminate further excitations. In the next section, we consider the response of the neuron to impulse input and investigate the role of the strong dependence of inhibitory current on the membrane potential and the delay between excitatory and inhibitory inputs.

2.1. Impulse Response of the Neuron. In this section, we consider the response of the neuron to synchronous excitatory and inhibitory input. We know that usually synchronous arrival of 20 – 30 presynaptic excitatory spikes are needed for activation of the target neuron. On the other hand, as we described before, network activity of avalanche type resembles relatively synchronous excitatory which is followed by an inhibitory synchronous input. This motivates us to consider the firing condition of the target neuron receiving impulse input.

First, we present the necessary condition that an inhibitory and an excitatory impulse input at time t_0 namely, I_{inh}^0 and I_{exc}^0 lead to an action potential. Suppose at time t_0 the postsynaptic neuron membrane potential is V_0 and it receives simultaneous spikes from inhibitory and excitatory afferents of total magnitude w_I and w_E , respectively. The neuron would spike if the maximum of the potential curve $v(t)$ would reach a higher value than V_{th} . Suppose this maximum occurs at time t_m , then from equating the right side of equation(2.1) to zero using equations (2.2) and (2.3) we have:

$$v(t_m) = \frac{g_{leak}v_{leak} + e^{-\frac{t_m}{\tau}} (g_0^{inh}w_IV_{Rinh} + g_0^{exc}w_EV_{Rexc})}{g_{leak} + e^{-\frac{t_m}{\tau}} (g_0^{inh}w_I + g_0^{exc}w_E)} \quad (2.4)$$

This is a monotonically decreasing function of t_m . Therefore, the necessary condition of firing is that $v(t_m = 0) > v(th)$. This leads to the following constraint for the amplitude of excitation impulse in terms of the inhibitory one:

$$w_E > \frac{g_{leak}}{g_0^{exc}} \left(\frac{V_{leak} - V_{th}}{V_{th} - V_{Rexc}} \right) + w_I \frac{g_0^{inh}}{g_0^{exc}} \left(\frac{V_{Rinh} - V_{th}}{V_{th} - V_{Rexc}} \right) \quad (2.5)$$

For this boundary-value of excitatory input, the time of firing t_m would be obtained by setting the right hand side of Eq(2.4) to V_{th} and solving for $t_{fire} = t_m$. Higher the value of w_I , the minimum value of w_E that causes firing would lead to a smaller first firing time. Fig.6 shows minimum excitation impulse needed for firing with $V_0 = V_{rest}$. Minimum excitation increases semi linearly while the corresponding firing time decreases when we change the inhibition strength. The latter effect can not be seen in the non-conductance current-based LIF model.

A simple argument can show why the firing time decreases by increasing both inhibitory and excitatory impulse strengths. As w_I increases, the minimum value of w_E required for action potential would also increase according to the equation (2.4). It guarantees that at the time of firing, when $V(t_m) = V_{th}$, the drift of potential by excitation and inhibition approximately cancel each other, therefore, at t_m :

$$g_{exc}^{min}(t_m) = g_{inh}(t_m) \frac{V_{Rinh} - V_{rest}}{V_{Rexc} - V_{th}}$$

Considering the same synaptic decay time constants for the inhibition and the excitation input, we have :

$$\frac{g_{exc}^{min}(t_0)}{g_{inh}(t_0)} = \frac{g_{exc}^{min}(t_m)}{g_{inh}(t_m)}$$

which results in the following drift at t_0 :

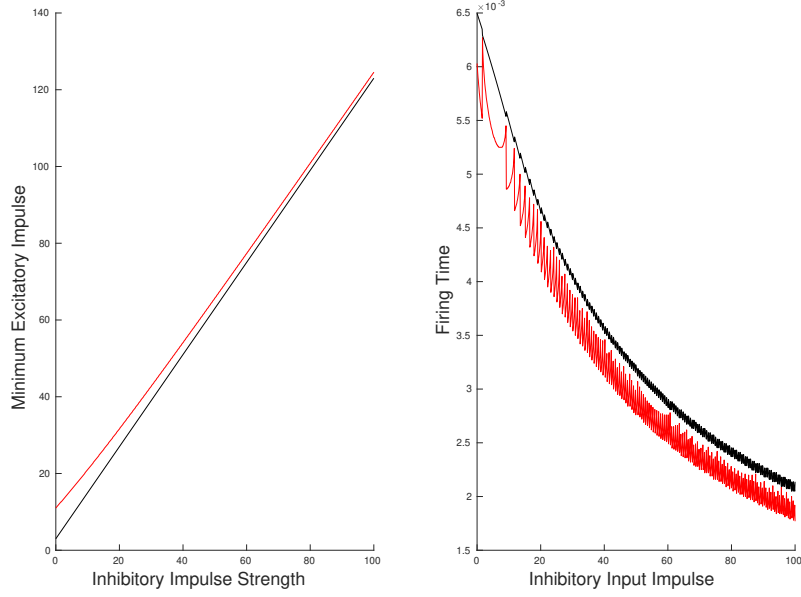


FIGURE 6. (Left) Minimum amplitude of the excitation impulse needed for the firing of the neuron vs. various inhibitory impulse strengths. The red line is the simulation result and the black one is the necessary constraint of Eq.(2.5). (Right) The first time of firing of the neuron receiving the minimum excitation impulse for each inhibitory impulse, for higher magnitude impulses neurons fire faster. The red curve is the simulation result and the black one is the approximation based on Eq.(2.4) and Eq.(2.5).

$$\begin{aligned}
\frac{dv(t)}{dt}(t_0) &= g_{inh}(0)(V_{Rinh} - V_{rest}) + g_{exc}(0)(V_{Rexc} - V_{rest}) \\
&= g_{inh}(0)[(V_{Rinh} - V_{rest}) + \frac{V_{Rinh} - V_{rest}}{V_{Rexc} - V_{th}}(V_{Rexc} - V_{rest})] \\
&= g_{inh}(0)(V_{rest} - V_{Rinh})\left[\frac{V_{Rexc} - V_{rest}}{V_{Rexc} - V_{th}} - 1\right]
\end{aligned}$$

Clearly this drift will increase by increasing w_I which increases $g_{inh}(0)$. This leads to a higher net drift at $t = 0$ and higher average curvature of the potential curve and lower firing time. It is clear that applying higher excitation than the minimum excitation would decrease the firing time.

When a neuron resides closer to the threshold, the minimum excitatory current that activates the neuron would be smaller. Suppose that constant inhibitory and excitatory currents set the stationary membrane potential at the value V_{st} and at time $t = 0$ excitatory impulse of magnitude w_E arrives

at the neuron. We can write down membrane potential dynamics for $t > 0$ as :

$$C \frac{dv(t)}{dt} = -k(v(t) - V_{st}) + g_{exc} w_E * e^{-\frac{t}{\tau}} (V_{Rexc} - V_{st}) \quad (2.6)$$

Here, k is the drift coefficient that drags the neuron to the potential level V_{st} which stems from the overall effect of the background input.

For the value of minimum excitation at the time of firing, we would have $\frac{dv}{dt} = 0$. Taking $\Delta V = V_{th} - V_{st}$ and approximating time of firing as :

$$t_m \approx \frac{\Delta V}{\left\langle \frac{dv}{dt} \right\rangle_{[0, t_f]}} = \frac{2\Delta V}{\frac{dv}{dt}_0}$$

we can solve for for w_E^{min} from equating the write hand side of equation(2.6) to zero at t_m which results in :

$$w_E^{min} = \frac{\Delta V(1 - 0.5k\tau)}{0.5(V_{Rexc} - V_{th})g_{exc}} \quad (2.7)$$

Fig.7 shows that the minimum excitation required for firing in the absence of inhibition increase linearly with the increase of the distance of the neuron stationary state membrane potential to the threshold. The blue line is the approximation of equation (2.7).

So far, we have considered the simultaneous arrival of both excitatory and inhibitory impulses. Relative delay of inhibitory impulse changes the balance condition. Suppose again an inhibitory impulse of magnitude w_I arrives after an excitatory impulse with the time delay t_d . For high values of inhibitory feedback, minimum excitation would be the value that sets the neuron to the firing threshold before the arrival of the inhibitory signal at t_d . Neurons receiving greater excitatory current will fire faster, i.e before t_d , and neurons receiving weaker excitatory current fail to fire.

For lower values of w_I , a sufficient amount of excitation leads to firing time larger than t_d . In this case, the minimum excitatory impulse should be higher than their counterpart in simultaneous cases but is lower than the amount that makes the cell fire before t_d .

Therefore, for weak inhibitory and excitatory currents, delayed inhibition increase the minimum excitation for firing but reduces the time of firing (compare green curves in Fig.8 related to the case with the delay with black ones related to the case with no delay between excitation and inhibition). However medium to high amplitude of delayed inhibition would set minimum excitation to a value that corresponds to firing right before the arrival of inhibitory current. This means that for the value of excitation more than

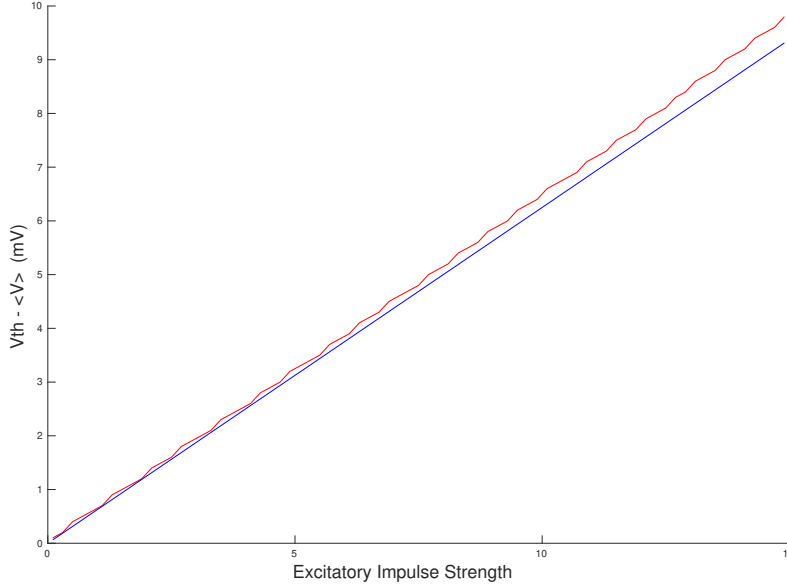


FIGURE 7. Minimum excitation necessary for firing versus the steady level of neuron potential. The red curve is the simulation result and the blue curve is approximation by Eq(2.7).

this value neurons will fire before the arrival of inhibition and for value below that neurons will not fire at all. Therefore, delayed strong inhibition set a time window for firing.

2.2. Response of the Neuron to the Constant Input. Suppose the target neuron receives a constant number of excitatory and inhibitory spikes per unit time, respectively denoted by ρ_E and ρ_I . Further, let us assume all the excitatory spikes to have the same strength, w_E , and all the inhibitory spikes are of magnitude w_I . Conductance of the excitatory channels $g_{exc}(t)$ is modified by excitatory spikes arrived at times $s < t$:

$$g_{exc}(t) = \int_{-\infty}^t g_{exc}^0 w_E \rho_E \exp\left(-\frac{t-s}{\tau_{syn}^{exc}}\right) ds = g_{exc}^0 w_E \rho_E \tau_{syn}^{exc}$$

The same formula applies to the constant inhibitory current. The potential of the target neuron fed by this current will reach a stationary value. If this stationary limit is greater than V_{th} , then the target neuron will fire periodically. This constraint reads as :

$$\rho_I < \frac{g_{leak} * (V_{th} - V_{rest}) + g_{exc}^0 * w_E * \rho_E * \tau * V_{th}}{g_{inh}^0 * w_I * \tau * (V_{inh} - V_{th})} \quad (2.8)$$

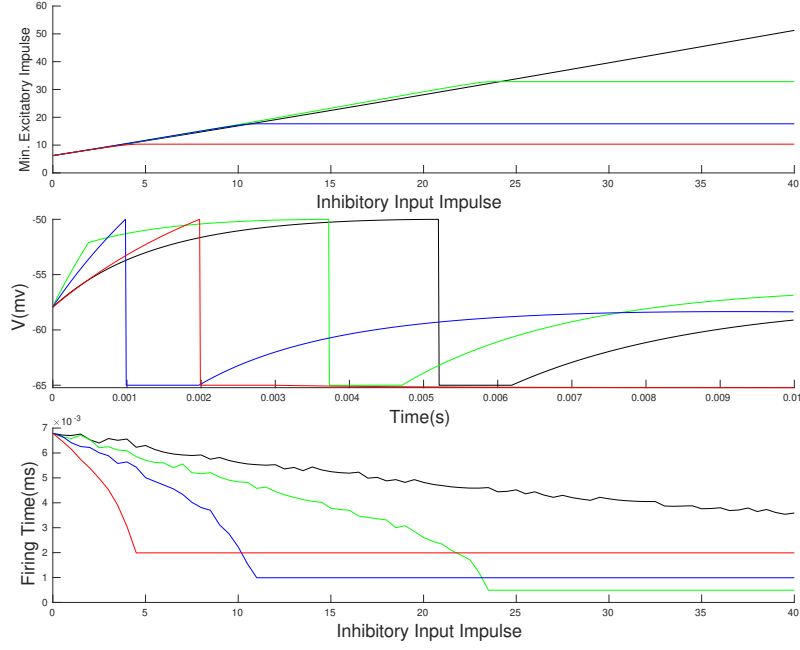


FIGURE 8. Inhibition current to the neuron arrives with four different values of delay after excitation. ($t_d = 0$ black curves, $t_d = 0.5ms$ green curves, $t_d = 1ms$ blue curves, and $t_d = 2ms$ red curves.) (Top) The minimum excitatory current that makes the neuron fire for different strengths of inhibitory input. (Middle) Membrane potential tracks for the value of inhibition impulse $W_I = 20$. (Bottom) Firing time of the neuron in response to the minimum excitatory current associated with each inhibitory input.

The stationary limit of the potential is a weighted average of reverse potentials as follows:

$$V_{st} = \frac{g_{leak}V_{leak} + g_{exc}^0 w_E \rho_{ET} V_{Rexc} + g_{inh}^0 w_I \rho_{IT} V_{Rinh}}{g_{leak} + g_{exc}^0 w_E \rho_{ET} + g_{inh}^0 w_I \rho_{IT}} \quad (2.9)$$

If input rates satisfy equation (2.8), the output firing rate would be :

$$\rho_{out} = (g_{leak} + g_{exc}^0 w_E \rho_{ET} + g_{inh}^0 w_I \rho_{IT}) \left(\ln \frac{V_{rest} - V_{st}}{V_{th} - V_{st}} \right)^{-1} \quad (2.10)$$

Fig.9 shows the output firing rate for three different fixed values of excitatory input rates versus a range of inhibitory input rates.

2.3. Response of the Neuron to the Poisson Input. In this section, we analyze the response of the neuron to a specific type of current, namely Poisson input. The reason to consider this input is that in an asynchronous firing state neurons receive Poisson input from other neurons. To see this,

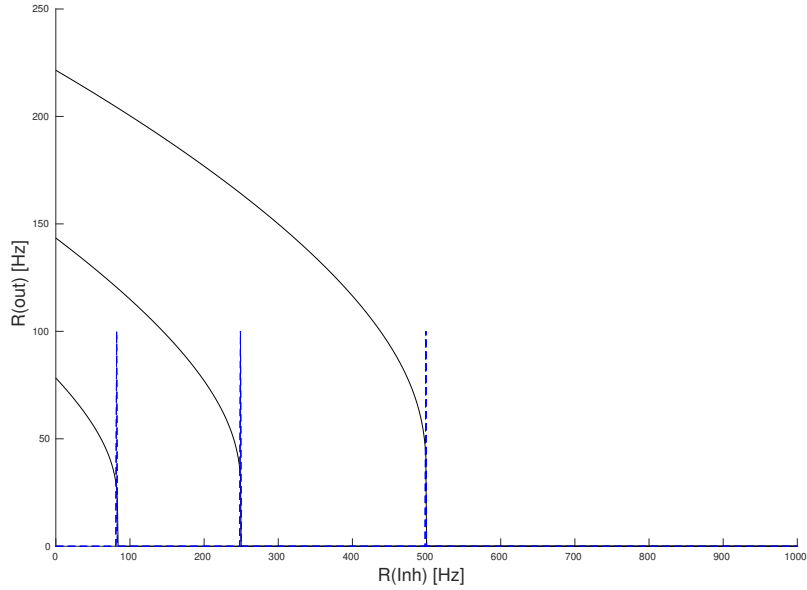


FIGURE 9. Firing rate of a neuron receiving three different values of constant excitation versus different values of constant inhibitory input. Simulation and equation (2.10) match and the cutoff is determined by equation (2.8).

assume number of afferents to each neuron is high and the average population firing rate, r , is approximately constant. Considering homogeneity in the number of connections and weights, then at any time interval Δt , the probability distribution that a neuron has k presynaptic active neurons out of the total n presynaptic neurons is binomial $f(n, k, r) = \binom{n}{k} (r\Delta t)^k (1 - r\Delta t)^{n-k}$, which in the regime of large n and small $r\Delta t$ agrees with a Poisson distribution with parameter $nr\Delta t$.

In the rest of this section, we take the input to the neuron as stationary homogeneous poissonian inhibitory and excitatory spike trains. In this case, the number of spikes in a time interval Δt is stochastic and poissonly distributed with following distribution :

$$p(k_{[t, t+\Delta T]}) = (\lambda\Delta T)^k \frac{e^{-\lambda\Delta T}}{k!}$$

The output firing rate of the neuron is depicted in Fig.10(Left). In comparison to the output curve of the constant input (Fig.9), this curve is smoother and the transition from the silent state to the active state does not show a sharp jump. Sufficiently below the critical inhibition value, in the drift-dominated regime, the neuron output for Poisson and constant input

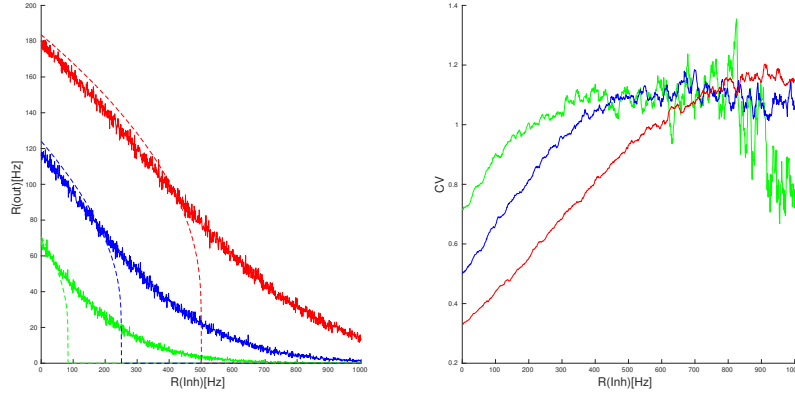


FIGURE 10. (Left) Firing rates of a neuron receiving three excitatory Poisson input with different rates (Red curve corresponds the highest) vs. the Poisson inhibitory input rate. Dashed lines are the response of the neuron to the constant input with a magnitude equal to Poisson rates. (Right) Coefficient of variation of the spike intervals of a neuron receiving Poisson inputs of the same rates as in the left graph. Near cutoff, neuron fires with CV close to one.

matches, however, close to this point the fluctuation effect caused by stochastic arrival of spikes is more evident. Moreover, the stochasticity in the input leads to stochastic firing at the output. Fig.10(Right) shows how the coefficient of variation (CV) of the firing time intervals of the output spike train changes by changing inhibitory input. This quantity is defined as:

$$CV(\delta t) = \frac{\sigma_{\delta t}}{\langle \delta t \rangle}$$

where δt is the set of firing time intervals of the target neuron subjected to a stationary Poisson input. When excitatory input is much stronger than the inhibitory one, the output firing pattern becomes more regular and the CV value is small. However, close to the inhibition cutoff, CV is getting close to unity, which is a characteristic of the Poisson point process.

2.3.1. Potential Distribution of a Neuron Receiving Poisson Input. The Poisson input in the limit of high firing rate and small synaptic weights can be approximated by a diffusion process. Suppose, in the time interval $[t, t + dt]$, $N(t, t + dt)$ excitatory spikes arrive at the cell each with synaptic strength w_e . As the spike arrival is a Poisson process with the rate λ , the distribution of $N(t, t + dt)$ is Poisson and all the cumulants of the random variable N would be equal to λdt . This leads to the following cumulants for $I(t, t + dt) = w_e N(t, t + dt)$:

$$\begin{aligned}\kappa_1 &= \langle I_{t,t+dt} \rangle dt = w_e \lambda dt \\ \kappa_2 &= \text{Var}(I_{t,t+dt}) = w_e^2 \lambda dt \\ \kappa_3 &= w_e^3 \lambda dt\end{aligned}$$

Higher cumulants can be ignored if we assume that $w_e^3 \lambda$ goes to zero in the limit of a high number of afferents. In theory, this can be achieved by assuming weights to scale as $w_e = \frac{W}{\sqrt{k}}$ in which k is the number of presynaptic neurons. In this case, $\lambda \sim O(k)$ and the average excitatory and inhibitory currents are each of order $O(\sqrt{k})$, the variance of the current is of $O(1)$ and higher cumulants vanishes in the limit of large k . In this case, one can consider $I(t, t + dt)$ to be a Gaussian random variable with the mean and variance according to the above equation. It can also be written as follows:

$$I(t)dt = w_e \lambda dt + w_e \sqrt{\lambda} dW_t$$

where W_t is a Wiener process.

It should be noted that with the aforementioned scaling of the synaptic weights both the inhibitory and excitatory rates diverge in the limit of $k \rightarrow \text{infy}$. Therefore, a nontrivial output firing requires a balance of the average inhibition and excitation.

In the conductance based model, the input to the cell causes a change in the conductance. As the input is stochastic, the conductance is also a stochastic variable which can be written as :

$$\begin{aligned}g(t) &= \int_{-\text{inf}}^t g_0 e^{-\frac{t-s}{\tau}} I(s) ds \\ &= \int_{-\text{inf}}^t e^{-\frac{t-s}{\tau}} g_0 w_e \lambda ds + \int_{-\text{inf}}^t e^{-\frac{t-s}{\tau}} g_0 w_e \sqrt{\lambda} dW_s\end{aligned}\tag{2.11}$$

The second term is the integral of a Wiener process with an exponential kernel. For the stochastic process $Y_t = \int_{-\text{inf}}^t f(s) dW_s$, we can easily verify that:

$$\begin{aligned}\langle Y_t \rangle &= 0 \\ \langle Y_t^2 \rangle &= \int_{-\text{inf}}^t f(s)^2 ds\end{aligned}$$

If we consider a stationary and homogeneous Poisson process as the input, $g(t)$ would also attain a stationary probability distribution. Using the above equation, mean and variance of $g(t)$ would reach following limits :

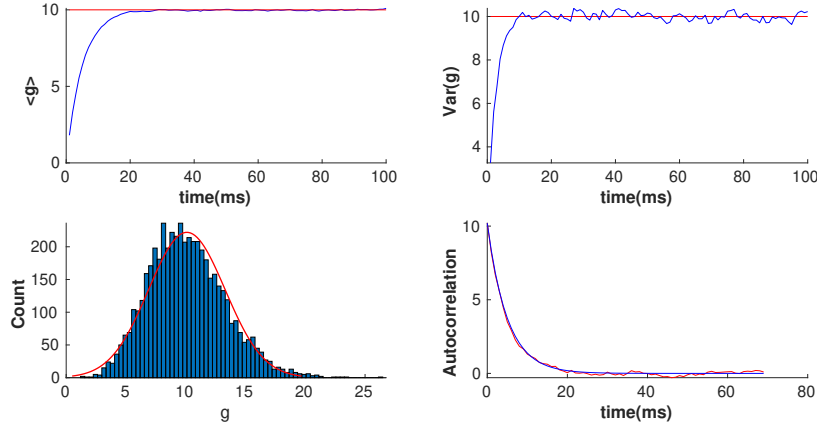


FIGURE 11. From Top-left to Bottom-right: Mean, Variance, stationary probability distribution, and auto-correlation of the conductance $g(t)$ of a neuron receiving Poisson input, respectively. The red lines are the values calculated by the diffusion approximation and the red curve in the bottom left plot is the Gaussian distribution with the mean and variance as derived in the text. The auto-correlation matches equation (2.13). This figure shows diffusion approximation is valid.

$$\begin{aligned}\langle g \rangle &= \tau g_0 w_e \lambda \\ \text{Var}(g) &= \frac{\tau g_0^2 w_e^2 \lambda}{2}\end{aligned}\tag{2.12}$$

The same argument as before justify that higher cumulants would vanish and one can assume $g(t)$ to reach a stationary Gaussian probability distribution with the mean and variance as above. Covariance of this process can be derived by direct multiplication of $g(t)$ and $g(t')$ and averaging over noise term from equation (2.11). when $t' > t$ we have:

$$\langle g(t)g(t') \rangle - \langle g(t) \rangle \langle g(t') \rangle = \text{var}(g) e^{-\frac{(t' - t)}{\tau}}\tag{2.13}$$

The same procedure applies to the inhibitory currents. Fig.11 shows statistics of the conductance $g(t)$ and the applicability of the diffusion approximation. If we assume the synaptic time scale, τ , is very small in comparison to the membrane potential time scale, one can ignore the cross-correlation at different time points and consider $Y_t = g(t) - \langle g \rangle$ as Gaussian white noise. In this limit :

$$\lim_{\tau \rightarrow 0} \langle Y_t Y_s \rangle = 2\tau \text{var}(g) \lim_{\tau \rightarrow 0} \frac{e^{-\frac{(s-t)}{\tau}}}{2\tau} = 2\tau \text{var}(g) \delta(t-s)$$

This leads to a stochastic differential equation for the membrane potential evolution in the conductance-based model, when $v(t) < V_{th}$:

$$\begin{aligned} C \frac{dv(t)}{dt} &= [g_{Leak}(v_{Leak} - v(t)) + g_0 w_e \lambda_e \tau (v_{Rexc} - v(t)) + g_0 w_i \lambda_i \tau (v_{Rinh} - v(t))] \\ &+ \xi_{exc}(t)(v_{Rexc} - v(t)) + \xi_{inh}(t)(v(t) - v_{Rinh}) \\ &\equiv [a - bv] + \xi_{exc}(t)(v_{Rexc} - v(t)) + \xi_{inh}(t)(v(t) - v_{Rinh}) \end{aligned} \quad (2.14)$$

Where $\xi_{exc}(t)$ and $\xi_{inh}(t)$ are purely random Gaussian process :

$$\begin{aligned} \langle \xi_{exc}(t) \rangle &= \langle \xi_{inh}(t) \rangle = 0 \\ \langle \xi_{exc}(t) \xi_{exc}(t') \rangle &= \tau^2 g_0^2 w_e^2 \lambda_e \delta(t-t') \equiv D_e \delta(t-t') \\ \langle \xi_{inh}(t) \xi_{inh}(t') \rangle &= \tau^2 g_0^2 w_i^2 \lambda_i \delta(t-t') \equiv D_i \delta(t-t') \end{aligned}$$

The first line of this equation is the deterministic evolution of the potential. We have defined a and b as coefficients of the drift term. When the fixed point of the deterministic term, $v_{det}^{inf} = V_{st} = \frac{a}{b}$ as defined by equation (2.9) is greater than V_{th} , the effect of fluctuations is marginal and the firing of neuron is governed by the drift term. However, when V_{st} is below the threshold fluctuations in the input can result in the firing of the neuron. Fokker-Planck equation corresponding to Eq.(2.14) in Ito interpretation reads as,

$$\begin{aligned} \frac{\partial p(v, t)}{\partial t} &= -\frac{1}{C} \frac{\partial}{\partial v} [(a - bv)p(v, t)] + \frac{1}{C^2} \frac{D_e}{2} \frac{\partial^2}{\partial v^2} (v_{Rexc} - v(t))^2 p(v, t) + \\ &\frac{1}{C^2} \frac{D_i}{2} \frac{\partial^2}{\partial v^2} (v_{Rinh} - v(t))^2 p(v, t) \equiv -\frac{\partial}{\partial v} J(v, t) \end{aligned} \quad (2.15)$$

with the boundary condition $p(V_{th}, t) = 0$. Density current at $v = V_{th}$ is equivalent to the firing rate. This current is fed back to the equation at $v = V_r$ which can be written as a discontinuity in the membrane potential derivative,

$$J(v_r^+, t) - J(v_r^-, t) = J(v_{th}, t - t_{ref}) \equiv r(t - t_{ref})$$

Stationary probability distribution and firing rate would be obtained by solving the following equation:

$$J_{st}(v) = r_0 \Theta(v - V_r)$$

which is of following form :

$$\begin{aligned} \frac{1}{C} \{a - bv + \frac{1}{C} D_e (v_{Rexc} - v) + \frac{1}{C} D_i (v_{Rinh} - v)\} p(v) \\ - \frac{1}{C^2} \{ \frac{D_e}{2} (v_{Rexc} - v)^2 + \frac{D_i}{2} (v_{Rinh} - v)^2 \} \frac{dp(v)}{dv} = r \end{aligned} \quad (2.16)$$

for $V_r < v < V_{th}$.

Together with the normalization requirement $\int_{-\infty}^{V_{th}} p(v) dv + r_0 * t_{ref} = 1$ one can solve equation (2.16) for both stationary probability distribution and stationary firing rate. When V_{st} is sufficiently smaller than V_{th} , i.e. in the low firing rate regime, we can ignore the non-linearity caused by the threshold and write down the evolution of the mean and variance of the membrane potential as follows:

$$\begin{aligned} \frac{d\langle v(t) \rangle}{dt} &= \frac{1}{C} (a - b\langle v(t) \rangle) \\ \frac{dVar(v, t)}{dt} &= -\frac{2b}{C} Var(v, t) + \frac{1}{C^2} [D_e \langle (V_{Rexc} - v(t))^2 \rangle + D_i \langle (v(t) - V_{Rinh})^2 \rangle] \\ &= (-\frac{2b}{C} + \frac{D_e + D_i}{C^2}) Var(v, t) + \frac{1}{C^2} [D_e (V_{Rexc} - \langle v \rangle)^2 + D_i (V_{Rinh} - \langle v \rangle)^2] \end{aligned}$$

This leads to the stationary value for the average and the variance of the membrane voltage :

$$\langle v \rangle_{st} = \frac{a}{b} \quad (2.17)$$

$$Var(v)_{st} = \frac{1}{2bC - (D_e + D_i)} [D_e (V_{Rexc} - \langle v \rangle_{st})^2 + D_i (\langle v \rangle_{st} - V_{Rinh})^2]$$

As it can be seen from Fig.14-Bottom and Fig.15-Right, the stationary standard deviation of membrane potential in the case of the Poisson input does not show high sensitivity to the input rates when the stationary mean potential is fairly away from the threshold. In Fig.14-Bottom, increasing excitatory input rate by 60% causes 2% increase of $\sigma(V)_{st}$ on average for different values of $\langle v \rangle_{st}$. This can be speculated from equation (2.17) as both the input noise and drift term in the numerator and the denominator depend linearly on input rates. Suppose $\langle v \rangle_{st}$ is fixed for a set of inhibitory and excitatory rates, which means there is a linear relation of the form $\rho_E = \kappa \rho_I + c$ originating from the condition on the fixed stationary average membrane potential. In the limit of high rates, stationary variance approaches a constant value:

$$\begin{aligned}
Var(v)_{st} &= \frac{\sigma^2}{2bC} = \frac{\alpha - \frac{\beta}{\lambda_E}}{\gamma - \frac{\lambda_E}{\lambda_E}} & (2.18) \\
\frac{\alpha}{\gamma} &= \frac{w_E^2 \tau^2 g^2 (V_{Rexc} - \langle V_{st} \rangle)^2 + w_E w_i \tau^2 g^2 (V_{Rexc} - \langle V_{st} \rangle) (\langle V_{st} \rangle - V_{Rinh})}{w_E \tau g + w_e \tau g \frac{V_{Rexc} - \langle V_{st} \rangle}{\langle V_{st} \rangle - V_{Rinh}}} \\
&= \frac{\tau g_0 (V_{Rexc} - \langle V_{st} \rangle) (\langle V_{st} \rangle - V_{Rinh}) [w_E (V_{Rexc} - \langle V_{st} \rangle) + w_I (\langle V_{st} \rangle - V_{Rinh})]}{V_{Rexc} - V_{Rinh}} \\
\frac{\beta}{\eta} &= \frac{w_i \tau g_0 (\langle V_{st} \rangle - V_{Leak}) (\langle V_{st} \rangle - V_{Rinh})^2}{\langle V_{st} \rangle - V_{Leak}} \\
&= w_i \tau g_0 (\langle V_{st} \rangle - V_{Rinh})^2
\end{aligned}$$

when $\frac{\alpha}{\gamma} > \frac{\beta}{\eta}$, the stationary membrane potential's variance and output rate would increase by proportionl increase of both inhibitory and excitatory rates and reaches a constant value $\frac{\alpha}{\gamma}$. This condition translates to $w_E (V_{Rexc} - \langle V_{st} \rangle)^2 > w_I (V_{Rinh} - \langle V_{st} \rangle)^2$. As far as $\langle V_{st} \rangle$ is adequately lower than V_{th} , $w_E (V_{Rexc} - \langle V_{st} \rangle) \approx w_I (V_{Rinh} - \langle V_{st} \rangle)$ and the condition mentioned above holds because $(V_{Rexc} - \langle V_{st} \rangle)$ is greater than $(V_{Rinh} - \langle V_{st} \rangle)$ by a factor of value around 2.

One has to consider that Gaussian approximation is only legitimate in the case of small τ and low firing rate regime. We want to consider cases in which these two conditions are not satisfied. Firstly, in higher values of τ_{syn} and at the stationary values of the average membrane potential lower than the threshold (low firing regime), there is an inversion to the mentioned scenario. In this case, at sufficiently high values of the input rates, conditioned on constant average membrane potential, the variance of membrane potential and accordingly the output rate decrease. (Fig.14-Top). This is due to the filtering effect of the input by the gradual decay of the synaptic conductances. At the end of this section, using the method of τ -expansion, we will consider autocorrelation in synaptic conductance and give more insight into this observation. The filtering of the high-frequency signal by the slow conductances is a mechanism of gain control. In general, the decay and the rise time of the inhibitory synapses are longer than the excitatory ones which would highlight the inhibitory input as the overall strength of it increases through temporal persistence. Besides, the voltage-dependent inhibitory current is higher at higher values of the membrane potential. The balanced average membrane potential is somewhere in the mid-range. Longer synaptic decay time constant, higher synaptic strength, delay, and potential dependence of the inhibitory synapses increase the overall inhibition strength

and compensate for the smaller number of them in comparison with excitatory synapses. This should be noted that output rates on the constant voltage level line with balanced input at $V = -57mv$, vary linearly with the input rates at moderate values of rates corresponding to low firing rate regime (Fig.14-Top).

On the other hand, when the stationary average membrane potential locates right at the threshold value, in conflict with the low firing regime assumption, equation (2.17) does not hold and higher rates of balanced input lead to a higher output rate independent of the value of τ_{syn} (Figure.14-Middle). Moreover, output rate varies in $\sqrt{I_{in}}$ trend. For analyzing the low firing rate regime, in subsection (2.3.3), we would linearize the output rate around the midpoint of the neuron potential range, i.e. at $V = -57mv$.

In the low firing regime, the stationary probability distribution can be approximated as:

$$P_{st}(V) = \frac{1}{\sqrt{2\pi}\sigma_{V(st)}} \exp\left(-\frac{(V - \langle V \rangle)^2}{2\sigma^2}\right) + c\delta(V - V_{Rest}) \quad V < V_{th}$$

$$P_{st}(V) = 0 \quad V \geq V_{th}$$

Stationary firing rate is derived from equation (2.16) by plugging in the Gaussian approximation for stationary potential probability density $P(V, t \rightarrow \infty) = N(\langle V \rangle, \sigma_{V(st)})$:

$$r = \frac{1}{C^2} \frac{1}{2} D(V_{th})^2 \frac{dp(V)}{dV} \Big|_{V=V_{th}} = -\frac{b}{C} \frac{D(V_{th})^2}{D(\langle V \rangle)^2} * \frac{(V_{th} - \langle V \rangle)}{\sigma_{V(st)}\sqrt{2\pi}} \exp\left(-\frac{(V_{th} - \langle V \rangle)^2}{2\sigma_{V(st)}^2}\right) \quad (2.19)$$

$$\approx \frac{b}{\sqrt{\pi}C} \frac{(V_{th} - \langle V \rangle)}{\sqrt{2}\sigma_{V(st)}} \left(1 - \frac{(V_{th} - \langle V \rangle)^2}{2\sigma_{V(st)}^2}\right)$$

It should be clear that at fixed value of $\langle V \rangle$, higher stationary variance leads to higher output rate in the Gaussian approximation. Fig.12 and Fig.13 show the Gaussian approximation for the membrane potential probability density and the firing rate approximation based on equation (2.19).

We can improve the approximation for the statistics of potential distribution (equation 2.17) and the firing rate (equation 2.19) by considering the autocorrelation in the conductance. We can use the τ expansion method to account for the first-order corrections to the Fokker-Planck equation. The equation $\frac{dv(t)}{dt} = f(v) + \eta(t)g(v)$ where $\eta(t)$ is colored Gaussian noise with the correlation,

$$\langle \eta(t)\eta(t') \rangle = \frac{H}{\tau} e^{-\frac{(t-t')}{\tau}}$$

corresponds to the following Fokker-Planck equation derived by the expansion with respect to τ :

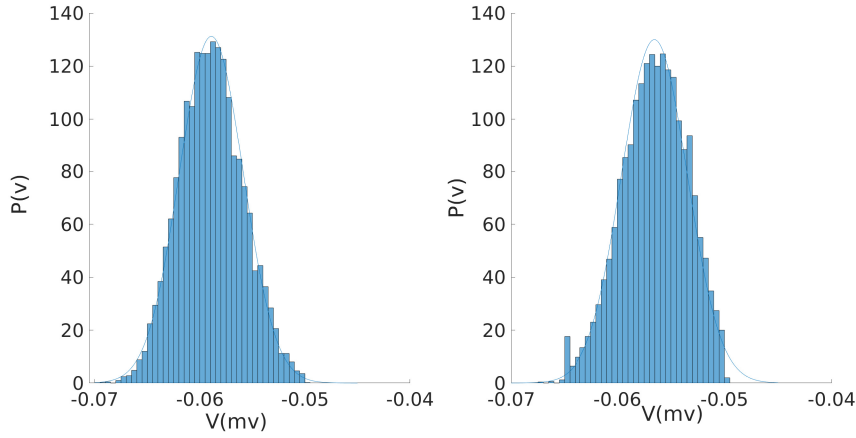


FIGURE 12. Membrane potential distribution and Gaussian approximation (Blue lines) for two different sets of inhibitory and excitatory Poisson inputs. The average membrane potential values are -0.59mv (Left) and -0.56mv (Right)

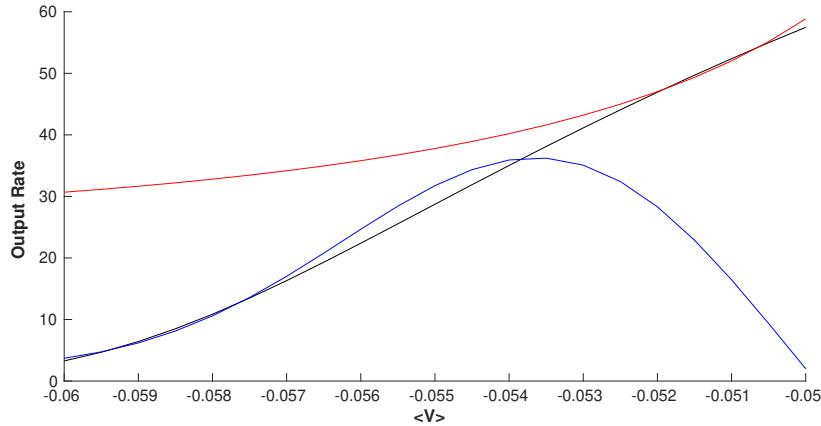


FIGURE 13. Firing rate approximation by Gaussian assumption of equation (2.19) (blue) and by near-threshold high firing assumption (red) of Eq.(2.25) in the next subsection (2.3.2) are compared with simulation result (black curve). Here, we fix inhibitory input and select a value of excitatory input rate that leads to a specific mean stationary membrane potential shown in the x-axis.

$$\begin{aligned}
\frac{\partial p(v, t)}{\partial t} &= -\frac{\partial}{\partial v}[f(v)p(v, t)] + H\frac{\partial}{\partial v}g(v)\frac{\partial}{\partial v}\{g(v)[1 + \tau g(v)(\frac{f(v)}{g(v)})']p(v, t)\} \\
&= -\frac{\partial}{\partial v}[(f(v) + Hg(v)g'(v))p(v, t)] + H\frac{\partial^2}{\partial v^2}\{g(v)^2p(v, t)\} \\
&\quad - \tau H\frac{\partial}{\partial v}\{g'(v)(g(v)f'(v) - g'(v)f(v))p(v, t)\} \\
&\quad + \tau H\frac{\partial^2}{\partial v^2}\{g(v)(g(v)f'(v) - g'(v)f(v))p(v, t)\}
\end{aligned}$$

In our case $H_e = \frac{\tau^2 g_0^2 w_e^2 \lambda_e}{2} = \frac{D_e}{2}$, which results in:

$$\begin{aligned} \frac{\partial p(v, t)}{\partial t} = & -\frac{1}{C} \frac{\partial}{\partial v} \{(a - bv + F(v))p(v, t)\} \\ & + \frac{D_e}{2C^2} \frac{\partial^2}{\partial v^2} \{G_e(v)p(v, t)\} + \frac{D_i}{2C^2} \frac{\partial^2}{\partial v^2} \{G_i(v)p(v, t)\} \end{aligned}$$

where:

$$\begin{aligned} F(v) &= \frac{D_e}{2C} [-2(v_{Rexc} - v(t)) - \frac{\tau}{C}(a - bV_{Rexc})] + \frac{D_i}{2C} [-2(v_{Rinh} - v(t)) - \frac{\tau}{C}(a - bV_{Rinh})] \\ G_e(v) &= (v_{Rexc} - v(t))^2 + \frac{\tau}{C}(v_{Rexc} - v(t))(a - bV_{Rexc}) \\ G_i(v) &= (v_{Rinh} - v(t))^2 + \frac{\tau}{C}(v_{Rinh} - v(t))(a - bV_{Rinh}) \end{aligned}$$

With these corrections to the drift and the diffusion terms, we can in a similar approach find the corresponding equations for the firing rate and stationary potential distribution similar to equation (2.19) and stationary value of mean and variance of the potential distribution in a low firing rate regime similar to equation (2.17). Fig.14 (Bottom) shows that these corrections lead to a better approximation of the stationary membrane potential variance in a low firing rate regime. Stationary variance of the membrane potential decreases in higher values of τ_{syn} . From above equation it can also be seen that at fixed value of stationary average potential, higher rates in excitatory and inhibitory input would lead a to lower stationary variance and lower rates.

Fig.15 shows the evolution of mean and variance of the membrane potential of a population of neurons each receiving an inhibitory Poisson input with rate λ_i and different excitatory input with rate λ_e with τ - expansion approximation and without.

2.3.2. Firing Rate and Interspike intervals' CV Near the Threshold.

When excitatory and inhibitory currents are matched in a way that stationary membrane potential V_{st} would be close to the firing threshold V_{th} , approximations in the previous section would not be correct. Here, we calculate the mean and the variance of the interspike intervals when the neuron receives Poisson input. We use the approximation that fluctuations in the input are weekly dependent on the voltage level. Therefore, our problem is reduced to the well known problem of the first passage time of a Brownian particle evolving as $\frac{dx}{dt} = -kx + \xi(t)$ to reach the threshold a . In which ξ is white noise with variance σ . We want to approximate results for first passage time moments when the stationary membrane potential is close to the threshold. The goal here is to obtain approximate analytical results for the firing rate and the CV of interspike intervals to identify the conditions

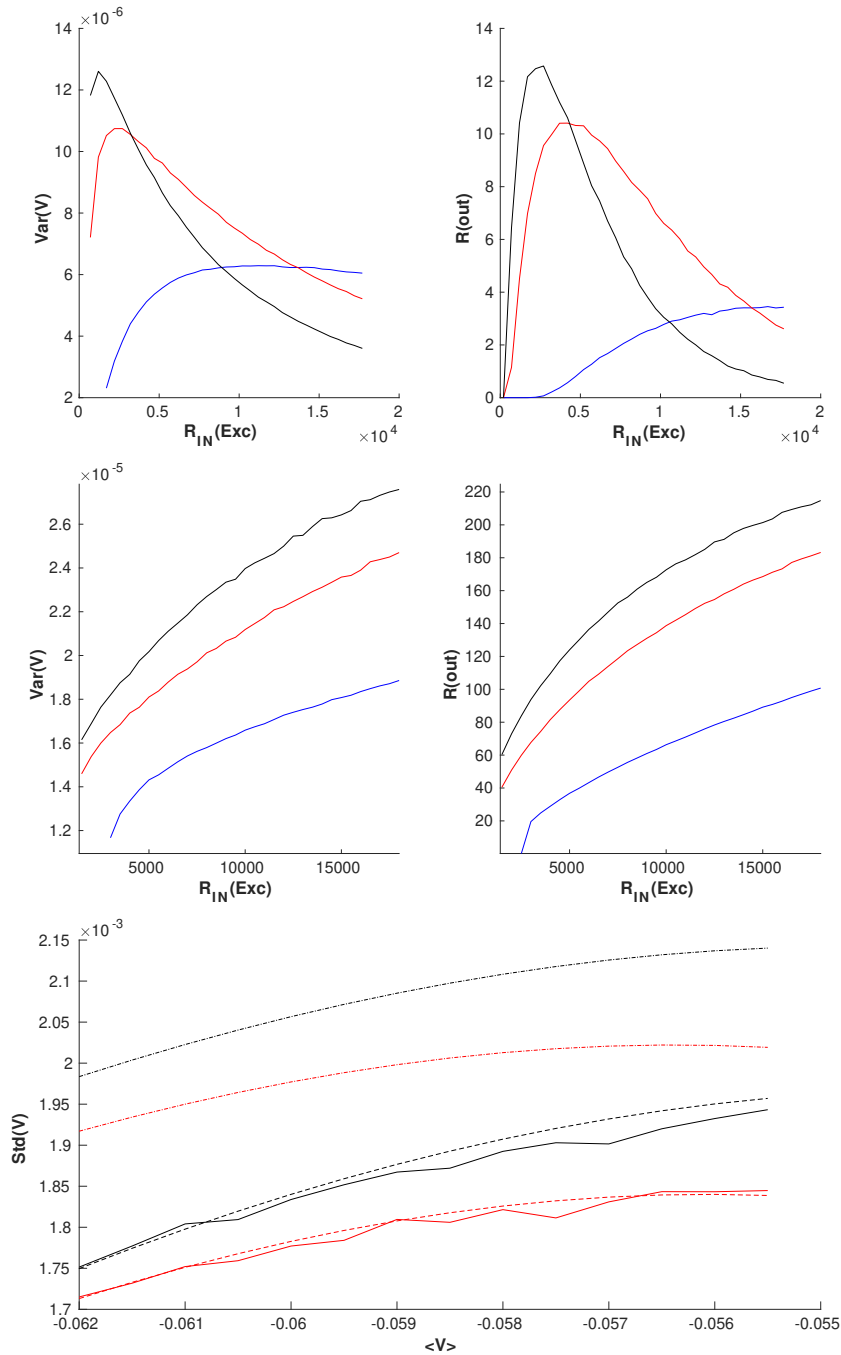


FIGURE 14. (Top-Left and Top-Right) Stationary variance of the membrane potential and the output firing rates, when the excitatory rate(x-axis) and inhibitory rates are balanced so that average membrane potential is at $-57mv$ for three different values of $\tau_{syn} = [1$ (Blue), 3 (Red), 5 (Black)] ms. (Middle) Same with average membrane potential tuned at the threshold value $-50mv$. (Bottom) Stationary potential variance for a neuron receiving two different excitatory input rates, $1000Hz$ (red) and $1600Hz$ (blue), and corresponding inhibitory input, which places the average potential at a specific value shown in the x-axis. Solid lines are simulation results, dashed lines correspond to low firing regimes with tau approximation, and fine dashed lines show Gaussian approximation. ($\tau_{syn} = 2.5ms$)

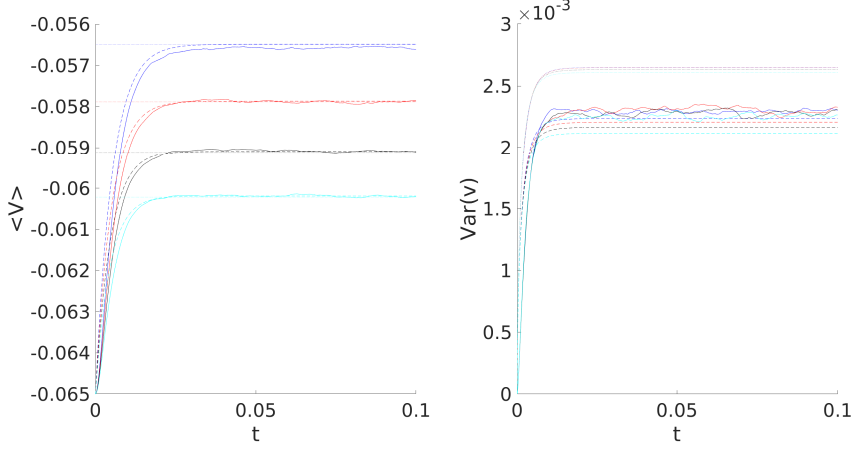


FIGURE 15. Evolution of the mean and the variance of the potential distribution of a population of neurons each receiving a fixed equal value of inhibitory input rate but different excitatory rates. Dashed lines are the trajectories determined from Gaussian noise approximation and the dotted lines are derived from the tau expansion method. The approximation by tau expansion improves the estimation of variance. ($\tau_{syn} = 2.5ms$)

for the output Poisson firing and the optimal linearization of the output rate in the low firing rate regime.

For the case of the Poisson current to the cell, the voltage fluctuates around the mean value $\langle V \rangle$. We assume that this mean value is close to the threshold and the magnitude of fluctuations is constant. Taking $x = V(t) - \langle V \rangle$, we model the voltage dynamic by the aforementioned Ornstein-Uhlenbeck process with :

$$\sigma^2 = \frac{1}{C^2} \left\{ \frac{D_e}{2} (v_{Rexc} - \langle V \rangle)^2 + \frac{D_i}{2} (v_{Rinh} - \langle V \rangle)^2 \right\} \quad (2.20)$$

$$k = \frac{1}{C} (g_{Leak} + g_0 w_e \lambda_e \tau + g_0 w_i \lambda_i \tau)$$

$$a = V_{th} - \langle V \rangle$$

k is the drift and a is the first passage time threshold. To determine first passage time(FPT) statistics let us first review the recursive formula for FPT moments as discussed in Siegert [114]. Suppose stochastic process Y_t with the conditional probability density $P(y, t|y_0)$ satisfies the following Fokker-Planck equation :

$$\frac{\partial p(y, t|y_0)}{\partial t} = -\frac{\partial}{\partial y} [A(y)p(y, t|y_0)] + \frac{1}{2} \frac{\partial^2}{\partial y^2} (B(y)p(y, t|y_0))$$

with the initial and the boundary conditions $P(y, t_0|y_0) = \delta(y - y_0)$ and $P(\pm\infty, t|y_0) = 0$, respectively .

First passage time probability density $\rho(\Theta|t, x_0)$ of the stochastic process following the above Fokker-Planck equation would satisfy:

$$\rho(\Theta|t, s) = -2 \frac{\partial}{\partial t} \int_{-\infty}^s P(\Theta, t|y) dy$$

Based on this equation, we can write recursion formula for moments of FPT with diffusion strength $B(y)$ and drift term $A(y)$ as follows:

$$t_n(\Theta|y_0) = n \int_{y_0}^{\Theta} \frac{2dz}{B(z)W(z)} \int_{-\infty}^z W(x)t_{n-1}(\Theta|x)dx \quad (2.21)$$

$t_0 = 1$ and $W(x)$ is the stationary probability distribution:

$$W(x) = \frac{C}{B(y)} \exp\left[\int dy \frac{2A(y)}{B(y)}\right]$$

Specially for the first moment we have :

$$t_1(\Theta|y_0) = \int_{y_0}^{\Theta} \frac{2dz}{B(z)W(z)} \int_{-\infty}^z W(x)dx \quad (2.22)$$

We want to apply this last formula in our case. Let us take $x = V - \frac{a}{b}$, $x_0 = V_0 - \frac{a}{b}$ and $x_{th} = V_{th} - \frac{a}{b}$ where $\frac{a}{b} = \langle V \rangle_{st}$ as in equation (2.17). Then random variable x evolves as $\frac{dx}{dt} = -bx + \sigma(x)\xi(t)$ where ξ is white noise with unit variance and :

$$\sigma^2(x) = \frac{1}{C^2} \{D_e(v_{Recc} - \frac{a}{b} + x)^2 + D_i(v_{Rinh} - \frac{a}{b} + x)^2\} \quad (2.23)$$

$$b = \frac{1}{C} (g_{Leak} + g_0 w_e \lambda_e \tau + g_0 w_i \lambda_i \tau)$$

For the case of the Poisson current to the cell, if the mean value is close to the threshold, the magnitude of fluctuation does not vary much in the interval $[V_{rest}, V_{th}]$, therefore in the following we neglect dependence of σ on x . Using equations (2.21) and (2.22), the average first passage time can be written as :

$$t_1(x_{th}|x_0) = \frac{\sqrt{\pi}}{b} \int_{x_0 \sqrt{\frac{b}{\sigma^2}}}^{x_{th} \sqrt{\frac{b}{\sigma^2}}} e^{z^2} (1 + erf(z)) dz$$

Where $erf(\cdot)$ is the Gauss error function. Writing $x_0 = (V_{leak} - V_{th}) + (V_{th} - \frac{a}{b}) = -\Theta + x_{th}$ in which $\Theta := V_{th} - V_{Leak}$, we have:

$$t_1(x_{th}|x_0) = \frac{\sqrt{\pi}}{b} \left[\int_0^{x_{th}} \sqrt{\frac{b}{\sigma^2}} e^{z^2} (1 + erf(z)) - \int_0^{(-\Theta+x_{th})} \sqrt{\frac{b}{\sigma^2}} e^{z^2} (1 + erf(z)) \right]$$

Taking $y := x_{th} \sqrt{\frac{b}{\sigma^2}}$ and $\theta := \Theta \sqrt{\frac{b}{\sigma^2}}$ and using the following series expansions in y ,

$$\begin{aligned} \int_0^y e^{z^2} dz &= y + \frac{y^3}{3} + \frac{y^5}{10} \dots \\ \int_0^y e^{z^2} erf(z) dz &= \frac{1}{\sqrt{\pi}} (y^2 + \frac{y^4}{3} + \frac{4y^6}{45} \dots) \\ \int_0^{-\theta+y} e^{z^2} (1 + erf(z)) dz &= \int_0^{-\theta} e^{z^2} (1 + erf(z)) dz + y(e^{-\theta^2} (1 + erf(-\theta))) \\ &\approx \int_0^{-\theta} e^{z^2} (1 + erf(z)) dz \equiv \kappa \end{aligned}$$

we can write down the approximation for the mean passage time as:

$$\begin{aligned} t_1(x_{th}|x_0) &= -\frac{\sqrt{\pi}}{b} \kappa + \left(\frac{a}{b} - V_{rest}\right) \sqrt{\frac{b}{\sigma^2}} \frac{\sqrt{\pi}}{b} + \frac{\sqrt{\pi}}{b} \left[(V_{th} - \frac{a}{b})\right] \sqrt{\frac{b}{\sigma^2}} \\ &\quad + \frac{1}{b} \left[(V_{th} - \frac{a}{b}) \sqrt{\frac{b}{\sigma^2}}\right]^2 \end{aligned} \tag{2.24}$$

Where κ is the last integral in the approximations mentioned above. It can be seen from equation (2.18) that the factor $\sqrt{\frac{b}{\sigma^2}}$ in regime of large balanced rates of excitatory and inhibitory inputs asymptotically approaches a constant value. Therefore, we can approximate the κ to be very weakly dependent on input rates and take it as a constant factor. Altogether, we can write down the average rate of firing, $r = \frac{1}{t_1(x_{th}|x_0)}$, in the case that average stationary potential is close to threshold as :

$$r = \frac{b}{\sqrt{\pi}} \left(\frac{1}{\kappa + (V_{th} - \frac{a}{b}) \sqrt{\frac{b}{\sigma^2}}} \right) \tag{2.25}$$

In Fig.13, we have plotted this rate approximation which is of minimal error when average potential is near threshold. From equations (2.24) and

(2.25), we can see if $\langle v \rangle = \frac{a}{b}$ is constant for balanced inhibitory and excitatory input rates, the output rate of the neuron would be linearly proportional to the input rates via the factor b . Moreover, the output rate would decrease as $\frac{1}{x_{th}}$ with the increase of the distance of the stationary average potential from the threshold.

Next, we want to write down the variance of the first passage time. From the recursion formula (2.21), we have :

$$t_2(x_{th}|x_0) = \frac{2\pi}{b^2} \int_{-\infty}^{x_{th}\sqrt{\frac{b}{\sigma^2}}} e^{z^2} (1 + \text{erf}(z))^2 \int_z^{x_{th}\sqrt{\frac{b}{\sigma^2}}} dr e^{r^2} \Theta(r - x_0\sqrt{\frac{b}{\sigma^2}})$$

After some straightforward calculations we arrive at:

$$\begin{aligned} t_2(x_{th}|x_0) &= \frac{2\sqrt{\pi}}{b} t_1(x_{th}|x_0) \left[\int_0^{x_{th}\sqrt{\frac{b}{\sigma^2}}} e^{z^2} (1 + \text{erf}(z)) \right] \\ &+ \frac{2\sqrt{\pi}}{b^2} \ln(2) \left[\int_0^{x_{th}\sqrt{\frac{b}{\sigma^2}}} e^{z^2} - \int_0^{x_0\sqrt{\frac{b}{\sigma^2}}} e^{z^2} \right] \\ &- \frac{2\sqrt{\pi}}{b^2} \left[\phi\left(x_{th}\sqrt{\frac{b}{\sigma^2}}\right) - \phi\left(x_0\sqrt{\frac{b}{\sigma^2}}\right) \right] \\ &- \frac{2\sqrt{\pi}}{b^2} \left[\psi\left(x_{th}\sqrt{\frac{b}{\sigma^2}}\right) - \psi\left(x_0\sqrt{\frac{b}{\sigma^2}}\right) \right] \end{aligned}$$

where functions ϕ and ψ are multi-variable integrals containing powers of erf and e^{x^2} in the integrand with following series expansion :

$$\begin{aligned} \phi(y) &= \sum_{n=0}^{\infty} \frac{y^{2n+3}}{(n+1)!(2n+3)} \sum_{k=0}^n \frac{1}{2k+1} \\ \psi(y) &= \sum_{n=0}^{\infty} \frac{2^n y^{2n+4}}{(n+2)(2n+3)!!} \sum_{k=0}^n \frac{1}{k+1} \end{aligned}$$

Rewriting the first term in the bracket in terms of first passage time average and considering only the terms of the first order in x_{th} we arrive at:

$$\begin{aligned}
t_2(x_{th}|x_0) &= 2t_1(x_{th}|x_0)[t_1(x_{th}|x_0) + \frac{\sqrt{\pi}}{b} \int_0^{(-\Theta+x_{th})\sqrt{\frac{b}{\sigma^2}}} e^{z^2} (1 + erf(z))] \\
&+ \frac{2\sqrt{\pi}}{b^2} \ln(2) [\int_0^{x_{th}\sqrt{\frac{b}{\sigma^2}}} e^{z^2} - \int_0^{x_0\sqrt{\frac{b}{\sigma^2}}} e^{z^2}] \\
&- \frac{2\sqrt{\pi}}{b^2} [\phi(x_{th}\sqrt{\frac{b}{\sigma^2}}) - \phi(x_0\sqrt{\frac{b}{\sigma^2}})] \\
&- \frac{2\sqrt{\pi}}{b^2} [\psi(x_{th}\sqrt{\frac{b}{\sigma^2}}) - \psi(x_0\sqrt{\frac{b}{\sigma^2}})] \\
&\approx 2t_1(x_{th}|x_0)^2 + \frac{2x_{th}\sqrt{\pi}}{b\sqrt{b}\sigma} \ln(2) + C(x_{th} = 0)
\end{aligned}$$

Where C is a negative number which is the sum of integrals at $x_{th} = 0$. Therefore, the expression for the CV of the time interval between spikes is :

$$CV^2 = \frac{Var(t)}{\langle t \rangle^2} \approx 1 + \frac{C}{t_1(x_{th}|x_0)^2} + 2\sqrt{\pi} \ln(2) \frac{\frac{x_{th}}{b\sqrt{b}\sigma}}{t_1(x_{th}|x_0)^2}$$

The second term is a negative number that monotonically goes to zero as x_{th} increases. In the limit of large x_{th} , both second and third terms go to zero, and CV approaches the value of one. However, in the near-threshold approximation, maximum of the third term is where CV is approaching the value one. Expanding this term in the powers of x_{th} , and equating the first derivative to zero, the maximum of this term is at :

$$x_{th}^{opt} := V_{th} - \langle V \rangle_{st} = \frac{\pi\sigma}{2\sqrt{b}} \quad (2.26)$$

As we have discussed in the following paragraphs after equations (2.18) and (2.24), $\frac{\sigma}{\sqrt{b}}$ reaches a constant value in high input rates from equation (2.18). This can be used to determine the value of $\langle V \rangle_{st}$ that leads to maximum CV. Fig.16 shows the CV of interspike interval for different sets of excitatory and inhibitory pairs of input. As can be seen, at the threshold, neurons' firing time intervals have lower variance, however, the CV approaches value one far away from the threshold. The value of the stationary membrane potential corresponding to the maximum value of the CV from the equation (2.26) is shown in the right diagram and it matches well with the actual values from the simulation. At $V_P := \langle V \rangle_{st}^{opt} \approx -0.56mv$, CV for different input rates show maximum independent of the rate values.

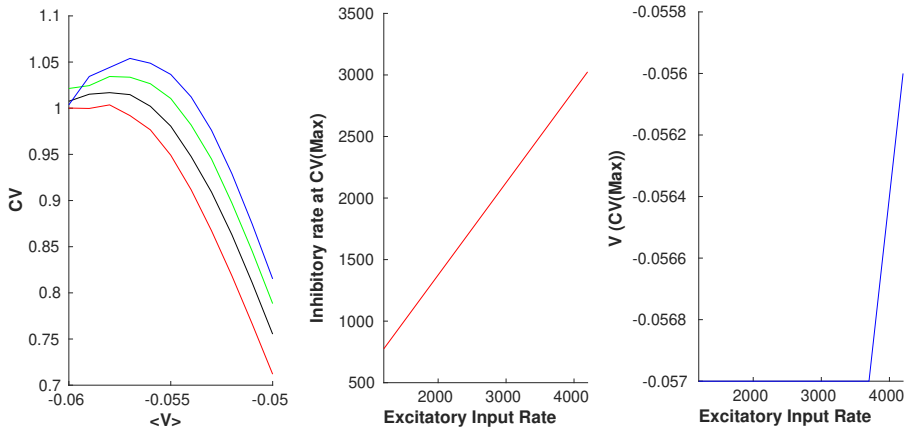


FIGURE 16. (Left) Interspike intervals CV for four different excitatory input rates and their corresponding inhibitory rates, which set the average membrane potential at each specified value shown in the x-axis. (Middle) Inhibitory rate vs. excitatory rate at the value of the maximum of CV . (Right) Membrane potential value at the value of the maximum of CV .

In the middle plot, we see the inhibitory rate that satisfies $CV = CV_{max}$ vary linearly with the excitatory rates. As can be seen, when the stationary membrane potential is approximately below V_P , CV of interspike intervals approaches the value of one, independent of values of inhibitory and excitatory rates. This is an indicator that output firing in response to Poisson Input is itself a Poisson point process when $\langle V \rangle_{st}$ lies below V_P . For a more conclusive result, one has to calculate higher moments or investigate the limit of FPT probability density when x_{th} is very large.

2.3.3. Linear Poisson Neuron Approximation. In this section, we want to show that linearizing the response curve of a neuron receiving Poisson current near V_P , introduced in the last subsection, leads to a good approximation for the firing rate of the neuron in a wide range of input rates. The linearization is around the line characterized by equation (2.9) with $V_{st} = V_P$ in the $\rho_{exc} - \rho_{inh}$ plane. This line corresponds to the balance of mean excitation and inhibition at V_P . On this balance line from equation (2.19), the output rate would depend linearly on the excitatory and inhibitory input rates (see Fig.17).

We want to linearize the output rate around V_P . For this purpose let us write equation of the plane passing through the line of current balance at V_P (Eq.(2.27)) and the tangent line in the (ρ_E, ρ_{out}) plane at some point $(\rho_I^0, \rho_E^0, \rho_{out}^0)$. Balance condition line for an excitatory neuron connected to k_{EE} excitatory neurons and k_{IE} inhibitory neurons each firing with the rate ρ_E and ρ_I , respectively, and receiving external excitatory rate ρ_{Ext} is of the following form:

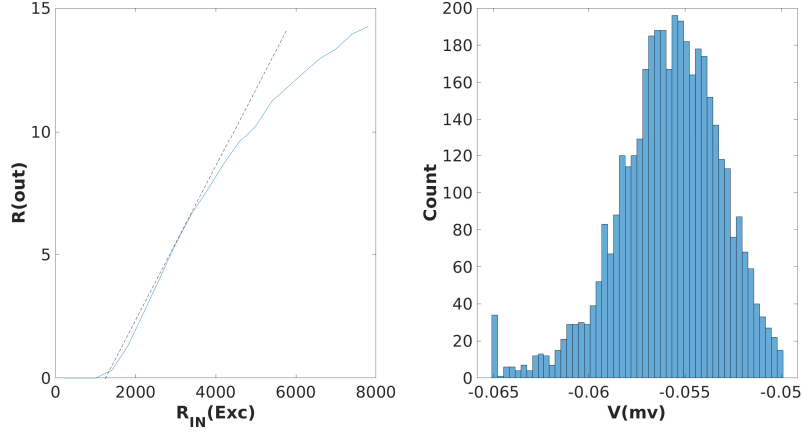


FIGURE 17. Response of a population of neurons receiving excitatory and inhibitory inputs balanced in a way that the drift term has a fixed point at $V_P = -0.56mv$. (Left) Output firing rate for different values of balanced inhibitory and excitatory input rates. The output rate changes semi-linearly on this line and firing in this regime that is driven by the fluctuation in the input causes the neuron to fire with Poisson point process statistics. (Right) The stationary potential distribution of the population of neurons, as can be seen, there is a reservoir of neurons close to the threshold while the average firing rate is about 20 Hz. Parameters used: $w_E = 0.5$, $w_I = 0.75$, $N_E = 7000$, $N_I = 0.25 * N_E$

$$\rho_E^e * k_{EE} = \frac{(V_{Rinh} - V_P) * g_{inh}^0 * w_{EI}}{g_{exc}^0 * w_{EE} * (V_P - V_{Rexc})} \rho_I * k_{EI} + \frac{g_{leak}(V_{rest} - V_P)}{\tau * g_{exc}^0 * w_{EE} * (V_P - V_{Rexc})} - \frac{\rho_{Ext}^e}{w_{EE}} \quad (2.27)$$

Let us rewrite this in a simpler form as $\rho_E^e = k\rho_I + C$. Equation of the balance line and the other tangent line in (ρ_E, ρ_{out}) plane would be of the following form, respectively:

$$\frac{(\rho_E - \rho_E^0)}{k} = \rho_I - \rho_I^0 = \frac{\rho_{out} - \rho_{out}^0}{\alpha_{OI}}$$

$$\frac{\rho_O - \rho_O^0}{\beta_{OE}} = \rho_E - \rho_E^0$$

Therefore, the equation of the plane passing through these lines is of the form:

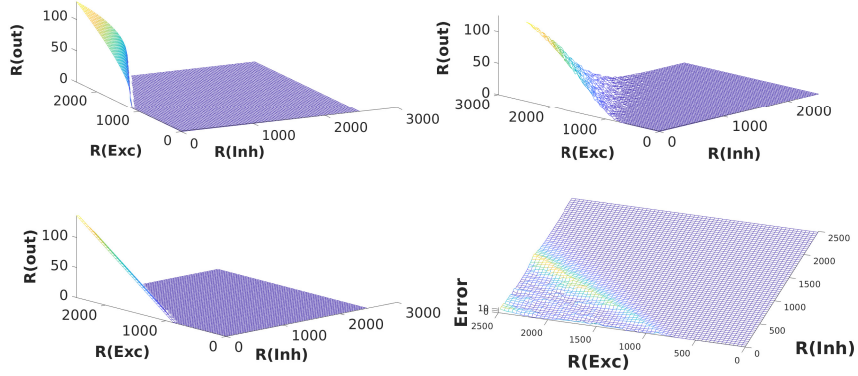


FIGURE 18. (Top left) Firing rate of a neuron w.r.t different values of constant inhibitory and excitatory input. (Top right) The same for the Poisson input. (Bottom Left) The linear approximation for the output on the critical line of Eq.(2.27). (Bottom right) The error of the linear neuron approximation.

$$(\rho_{out} - \rho_{out}^0) = \beta_{OE}(\rho_E - \rho_E^0) + (\alpha_{OI} - \beta_{OE}k)(\rho_I - \rho_I^0) \quad (2.28)$$

β_{OE} is derivative of the nonlinear response at the selected point in direction of ρ_E and α_{OI} is proportional to the change of output rate by changing inhibition and accordingly excitation on the balance line. These derivatives do not vary much on the balance line, therefore, the choice of the linearization point does not matter for us at this stage. This suggests that the plane of equation (2.28) is tangent to the ρ_{out} surface. This linear approximation would fail for very high excitatory input where neuron's saturation causes non-linearity. The linearization point is where the output firing curve has the lowest curvature, second derivative vanishes, which makes the approximation error minimal. Fig.18 shows the output firing rate of the target neuron and the linear approximation presented above.

In the next section, we want to investigate the homogeneous firing state of a network. For this purpose we will look at self consistency solutions $\rho_{out} = \rho_E(in) = \rho_E^*$ for an arbitrary value of inhibitory current. From equation (2.28) :

$$(1 - \beta_{OE})\rho_E^* = (\alpha_{OI} - \beta_{OE}k)(\rho_I - \rho_I^0) + \rho_O^0 - \beta_{OE}\rho_E^0$$

By putting in $k\rho_I^0 - \rho_E^0 = -C$ and dividing the above equation by β_{OE} , we arrive at :

$$\left(\frac{1}{\beta_{OE}} - 1\right)\rho_E^* = -k\rho_I - C + \frac{\alpha_{OI}}{\beta_{OE}}(\rho_I - \rho_I^0) + \frac{1}{\beta_{OE}}\rho_O^0$$

β_{OE} depends on the number of excitatory input to the cell, K_{EE} , and is related to the proportional change of output firing at the balance line to the change in the firing rate in each excitatory neuron. On the other hand, α_{OI} , proportional to change in the firing rate while fixing the balance condition, is much smaller than β_{OE} . Therefore, when K_{EE} is large, the self-consistency equation matches the balance line of equation (2.27) with a minimal error.

3. Interconnected Homogeneous Population of Excitatory and Inhibitory Neurons

In this section, we want to analyze the dynamics of a homogenous population of excitatory and inhibitory neurons. Like in the previous section, we will start by writing down FPE for membrane potential probability density. Assuming that neurons receive Poisson input, the equation for the membrane potential dynamic of an excitatory neuron in a homogeneously connected EI population is :

$$\begin{aligned} \frac{\partial p(v^E, t)}{\partial t} = & -\frac{1}{C} \frac{\partial}{\partial v^E} [(a - bv^E)p(v^E, t)] + \frac{1}{C^2} \frac{D_e}{2} \frac{\partial^2}{\partial v^{E2}} (v_{Rexc} - v^E(t))^2 p(v^E, t) + \\ & (3.1) \\ & \frac{1}{C^2} \frac{D_i}{2} \frac{\partial^2}{\partial v^{E2}} (v_{Rinh} - v^E(t))^2 p(v^E, t) \equiv -\frac{\partial}{\partial v} J(v^E, t) \end{aligned}$$

In which :

$$\begin{aligned} a = & g_{leak}V_{leak} + g_{exc}^0\tau V_{Rexc}(k_{EE}w_{EE}\rho_E + \lambda_{EE}) + g_{inh}^0\tau V_{Rinh}(k_{EI}w_{EI}\rho_I + \lambda_{EI}) \\ b = & g_{leak} + g_{exc}^0\tau(k_{EE}w_{EE}\rho_E + \lambda_{EE}) + g_{inh}^0\tau(k_{EI}w_{EI}\rho_I + \lambda_{EI}) \\ D_e = & \tau^2 g_0^2 [k_{EE}w_{EE}^2\rho_e + \lambda_{EE}] \\ D_i = & \tau^2 g_0^2 [k_{EI}w_{EI}^2\rho_I + \lambda_{EI}] \end{aligned}$$

With boundary condition for excitatory population as :

$$\begin{aligned} P(v^E = V_{th}, t) &= 0 \\ J(v_{Leak}^+, t) - J(v_{Leak}^-, t) &= J(v_{th}, t - t_{ref}) \equiv r(t - t_{ref}) \end{aligned}$$

In the above equations, w_{EE} and w_{EI} are average synaptic weights from an excitatory or inhibitory neuron to an excitatory neuron, respectively. k_{EE} and k_{EI} are the number of excitatory and inhibitory presynaptic neurons connected to each neuron in the excitatory population, respectively. λ_{EE} and λ_{EI} are external excitatory and inhibitory currents to the excitatory population which is supposed to be Poisson as well.

Stationary potential distribution and firing rates, if exist, are solutions to the following equations:

$$\begin{aligned} J_E^{st}(v^E) &= \rho_E^{st}\Theta(v^E - V_{Leak}) \\ J_I^{st}(v^I) &= \rho_I^{st}\Theta(v^I - V_{Leak}) \end{aligned}$$

The self consistency equation for excitatory rate can be written as:

$$\rho_E(t) = -\frac{1}{C^2} \left\{ \frac{D_e}{2} (v_{Rexc} - V_{th})^2 + \frac{D_i}{2} (v_{Rinh} - V_{th})^2 \right\} \frac{dp(v, t)}{dv} \Big|_{v=V_{th}} := f(\rho_E, \rho_I, \lambda_{EE}, \lambda_{EI})$$

The same sets of equation holds for $P(v^I, t)$ with $\rho_I(t) := g(\rho_E, \rho_I, \lambda_{IE}, \lambda_{II})$

Solving for the above-mentioned gain functions f and g is not analytically tractable for the EI population. These equations may have multiple solutions and changing control parameters can lead to Hopf and Saddle-node bifurcations, which in turn produce/destroy oscillation or produce/destroy pairs of fixed points. Solutions of the self-consistency equations for the firing rates are the stationary limits of the EI population rates, which are of the following form:

$$\rho_E^{st} = f(k_{EE}\rho_E^{st}, k_{EI}\rho_I^{st}, \lambda_{EE}, \lambda_{EI}) \quad (3.2-a)$$

$$\rho_I^{st} = g(k_{EI}\rho_E^{st}, k_{II}\rho_I^{st}, \lambda_{IE}, \lambda_{II}) \quad (3.2-b)$$

for $\rho_{exc}, \rho_{inh} \in [0, \rho_{max}]$.

Depending on the strength of the connections and the external inputs, equation (3.2) can have multiple solutions. Dynamics to the stationary limit can be phenomenologically approximated by the following mean field equations:

$$\begin{aligned} \frac{d\rho_E}{dt} &= -\frac{1}{\tau_m} (\rho_E(t) - f(k_{EE}\rho_E(t), k_{EI}\rho_I(t), \lambda_{EE}, \lambda_{EI})) \\ \frac{d\rho_I}{dt} &= -\frac{1}{\tau_m} (\rho_I(t) - g(k_{EI}\rho_E(t), k_{II}\rho_I(t), \lambda_{IE}, \lambda_{II})) \end{aligned} \quad (3.3)$$

Although it is possible to numerically investigate the FPE for EI populations and its bifurcation diagram, in the next subsections, we follow another approach by using linearized nullclines approximation and logistic function approximation for functions f and g . We will show that studying these models is appropriate for the bifurcation analysis and agree with the simulation results.

In the remaining of this work, in the simulations, we consider population of $N_{Exc} = 2 * 10^4$ and $N_{Inh} = 0.25 * N_{Exc}$ inhibitory spiking neurons with conductance-based currents introduced in section (1). Each excitatory neuron in the population is randomly connected to $k_{EE} = \frac{N_{Exc}}{100} = 200$ excitatory and $k_{EI} = \frac{k_{EE}}{4}$ inhibitory neurons and each inhibitory neuron is connected to $k_{IE} = k_{II} = \frac{k_{EE}}{4}$ excitatory and inhibitory neurons.

Weights of excitatory synaptic connections are in a range that 10 – 20 synchronous excitatory spikes are enough to depolarize the target neuron to the level of firing threshold when it is initially at rest at the time of the input arrival. Weights are being drawn from a log-normal probability density with low variance. Therefore, approximately, $O(\sqrt{k_{EE}})$ spikes are adequate for the firing. By assuming homogeneity in the population which means each neuron receives input with the same statistics, as we have discussed in the introduction, we can build a mean-field equation for the excitatory and inhibitory population in this sparse network.

3.1. Linearized Nullclines and Different Dynamic Regimes. Because function f in equation (3.2a) for stationary excitatory rate has a sigmoidal shape, this equation would have one or three solutions based on the value of the inhibitory rate. This is shown in Fig.19(Top-left) for three different total inhibitory currents. In a low to a moderate value of inhibition there exist three fixed points, i.e. intersections of the linear line with the sigmoidal gain function, at the quiescent state, the semi-linear section, and the high firing state. Increasing inhibitory input rate causes the nonlinear gain function to move to the right and at the point specified in the graph by a blue dot, the middle saddle and high fixed point annihilate each other through Saddle-node bifurcation. On the other hand, increasing external excitatory input will move the graph upward, which leads to the annihilation of the low fixed point and the saddle through another SN bifurcation. Fig.15(Top-right) shows the solutions to equation (3.2-a) for different values of total inhibitory current to the excitatory population. This is plotted for two different values of W_{EE} with the dashed curve corresponds to higher W_{EE} .

Similarly, Fig.19(BL) is the plot corresponding to the equation (3.2-b). Here, nonlinear Sigmoid function g is plotted for three different values of excitatory currents. There exist a single intersection point between the line passing through the origin and these curves, which means equation (3.2-b) has a unique solution for the stationary inhibitory rate at each specific excitatory input. Fig.19(BR) is the plot of the location of these intersections for different values of inhibitory input. As it can be seen in Fig.19, there exist a semi linear section in the nullcline graphs corresponding to solutions in the linear Poisson section of gain function. Based on linear Poisson approximation of the last section, equations for these lines in both excitatory and inhibitory nullcline graphs are :

$$\rho_E^e * k_{EE} = \frac{(V_{Rinh} - V_P) * g_{inh}^0 * w_{EI}}{g_{exc}^0 * w_{EE} * V_P} \rho_I * k_{EI} + \frac{g_{leak}(V_{rest} - V_P)}{\tau * g_{exc}^0 * w_{EE} * V_P} - \frac{\lambda_{EE}}{w_{EE}} \quad (3.4-a)$$

$$\rho_E^i * k_{IE} = \frac{(V_{Rinh} - V_P) * g_{inh}^0 * w_{II}}{g_{exc}^0 * w_{IE} * V_P} \rho_I * k_{II} + \frac{g_{leak}(V_{rest} - V_P)}{\tau * g_{exc}^0 * w_{IE} * V_P} - \frac{\lambda_{IE}}{w_{IE}} \quad (3.4-b)$$

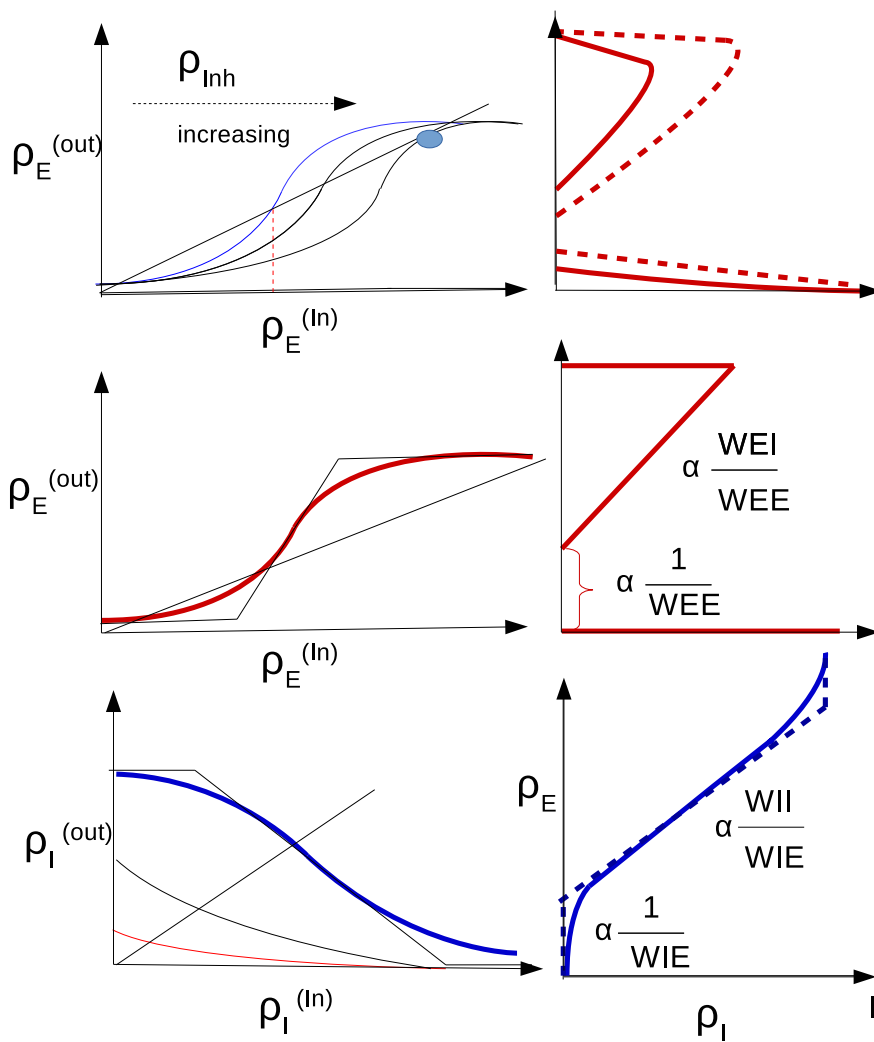


FIGURE 19. (Top-Left) Excitatory neuron output rate vs. excitatory input rate at three fixed values of inhibitory currents. (Middle-Left) Linearized excitatory gain function. (Bottom-Left) Inhibitory neuron output rate vs. inhibitory input at three different values of excitatory currents. (Right) Excitatory (Top and middle) and Inhibitory(bottom) null-clines of Eq.(3.3) and their linearization based on Eq.(3.4).

Where $k_{\alpha\beta}$ are the number of excitatory/inhibitory synapse to an excitatory/inhibitory neuron. In remaining of this work we assume external inhibitory currents to be zero which reflects the fact that inhibition is local in our model. We also take $\frac{k_{EI}}{k_{EE}} = \frac{k_{II}}{k_{IE}}$, which simplifies our analysis.

In the $\rho_{inh} - \rho_{exc}$ plane the slope and the y-intercept of two lines in the equation (3.4) determine the intersection of the two nonlinear nullclines and can be investigated to analyze approximate locations of bifurcation points of equation (3.3). We choose $\langle W_{EE} \rangle$ and $\rho_{Ext} = \lambda_{EE}$ as control parameters of our model. Therefore, we first discuss how their change would affect nullclines of equation (3.3). Increasing ρ_{Ext} moves the Sigmoid graph in Fig.19(TL) upwards causing low and middle fixed points to move towards each other. For a sufficiently high value of excitatory rate, these fixed points will disappear by a saddle-node bifurcation. In the excitatory nullcline graph (Fig.19-TR), increasing ρ_{Ext} leads to a shift of the graph to the right. Increasing W_{EE} will both reduce the y-intercept of excitatory nullcline and the slope of the linear section as it is shown in Fig.19(TR). Nullcline for inhibitory rate equation stays intact by change of control parameters.

Intersections of the inhibitory and excitatory nullclines are solutions to the set of rate equations (3.2). Based on the number of fixed points and their stability, system can show bi-stability of quiescent and high firing, oscillatory dynamics, avalanches, high synchronized activity, and quiescent state. Investigating the linearized section of the graphs can help us to identify different regimes of activity. The slope and y-intercept of the linear sections of nullclines can be compared for this purpose. Based on Poisson neuron approximation there exist a point in the control parameter space at which the y-intercept and slope of two nullclines are equal. This is the solution to the following linear constraints:

$$s_{exc} := \frac{W_{EI}k_{EI}}{W_{EE}k_{EE}} = \frac{W_{II}k_{II}}{W_{IE}k_{IE}} := s_{inh} \quad (3.5-a)$$

$$y_{exc} := \frac{d - \rho_{Ext}}{W_{EE}k_{EE}} = \frac{d - \lambda_{IE}}{W_{IE}k_{IE}} := y_{inh} \quad (3.5-b)$$

where d is a constant equal to $\frac{g_{leak}(V_{rest} - V_{th})}{\tau * g_{exc}^0 * (V_{th} - V_{Rexc})}$.

Fig.20(TL) shows the case in which $W_{EE}W_{II} > W_{EI}W_{IE}$ and y-intercept of the excitatory nullcline is lower than the inhibitory one. This occurs in the regime of a low to moderate imbalance of the excitatory and the inhibitory external input and high excitatory synaptic weight. In this case, there exist bistability of the quiescent and the high firing fixed point which are separated by a saddle. Increasing external excitatory input, the excitatory nullcline would be shifted to the right and the middle saddle and quiescent node would disappear by the Saddle-node bifurcation and only the

high firing synchronous state would remain(Fig.20(TR)). Increasing W_{EE} would also have the same qualitative effect. However, decreasing external input or W_{EE} drives the system to a quiescent state through different sets of bifurcations based on the initial state of the system and in general of other parameters of the model. This intermediate transition state involves the appearance of a fixed point in the linear section.

When $s_{exc} > s_{inh}$ while $y_{exc} < y_{inh}$, there is a fixed point in the linear section as depicted in Fig.20(BL). We will discuss the stability of the fixed point on the linear segment in the following sections. By increasing external input, the quiescent fixed point and the low saddle moves closer to each other while the fixed point on the linear section ascends to higher values of the rates. After Saddle-node bifurcation at the low rate, only the fixed point on the linear section survives as shown in Fig.20(BR). These two arrangements in which the fixed points are close to low firing regimes are of importance for us because of the avalanche dynamics that appear near this region. The intersection point of nullclines in the semilinear regime can be approximated by the intersection point of the linearized nullclines which is:

$$\rho_E^c = \frac{\tau g_0 (V_E^R - V_{th})(c_{II}\rho_{Ext} - c_{EI}\lambda_{EI}) + g_L (V_L - V_{th})(c_{II} - c_{EI})}{\tau (c_{IE}c_{EI} - c_{EE}c_{II})} \quad (3.6)$$

$$\rho_I^c = -\frac{\tau g_0 (V_E^R - V_{th})(c_{IE}\rho_{Ext} - c_{EE}\lambda_{EI}) + g_L (V_L - V_{th})(c_{IE} - c_{EE})}{\tau (c_{IE}c_{EI} - c_{EE}c_{II})}$$

where $c_{xy} = k_{xy}w_{xy}g_y(V_y^R - V_{th})$.

As discussed previously, in the intermediate range of the parameters, the high fixed point might become unstable through either Andronov-Hopf or Saddle-node bifurcations. Figures (21 and 22) show the nullclines graphs and the population activity when the high fixed point loses stability by Hopf bifurcation. Fig.21(TL) shows nullclines of a system that has stable high and quiescent fixed points with a saddle-node at low rates. By decreasing W_{EE} , s_{exc} is approaching s_{inh} while sufficient external input guarantees that $y_{exc} < y_{inh}$ during this parameter change. In this particular setup, the inhibitory nullcline is semi-linear and it is straightforward to speculate that the high fixed point goes through Hopf bifurcation when the return point of excitatory nullcline touches the inhibitory nullcline which takes place at some value $w_{EE}^* \in [0.55, 0.75]$. Decreasing w_{EE} further, high saddle fixed point descends through linear segment and gets closer to the lower saddle point, the limit cycle becomes unstable by the saddle separatrix loop bifurcation preceding by the saddle-node annihilation of low and high saddles and the system will end up in the quiescent state for low values of W_{EE} (Fig.21-Bottom). Population activity in these three regimes is shown in Fig.22. Neurons are firing synchronously with high rates in three different sub-populations in the first case. The high oscillatory activity appears in the second regime where the unstable saddle, which is encircled by a stable

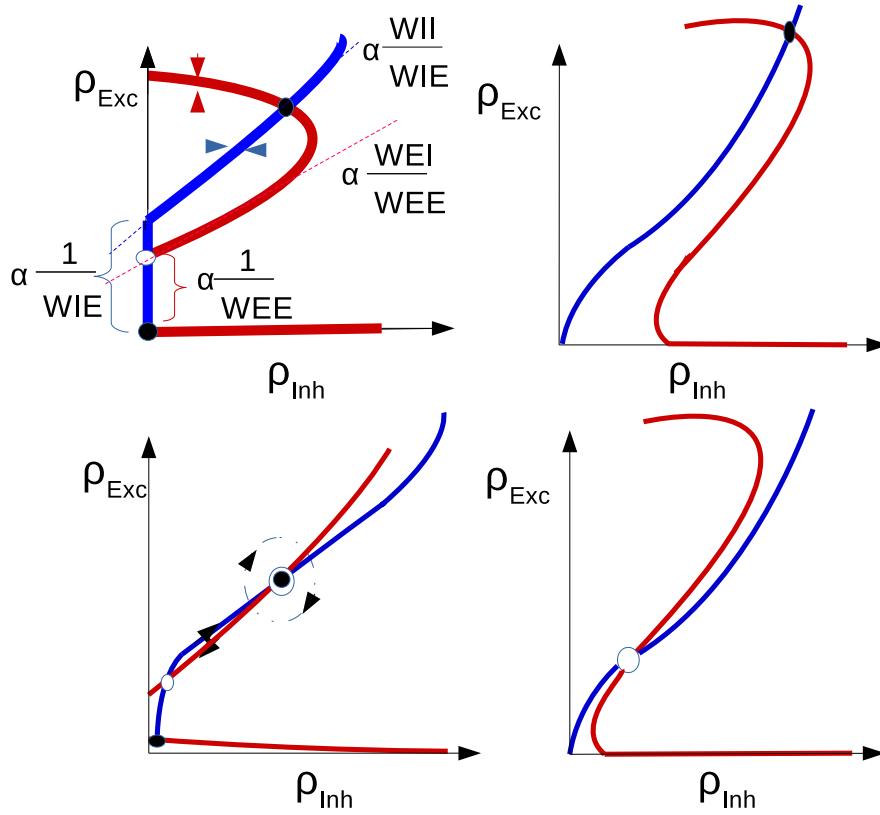


FIGURE 20. From Top-Left to Bottom-Right: Nullclines diagrams corresponding to the regimes of bistability, the high synchronized firing, the avalanches and the oscillatory dynamics. Red curves are the excitatory nullclines (Eq.3.2a) and blue curves are the inhibitory nullclines (Eq.3.2b).

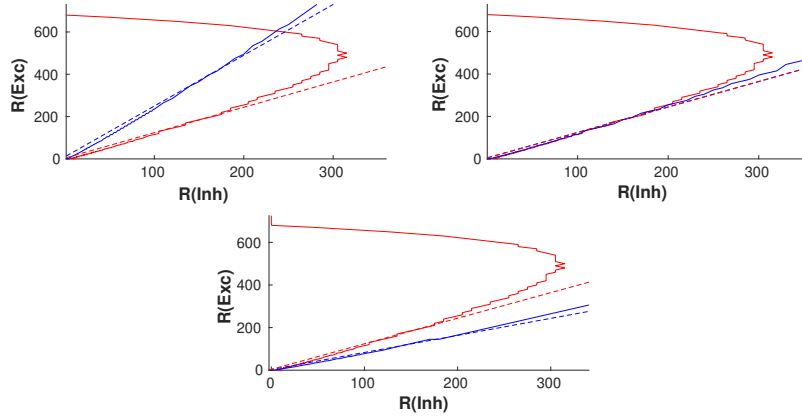


FIGURE 21. The nullclines for the excitatory and the inhibitory neuron populations and their corresponding linear approximations of Eq.(3.4-a) and (3.4-b). Values of parameters are $w_{EE} = [0.75$ (Top-Left), 0.55 (Top-Right), 0.4 (Bottom)], $w_{EI} = 2$, $w_{II} = 1.5$, $w_{IE} = 0.6$.

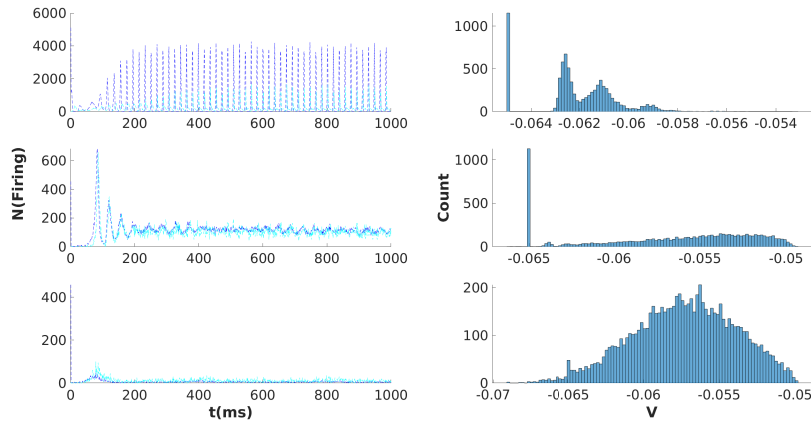


FIGURE 22. Simulation of populations of $N_E = 10000$ excitatory and $N_I = 0.25N_E$ neurons connected by the average synaptic weights same as those in Fig.21. (Left) The number of active excitatory neurons(dark blue) and active inhibitory neurons(light blue) in each time slot of (0.1ms) for three different values of w_{EE} .(Right) The stationary membrane potential distribution is shown correspondingly. In the Asynchronous state, the distribution has higher variance.

limit cycle, lies close to the high activity region. Membrane potential distribution, in this case, has a higher variance, and neurons fire asynchronously.

On the other hand, Fig.23 shows the case in which a high fixed point loses stability through colliding with the saddle that ascends along the linear

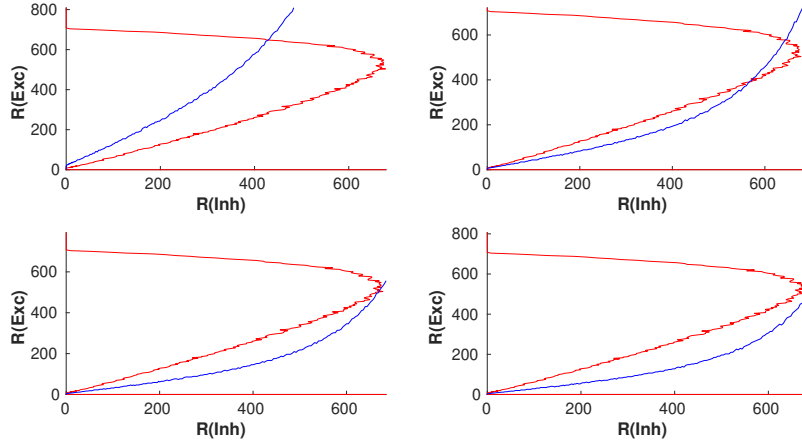


FIGURE 23. Nullclines for the excitatory (red curve) and the inhibitory (blue curve) population rates. The parameters used are $w_{EE} = 0.6, w_{EI} = 1.2, w_{II} = 0.6, w_{IE} = 0.6$ and $w_{EE} = [0.8, 0.6, 0.4, 0.2]$. decreasing w_{EE} changes the intersections of two curves. (The lowest value of w_{EE} corresponds to the top-left plot and the highest is for the bottom-right plot).

section. This situation occurs in a lower level of the external input, in which decreasing W_{EE} makes y_{exc} to pass above y_{inh} before the slopes become equal. In this case, the high activity fixed point is annihilated by the saddle fixed point.

In addition to oscillatory activity in the middle range of rates, the EI-population can exhibit non-oscillating asynchronous activity which corresponds to a stable fixed point in the linear regime. Fig.24 is the simulation result of excitatory population rate similar to the setup of the Fig.22 with higher W_{II} , which, as we will see later, makes the fixed point on linear section stable.

Fig.25 shows the transition from low firing asynchronous state to high firing synchronous state by decreasing W_{IE} with $W_{EE} = 0.5$.

3.2. Logistic Function Approximation of Gain Functions. In this section, we approximate gain functions in equation (3.3) by logistic function to analyze bifurcations diagram and approximate locations of bifurcation points. For this purpose, we consider the following form of gain

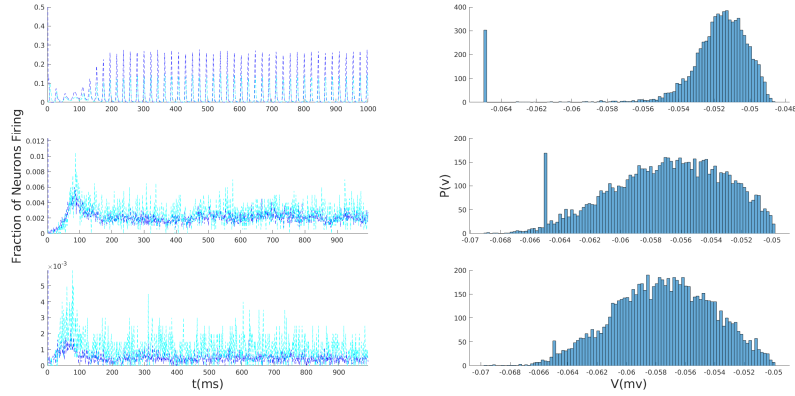


FIGURE 24. Simulation results of the network with same parameters as in Fig.22 except for new value of $w_{II} = 2.4$. EI population shows asynchronous firing in medium range of W_{EE} . This suggest that there is a stable fixed point at intersection of linear segments of excitatory and inhibitory nullclines.

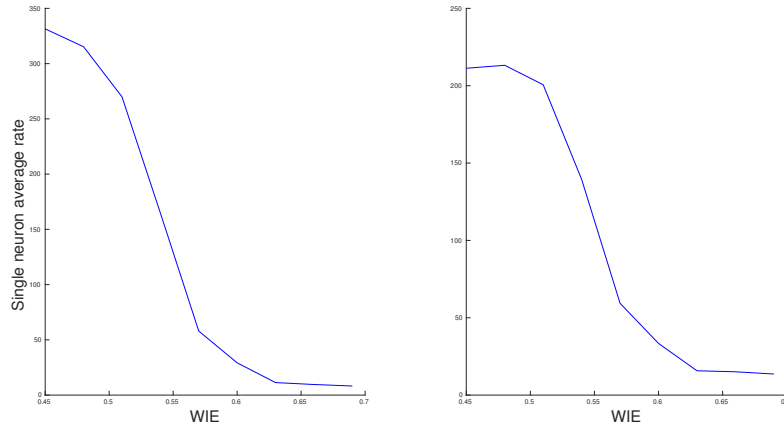


FIGURE 25. Average firing rate of an excitatory (Left) and an inhibitory neuron(Right) in an EI interconnected population with $w_{EE} = 0.5$, $w_{EI} = 2$, $w_{II} = 2.4$.

function for both excitatory and inhibitory populations :

$$g^x(\rho_{Inh}, y_x) = \frac{\rho_{max}}{1 + \alpha(\rho_{Inh})e^{-ky_x}} - z_0 \quad (3.7)$$

$$y_x = g_{syn}\tau w_{xI}\rho_{Inh}(V_{Rinh} - V_{th})$$

$$+ g_{syn}\tau(w_{xE}\rho_{exc} + \rho_{Ext}^x)(V_{Rexc} - V_{th}) + g_L(V_{Leak} - V_{th})$$

$$z_0 = \frac{\rho_{max}}{1 + \alpha(0)e^{-kg_L(V_{Leak} - V_{th})}}$$

Here, x stands for either excitatory(E) or inhibitory(I) gain functions, which have the same form but different input arguments. ρ_{Ext}^x is the external excitatory input to the population x . In the following, we fix the excitatory external input to the inhibitory population at a fixed value and set the external excitatory input $R_E := \rho_{Ext}^E$ as one of the control parameters besides W_{EE} . As in the previous section, we assume inhibitory synapses to be local and set the external inhibitory currents to zero. Bifurcation analysis for the EI population with sigmoidal gain functions has been done in Borisyyuk et al. [115]. Here, we take slightly different gain functions and different sets of control parameters.

At $y_x = 0$, the balanced input sets the membrane potential at the threshold value and output rate would be approximately $g_{th} = \frac{\rho_{max}}{1 + \alpha(\rho_{inh})}$. Dependence of the output rate on inhibitory input, when balanced condition at threshold holds, is represented by the function α . At $y = 0$, the output rate is proportional to the standard deviation in the input and it can be written as a function of inhibitory input rate as(see Fig.26):

$$g_{th} = b_0 + b_1\sqrt{\rho_{inh}}$$

which fixes function $\alpha(\rho_{inh})$.

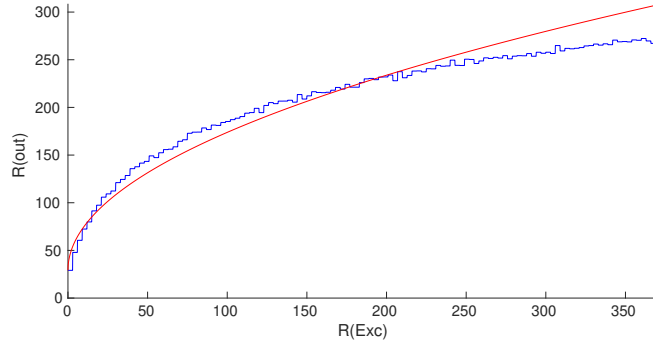


FIGURE 26. Output rate as a function of the input inhibitory rate, when the excitatory rate is selected in a way that the average membrane potential of the neuron is V_{th} . The neuron is operating near a saddle-node bifurcation point at which $F(I_{syn}) = k\sqrt{I_{syn} - I^*}$.

At the equilibrium, population rates satisfy the following equations:

$$\begin{aligned} \rho_I &= g^I(\rho_I, c_{ie}\rho_E + c_{ii}\rho_I + d\rho_{Ext}^I) - z_0 \\ \rho_E &= g^E(\rho_I, c_{ee}\rho_E + c_{ei}\rho_I + dR_E) - z_0 \end{aligned} \quad (3.8)$$

Where $c_{xy} = k_{xy}w_{xy}(V_{R_y} - V_{th})$ and $d = (V_{RExc} - V_{th})$. Same as before, we take w_{EE} and R_E as control parameters. Therefore, solution of the first equation is independent of the control parameters and gives a curve

in the $\rho_{Inh} - \rho_{Exc}$ plane. Taking into account that inverse of $g(\rho_{Inh}, y)$ is $g^{-1}(\rho_{Inh}, z) = \frac{1}{k}(\log(\frac{z}{\rho_{max} - z}) + \log(\alpha))$, equation for the inhibitory nullcline can be written as :

$$\rho_E = \frac{1}{c_{ie}} \left(\frac{1}{k} \left[\log\left(\frac{(\rho_I + h_0)}{\rho_{max} - (\rho_I + h_0)}\right) + \log(\alpha) \right] - c_{ii}\rho_I - dR_E - g_L \right) \quad (3.9)$$

The term in the bracket accounts for non-linearity in low and high values of ρ_I . Derivative of this term w.r.t ρ_I is $\frac{\rho_{max}}{\rho_I(\rho_{max} - \rho_I)}$, which is very small in middle range of ρ_I at values close to $0.5\rho_{max}$. This is consistent with the fact that nullclines are approximately linear in the middle range of the rates. To analyze linear stability of the fixed points, let us write down derivatives of gain function in the following format:

$$\begin{aligned} \frac{\partial g^x}{\partial \rho_E} &= k c_{xe} g^x \left(1 - \frac{g^x}{\rho_{max}}\right) \\ \frac{\partial g^x}{\partial \rho_I} &= k c_{xi} g^x \left(1 - \frac{g^x}{\rho_{max}}\right) - \frac{1}{\alpha} g^x \left(1 - \frac{g^x}{\rho_{max}}\right) \frac{\partial \alpha}{\partial \rho_I} \end{aligned}$$

Here g^x stands for g^I or g^E . One can substitute $\rho_I + h_0$ and $\rho_E + h_0$ from equation(3.8) for g^I and g^E , respectively. Therefore, Jacobian matrix at the fixed point is of the following form :

$$J = \begin{pmatrix} -1 + c_{ee}\rho^E \left(1 - \frac{\rho_E}{\rho_{max}}\right) & c_{ei}\rho^E \left(1 - \frac{\rho_E}{\rho_{max}}\right) - \frac{1}{\alpha} \rho_E \left(1 - \frac{\rho_E}{\rho_{max}}\right) \frac{\partial \alpha}{\partial \rho_I} \\ c_{ie}\rho^I \left(1 - \frac{\rho_I}{\rho_{max}}\right) & -1 + c_{ii}\rho^I \left(1 - \frac{\rho_I}{\rho_{max}}\right) - \frac{1}{\alpha} \rho_I \left(1 - \frac{\rho_I}{\rho_{max}}\right) \frac{\partial \alpha}{\partial \rho_I} \end{pmatrix} \quad (3.10)$$

Hopf bifurcation occurs at fixed point solutions at which trace of the Jacobian(Eq.(3.10)) vanishes and its determinant is positive. On the other hand, at the saddle-node bifurcation points determinant vanishes. Fig.27 shows the arrangement of the excitatory and inhibitory nullclines at the Hopf and the saddle-node bifurcation points. We proceed to approximate local bifurcation lines in the parameter space.

Condition on zero trace, $Tr(J) = 0$, parameterized by the inhibitory nullcline curve(Eq.(3.9)) results in the value for W_{EE} at which Hopf bifurcation can occur. Ignoring terms related to α , which are relatively small, from equating the trace of the Jacobian to zero, we have:

$$w_{EE}^H = \frac{2 - c_{ii} * \rho_I \left(1 - \frac{\rho_I}{\rho_{max}}\right)}{c_{ee0}\rho_E \left(1 - \frac{\rho_E}{\rho_{max}}\right)}$$

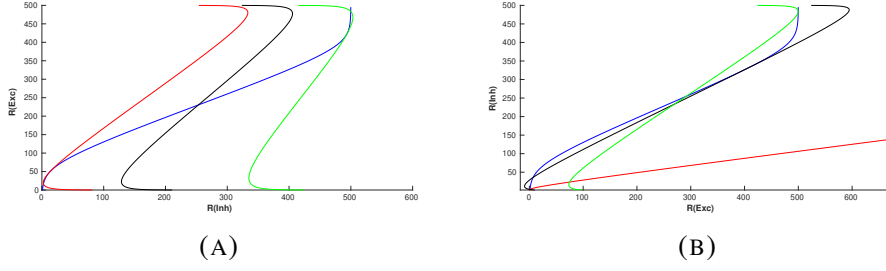


FIGURE 27. Inhibitory (blue) and Excitatory nullclines for three different sets of control parameters (W_{EE}, R_E) at the Hopf bifurcation (A) and the saddle-node bifurcation points (B). Parameters were chosen to illustrate positions of nullclines at the parameter values in which bifurcation happens in the lower nonlinear, the semi-linear, and the high nonlinear sections of the nullclines.

where $c_{ee0} := \frac{c_{EE}}{w_{EE}}$. For each (ρ_E, ρ_I) point on the inhibitory nullcline (Eq.(3.9)), the above equation gives a value of w_{EE} which sets the trace of Jacobian to zero at this point. The second equation in (3.8) which corresponds to the excitatory nullcline determines external excitatory input, R_E , parameterized by ρ_{Inh} . Next, we should check the condition on positivity of determinant to sketch the Hopf bifurcation line in the $w_{EE} - R_E$ plane. Neglecting non-linearities caused by α , determinant of the Jacobian conditioned on zero trace is :

$$\det(J)|_{Tr(J)=0} = -\left(1 - c_{ii}\rho_I\left(1 - \frac{\rho_I}{\rho_{max}}\right)\right)^2 - c_{ie}c_{ei}\rho_I\left(1 - \frac{\rho_I}{\rho_{max}}\right)\rho_E\left(1 - \frac{\rho_E}{\rho_{max}}\right)$$

At extremely low values of the rates (near zero), the determinant is negative because of the -1 in the above formula. Conditioned on a sufficient amount of inhibitory feedback's strength, which is proportional to $|c_{ie}c_{ei}|$, determinant becomes positive at some point by increasing rates and the low fixed point losses stability through Hopf bifurcation. The point that both determinant and trace of J are zero, is called Bogdanov-Takens(BT) bifurcation point.

Inserting $\rho_E\left(1 - \frac{\rho_E}{\rho_{max}}\right)$ from $\det(J)|_{Tr(J)=0} = 0$ into the denominator of the formula for w_{EE}^H and introducing parameter $\gamma = \rho_I\left(1 - \frac{\rho_I}{\rho_{max}}\right)$, the BT point in the low rate regime is located at the following strength of W_{EE} :

$$w_{EE}^{BT} = \frac{\gamma c_{ie}c_{ei}(2 - c_{ii} * \gamma)}{(1 - c_{ii}\gamma)^2}$$

At moderate value of $c_{ii}\gamma$:

$$w_{EE}^{BT} \approx \frac{w_{ie}w_{ei}}{w_{ii}}. \quad (3.11)$$

On the semi-linear part of the inhibitory nullcline, we have approximate relation between rates in the form of $\frac{\rho_I}{\rho_E} \approx \frac{w_{IE}}{w_{II}}$. Determinant on the line of zero trace when $\rho_E = \frac{w_{II}}{w_{IE}} := \beta\rho_I$ is :

$$\det(J)|_{Tr(J)=0} = -1 + 2c_{II}\gamma + (c_{ii}^2 - \beta c_{ie}c_{ei})\gamma^2$$

Function $\gamma(\rho_I)$ has a maximum at $\frac{\rho_{max}}{2}$. With this in mind, condition for positive determinant at potential Hopf Bifurcation fixed point in lower rates of linear regime will be :

$$\det(J)|_{Tr(J)=0}^L \approx -c_{ii}^2\rho_I^2 - c_{ie}c_{ei}\rho_E\rho_I = |c_{ii}|\rho_I^2(|c_{ei}| - |c_{ii}|) > 0$$

Therefore, if $|c_{ei}| > |c_{ii}|$, Hopf bifurcation line continues to survive on the linear regime. On this line, $w_{ee}^{Hopf} \approx \frac{2 - c_{ii}\gamma}{c_{ee0}\beta\gamma}$, which has negative derivative $\frac{-2}{\beta\gamma^2}$. Thus, Hopf bifurcation on the linear regime occurs at lower values of w_{EE} compared to w_{EE}^{BT} . On the other hand, R_E should increase to satisfy the fixed point condition of equation (3.8) for the excitatory rate. Altogether, in the $(w_{EE} - R_E)$ plane, Hopf bifurcation line extends to lower w_{EE} and higher R_E from the low BT point to the high BT point.

Ascending on inhibitory nullcline, we would reach the nonlinear high branch of the curve, where linear relation between rates no longer holds and second derivative of $\rho_E^*(\rho_I)$ will increase. Besides, $\gamma(\rho_{inh})$ decreases towards zero. Taking into account both of these facts, on high branch $\det(J)|_{Tr(J)=0}^L$ decreases and passes through zero at another Bogdanov Takens point at high values of rates. If inhibitory feedback is not strong enough conditions for Hopf bifurcation are not satisfied.

To sketch the saddle-node bifurcation line, we should look at solutions to $\det(J) = 0$. Inserting $\rho_E(\rho_I)$ from equation (3.9) to $\det(J)$, for each point on the inhibitory nullcline, there exist a w_{EE} which is the solution to $\det(J) = 0$. The only condition to check is $w_{EE} > 0$. Again the condition on the excitatory nullcline to intersect the inhibitory one at the fixed point determines R_E . Alongside the semi-linear section of the nullcline, the condition $\det(J) = 0$ translates to the alignment of the slopes of linearized nullclines. Therefore, along this section w_{EE} varies very little.

Fig.28 shows Hopf and Saddle-Node bifurcation lines with parameters written in the caption. As can be seen, there exists two Bogdanov -Takens bifurcation points at low and high values of the external input corresponding to the intersection of the nullclines in the low and the high firing rate regimes.

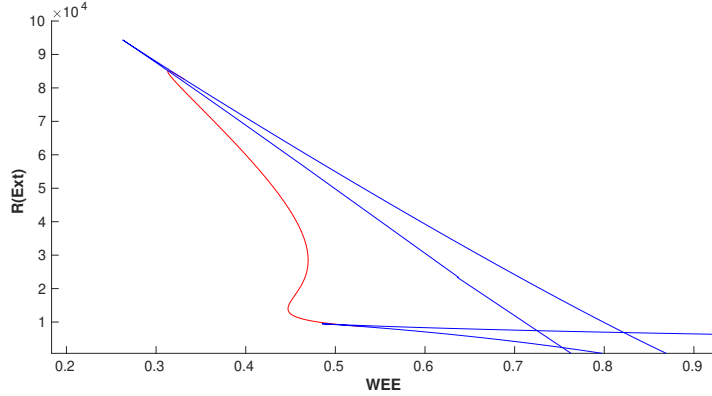


FIGURE 28. Local Bifurcation diagram in the control parameter plane (W_{EE}, ρ_{Ext}). Red curve is the Hopf bifurcation line and the blue curves are Saddle-node bifurcation lines. Free parameters of the model $\rho_{Ext}^{Inh} = 300Hz$, $W_{II} = 1$, $W_{EI} = 1.8$ and $W_{IE} = 0.6$.

Fig.29 is the bifurcation diagram at the low rates. Different regimes of the phase space corresponding to different numbers and/or types of fixed points have been labeled. The system has a minimum of one to a maximum of five fixed points. Region (1) in the low values of W_{EE} and the external input strength is the quiescent state with only one stable fixed point solution. In region (2), there is only an unstable fixed point surrounded by a stable limit cycle corresponding to the intersection of the nullclines in the semi-linear sections. In regions (3) and (4) near the BT point, two other fixed points exist in the low firing rates. The type of solution in these regions will be discussed in section (3.3). Region (5) corresponds to the case in which there exist 5 intersection points on the nullcline map and the bi-stability of the quiescent and high state which survives after the annihilation of unstable nodes on the middle section of nullcline to the region (6). Finally, in region (7), at a high level of the external input and the synaptic weight, the only existing fixed point is the high firing one.

Dashed lines in this figure are the constraints of equations (3.5-a) and (3.5-b) corresponding to equal slope and y-intercept of the linearized nullclines. The vertical line is the value of W_{EE}^* that matches the slopes, for $W_{EE} < W_{EE}^*$ the inhibitory feedback is getting stronger. The oblique line shows values of R_E for each W_{EE} that equalize y-intercepts of linearized nullclines. In the region below this line $y_{inh} < y_{exc}$ and vice versa.

3.3. Dynamics Near the BT Bifurcation Point. Exact location of the BT points in the parameter space ($c_{ee}^{BT}, R_E^{BT}, \rho_E^{BT}, \rho_I^{BT}$) are the solutions to $\det(J) = Tr(J) = 0$ and $g_E(i_E) = g_I(i_I) = 0$.

Fig.30 shows nullcline arrangements near the low BT point and the global saddle separatrix loop bifurcation line which annihilates the limit cycle solution of the region (3), shown in the same figure.

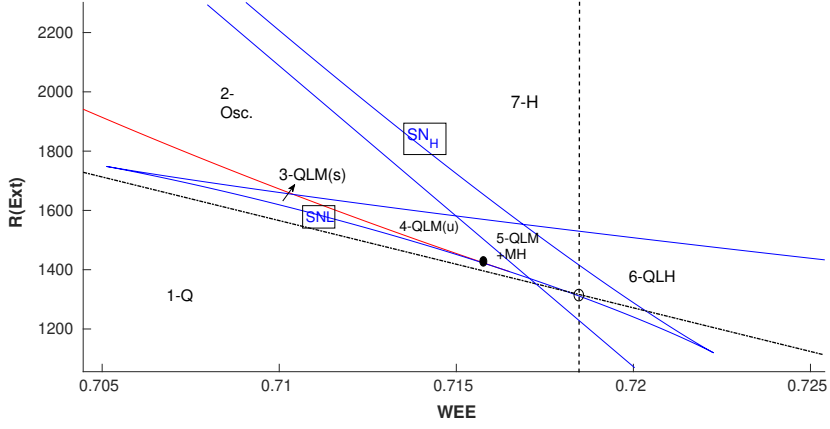


FIGURE 29. Zoom in on the local bifurcation diagram at low firing rates and the corresponding regimes of the phase space with different numbers of fixed points. The dashed line is the condition on the equal slope of linearized nullclines and the semi-dashed line is the condition on equal y-intercepts. BT point (black dot) is close to the intersection of these lines. In the labeling of regions, (Q) denotes quiescent state fixed point, (L) is the fixed point in low firing rate, (M) is the fixed point in linear section, and (H) is the high firing fixed point.

In the previous section, we showed that the low BT point is located close to the matching condition for y-intercept and slopes of linearized nullclines, which are rewritten below:

$$c_{ee}^* = \frac{c_{ie}c_{ei}}{c_{ii}}$$

$$R_E^* = \frac{c_{ee}^*}{c_{ie}}(\rho_{Ext}^I - d) + d$$

Where d is a constant defined in equation (3.5). The condition on zero trace at low values of rates leads to the approximate relation between the inhibitory and excitatory rates at the BT point in the Logistic function approximation of rates:

$$\frac{\rho_E^{BT}}{\rho_I^{BT}} \approx -\frac{c_{ii}}{c_{ee}} \quad (3.12)$$

Altogether, at the BT point the linearized matrix would be of the following form :

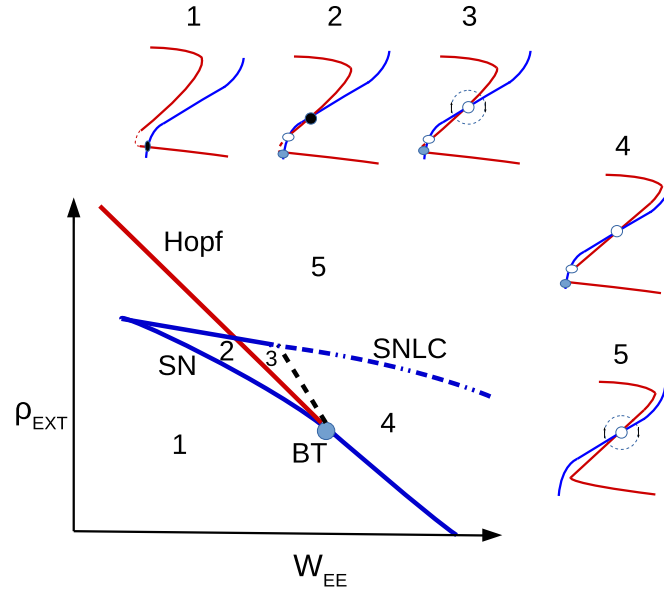


FIGURE 30. Nullclines' arrangements near the BT point. Black dashed line is saddle-separatrix loop bifurcation and the blue dotted-dashed is saddle-node on limit cycle(SNLC) bifurcation line.

$$J_{BT} = \begin{pmatrix} a & -b \\ \frac{a^2}{b} & -a \end{pmatrix} \quad (3.13)$$

where $\frac{b}{a} = \frac{c_{ei}}{c_{ee}} = \frac{c_{ii}}{c_{ie}}$.

At the BT point, Jacobian have a double zero eigenvalue and with proper coordinate transformation, it can be written in the following form:

$$J = \begin{pmatrix} 0 & 1 \\ 0 & 0 \end{pmatrix}$$

To write down the dynamic in the normal form in the vicinity of BT bifurcation point, consider the system:

$$\dot{x} = f(x, \mu) = Ax + F(x), x, \mu \in R^2$$

Assume at $\mu = 0$ system has a fixed point at x_0 and its Jacobian at this point has zero eigenvalue of multiplicity two. AT the BT point, there exist two generalized eigenvectors q_0 and q_1 such that:

$$Aq_0 = 0, Aq_1 = q_0$$

Also for A^T , we select vectors $p_{0,1}$ such that:

$$A^T p_1 = 0, A^T p_0 = p_1$$

which satisfy following normalizations:

$$\langle p_0, q_0 \rangle = \langle p_1, q_1 \rangle = 1, \langle p_0, q_1 \rangle = \langle p_1, q_0 \rangle = 0$$

By a linear change of coordinates with the transformation matrix $T = (q_0, q_1)$, i.e $x = Ty$, our system can be written as :

$$\begin{pmatrix} \dot{x}_1 \\ \dot{x}_2 \end{pmatrix} = \begin{pmatrix} 0 & 1 \\ 0 & 0 \end{pmatrix} \begin{pmatrix} x_1 \\ x_2 \end{pmatrix} + \begin{pmatrix} f(x_1, x_2) \\ g(x_1, x_2) \end{pmatrix} \quad (3.14)$$

By Taylor expansion of the nonlinear part as $\begin{pmatrix} f(x_1, x_2) \\ g(x_1, x_2) \end{pmatrix} = \begin{pmatrix} \sum_{m+n \geq 2} a_{mn} x_1^m x_2^n \\ \sum_{m+n \geq 2} b_{mn} x_1^m x_2^n \end{pmatrix}$, the critical center manifold can be parameterized as $x = h(y_1, y_2) = y_1 q_0 + y_2 q_1 + \sum h_{mn} y_1^m y_2^n$. To obtain the normal form, we insert this ansatz in the dynamic equation (3.14) to arrive at:

$$\begin{aligned} \dot{y}_1 &= y_2 \\ \dot{y}_2 &= \epsilon_1 + \epsilon_2 y_2 + a_2 y_1^2 + b_2 y_1 y_2 + O(\|y_1 y_2\|^3) \end{aligned} \quad (3.15)$$

Here, $\epsilon_{1,2}(\mu)$ are transformed bifurcation parameters, $a_2 = g_{xx}/2$ and $b_2 = g_{xy} + f_{xx}$. Fixed points of the normal form of equation (3.15) are $y_0^\pm = (\pm \sqrt{\frac{-\epsilon_1}{a_2}}, 0)$. Taking $a_2 > 0$ for the moment, when $\epsilon_1 < 0$, there exist two fixed points. Jacobian at these points are of the following form :

$$\begin{pmatrix} 0 & 1 \\ \pm 2\sqrt{\frac{-\epsilon_1}{a_2}} & \epsilon_2 \pm b_2\sqrt{\frac{-\epsilon_1}{a_2}} \end{pmatrix}$$

By computing the trace and the determinant of the Jacobian, we see that y_0^+ is a saddle when $\epsilon_1 < 0$ for all ϵ_2 , while y_0^- is a sink for $\epsilon_2 < b_2\sqrt{\frac{-\epsilon_1}{a_2}}$ and a source for $\epsilon_2 > b_2\sqrt{\frac{-\epsilon_1}{a_2}}$. When $b_2 > 0$, the line of $\epsilon_2 = b_2\sqrt{\frac{-\epsilon_1}{a_2}}$ is a sub-critical Hopf bifurcation line and when $b_2 < 0$ the same line is a supercritical Hopf bifurcation. A reverse scenario happens when $a_2 < 0$. To summarize, defining $\sigma = \text{sgn}(a_2 * b_2)$, if σ is negative then a stable limit cycle appears and the Hopf bifurcation is supercritical (Fig.31(right)), otherwise, if σ is positive, we have a sub-critical Hopf bifurcation (Fig.31(left)). As shown in Fig.31, near the BT point apart from the local bifurcations, i.e Hopf and saddle-node, there is a saddle-node separatrix loop bifurcation which annihilates stable or unstable limit cycle that are produced by supercritical or sub-critical Hopf bifurcations, respectively.

Linearization near the BT point can help us to identify dynamical regimes surrounding it without calculation of the σ parameter. Nullclines' map of

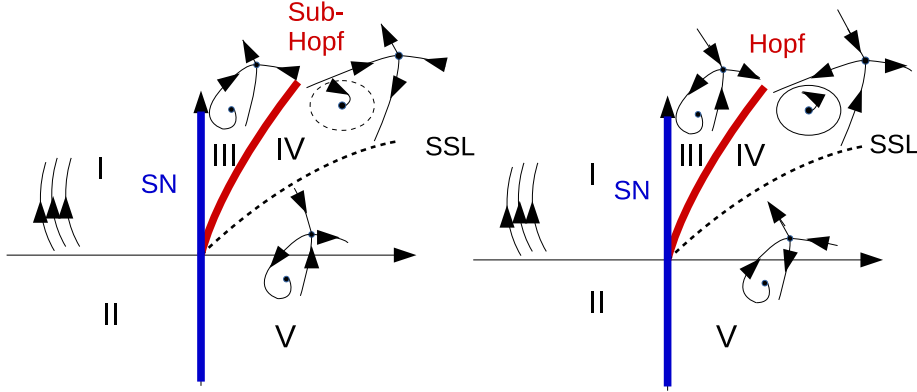


FIGURE 31. (Left) Dynamic flow near the high BT point. (Right) The same for the low BT point. Blue lines are saddle-node bifurcation, red lines are Hopf bifurcation, and dashed lines are saddle-node separatrix loop bifurcation.

regions (2) and (3) in Fig.30 shed light on the type of BT bifurcation. In the plot corresponding to the region (3), w_{EE} is higher which means the Jacobian at the fixed point has a lower determinant and a higher trace w.r.t the corresponding values in the region (2). Of the two fixed points in regions (2) and (3) at the semi-linear section, the one in the higher W_{EE} regime (region (3)) is the unstable point. Therefore, in our case near the low BT point, the phase space resembles the one in Fig.31(Right). Increasing W_{EE} from the region (2) will result in the loss of stability of the fixed point in the linear branch by the Hopf bifurcation as the value of the trace of the Jacobian at the fixed point becomes zero. However, as we increase w_{EE} the slope of the linearized approximation of nullclines which are tangent to the stable and the unstable manifolds of the saddle point that separate the quiescent fixed point and the limit cycle solution get closer to each other. At some point, these manifolds cross over and therefore, destroys the limit cycle solution through saddle-node separatrix loop bifurcation. This ends up in a source in the linear firing regime of the region (4) of Fig.30. The position of the Hopf bifurcation line and the saddle-node at the semilinear regime determines the region of oscillatory solution. The Limit cycle can be itself the only solution or it can coexist with another fixed point.

For our EI system, we can write down the normal form and analyze the type of the BT point from explicit linearization. For the case of J_{BT} in equation (3.13), generalized eigenvectors are $q_0 = (1 \ a/b)$ and $q_1 = (1 \ (a-1)/b)$. Therefore, new parameterized coordinates are $y_1 = E/b - a/b(E - I)$ and $y_2 = E - I$.

Using Logistic gain function second derivatives can be written as:

$$\begin{aligned} g_{EE} &\propto W_{IE}^2 g_I(1 - g_I)(1 - 2g_I) \\ g_{EI} &\propto -|W_{II}||W_{IE}|g_I(1 - g_I)(1 - 2g_I) \\ f_{EE} &\propto W_{EE}^2 f_E(1 - f_E)(1 - 2f_E) \end{aligned}$$

where $g_{EI} < 0$, $f_{EE} > 0$ and $g_{EE} > 0$. At the BT point, $|W_{II}|g_I(1 - g_I) = W_{EE}f_E(1 - f_E)$, therefore:

$$\text{sgn}(\sigma) := \text{sgn}(g_{EE} * (f_{EE} + g_{EI})) = \text{sgn}(W_{EE}(1 - 2f_E) - |W_{IE}(1 - 2g_I)|) < 0$$

which is satisfied in the case of adequately strong inhibitory feedback.

3.4. Avalanches in the Region Close to the BT Point. We assume that the external input to both excitatory and inhibitory neurons are dominated by the excitatory type and also connections among excitatory populations have a longer range. Therefore, the external excitatory input to the excitatory population is higher than to the inhibitory one. On the other hand, inhibitory connections are local and therefore, following the dynamics of the adjacent excitatory population. Strong local feedback provided by the inhibition prevent the excitatory network to be overloaded. However, it is very closely balanced to set the network near the threshold of activation so that system can respond efficiently to the external input. In the substrate regime of spontaneous activity, the EI population does show avalanche pattern dynamics and oscillatory behavior. Synchronization of oscillations and the scale-free avalanche dynamics are characteristic behaviors experimentally validated. In the following, we will show that close to the BT point at a low firing rate regime, we can observe both phenomena.

In the parameter space enclosed by the Hopf and the saddle-node bifurcation lines, i.e. region (4-QLM(u)) in Fig.29, there exist regions with both oscillatory and medium-range Poisson firing states. Decreasing W_{EE} while changing ρ_{Ext}^E accordingly, so that the Low and medium fixed points move closer to the origin, the system moves towards the Bogdanov-Takens bifurcation point, where the saddle-node bifurcation and Hopf bifurcation lines intersect. In this regime, we see avalanche dynamics in our population. Close to the BT point, the basin of attraction of the quiescent fixed point shrinks, and the noise level is high enough for escaping from it. This is in the adjacency of both the saddle-node bifurcation, which creates unstable low and weakly stable medium firing fixed point, and the Hopf bifurcation of the quiescent fixed point. This region corresponds to strong inhibitory feedback and a sufficient imbalance in the external excitatory input to the excitatory and inhibitory population. In the nullcline graph, this translates to the state where the y-intercept of the excitatory graph is lower than the y-intercept of the inhibitory graph and the slope of excitatory is larger than the slope of inhibitory one. Increasing W_{EE} causes the middle fixed point to move to the higher rates and to have a larger basin of attraction. On the other hand, the saddle and the quiescent fixed point move towards each

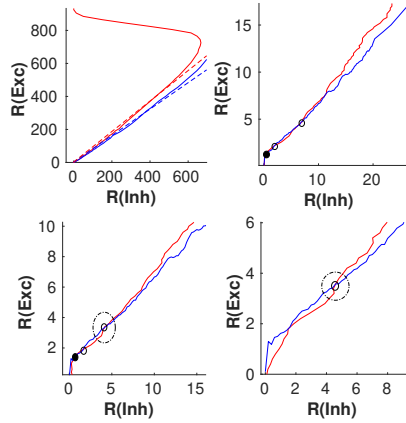


FIGURE 32. Nullclines configuration around avalanche dynamic region. Red curves are excitatory nullclines and blue curves are inhibitory nullclines.

other in the phase diagram and annihilate each other by the saddle-node bifurcation.

Fig.32 shows nullcline arrangements in the region that we observe avalanche patterns. The top-left diagram is the general position of nullclines indicating the fixed point in the linear regime. The other three diagrams correspond to the two distinct regimes near the BT point and the transition between these two. The top-right diagram belongs to the section to the right of the BT point (Fig.30) in which there exists a quiescent fixed point with a weakly unstable saddle in the linear section. Here, noise causes the system to escape from the basin of attraction of the fixed point which then relaxes toward the origin in the direction of the nullclines. As nullclines lie on top of each other decay time is large and the system shows high synchronous activity while returning to a quiescent state. An increase of external drive or decrease of W_{EE} leads to a saddle-node annihilation which leaves the system with a fixed point at the middle section. Fig.31 (Bottom-left) belongs to the state on the left side of the BT point in the vicinity of the Hopf bifurcation of the origin. In this case, there is a limit cycle around the saddle point in the linear branch. Similar to the previous case, adjacency of fixed point at the origin to the saddle shrinks the basin of attraction of the quiescent state. Therefore, noise can bring the system to the limit cycle which itself is sensitive to internal and external noise. Finally, Fig.31 (BR) shows how saddle-nodes of the last two diagrams are annihilated by the saddle-node on limit cycle and the saddle-node bifurcations, respectively. In these two cases, a limit cycle solution emerges. However, close to origin this limit cycle stays for a longer time in the lower section of very low firing because of the slow flow in this region. The outcome is again a quasi-periodic burst of avalanches followed by a quiescent state.

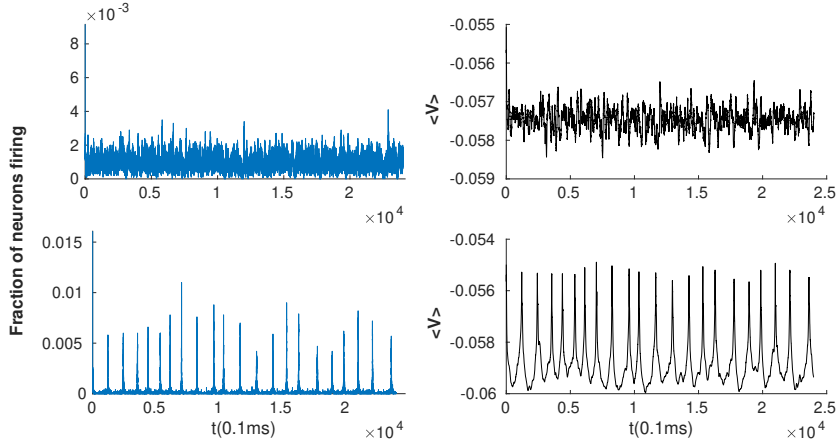


FIGURE 33. Avalanches close to the BT point. $W_{II} = W_{EI} = 2, W_{IE} = 0.75$, $\rho_{Ext}^{inh} = 150Hz$ in both panels. In the top figures $W_{EE} = 0.66$ and $\rho_{Ext}^{exc} = 209Hz$ and in lower panel $W_{EE} = 0.63$ and $\rho_{Ext}^{exc} = 225Hz$.

Fig.33 (Bottom) shows avalanche characteristics of the activity in the parameter regime on the left of BT point with the limit cycle solution very close to the origin(same as Fig.31(top-right)).In Fig.33 (Top), W_{EE} is higher and ρ_{Ext}^E is slightly lower than the previous case and the system is located in the region with a fixed point in low firing regime which is stable because of the high value of W_{II} . Fig.34 shows avalanche dynamics on the right side of the BT point. The bottom panel corresponds to the case in which the limit cycle is very close to the origin. In both sets of figures increasing W_{EE} moves the system out of the avalanche region with the difference that the fixed point at the linear section is stable in the first case and unstable in the second. Therefore, the nearby regime of the activity in the first case is a non-oscillatory inhomogeneous Poisson firing state while the corresponding regime near the second case is oscillatory.

3.5. Stability Analysis of the Fixed Points in the Linear Regime. As we have seen in the last section, close to the BT point there exist regions in which there is a low firing fixed point at the intersection of semi-linear sections of the nullclines. The stability of this fixed point is determined by the Jacobian matrix of the linearized system:

$$A = \begin{pmatrix} -1 + \frac{\partial f}{\partial E} & -\left| \frac{\partial f}{\partial I} \right| \\ \frac{\partial g}{\partial E} & -1 - \left| \frac{\partial g}{\partial I} \right| \end{pmatrix}$$

Linear segments would intersect if $y_{inh} < y_{exc}$ and $s_{exc} > s_{inh}$ or $y_{inh} > y_{exc}$ and $s_{exc} < s_{inh}$. When the slope and y-intercepts are equal, the Jacobian at the point of intersection is:

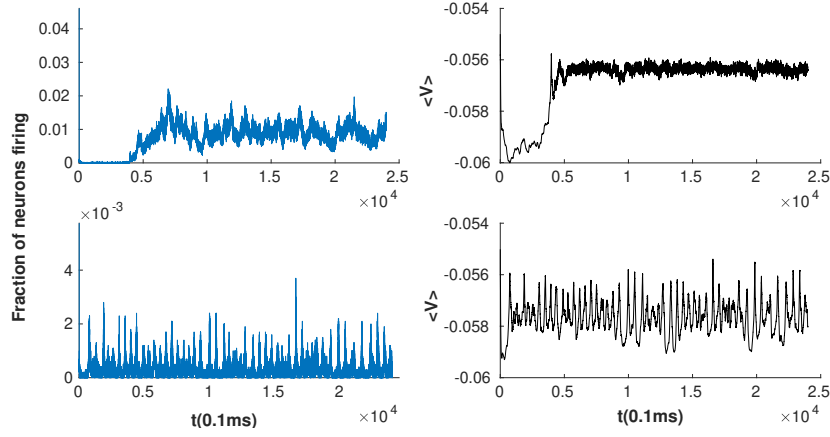


FIGURE 34. Same as Fig.33 but with new parameters: $W_{EI} = 2, W_{II} = 1.5, W_{IE} = 0.75, \rho_{Ext}^{inh} = 150\text{Hz}, \rho_{Ext}^{exc} = 280\text{Hz}, W_{EE} = 0.53$ (Top) and 0.48 (Bottom).

$$A = \begin{pmatrix} a - \mu & -(b - \frac{b}{a}\mu) \\ a & -b \end{pmatrix} \quad (3.16)$$

$$\text{with } \mu = a \frac{\rho_{Ext}^E - \rho_{Ext}^I}{c - \rho_{Ext}^I}.$$

$$a = \frac{\partial g}{\partial E} = \alpha' W_{IE} K_{IE} = \alpha W_{EE} k_{EE} - 1 + \mu$$

$$b = 1 + \left| \frac{\partial g}{\partial E} \right| = 1 + \beta' W_{II} K_{II} = \left(1 - \frac{\mu}{a}\right)^{-1} [\beta W_{EI} k_{EI}]$$

$$\alpha = g_{exc}^0 \tau_{exc} \frac{(V_{th} - V_{Rexc})}{\sqrt{2\pi\sigma_V^{Exc}}}$$

$$\alpha' = g_{exc}^0 \tau_{exc} \frac{(V_{th} - V_{Rexc})}{\sqrt{2\pi\sigma_V^{Inh}}}$$

$$\beta = g_{inh}^0 \tau_{inh} \frac{(V_{th} - V_{Rinh})}{\sqrt{2\pi\sigma_V^{Exc}}}$$

$$\beta' = g_{inh}^0 \tau_{inh} \frac{(V_{th} - V_{Rinh})}{\sqrt{2\pi\sigma_V^{Inh}}}$$

$$\alpha * \beta' = \beta * \alpha'$$

Because external excitatory input to the excitatory population is greater than the external input to the inhibitory population and inhibitory connections are assumed to be local, μ is slightly positive.

At $\mu = 0$, the eigenvalues of A are 0 and $a - b$ with corresponding eigenvectors, $u_1 = \left(\frac{b}{a}, 1\right)$ and $u_2 = (1, 1)$. By the coordinate transformation to

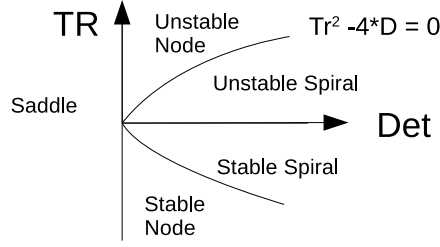


FIGURE 35. Stability of fixed points in the linear regime based on the values of trace and determinant of the Jacobian.

u_1 and u_2 coordinates, we can write down the dynamics in the decoupled system as follows:

$$u = \begin{pmatrix} \frac{b}{a} & 1 \\ 1 & 1 \end{pmatrix}^{-1} \begin{bmatrix} E \\ I \end{bmatrix} = \frac{a}{a-b} \begin{bmatrix} I - E \\ E - \frac{b}{a}I \end{bmatrix}$$

$$\dot{u} = \begin{pmatrix} 0 & 0 \\ 0 & a-b \end{pmatrix} u$$

With the transformed initial condition :

$$u_0 = \frac{a}{a-b} \begin{bmatrix} I_0 - E_0 \\ E_0 - \frac{b}{a}I_0 \end{bmatrix}$$

Which has the following solution in the u coordinates:

$$u(t) = \frac{a}{a-b} \begin{bmatrix} I_0 - E_0 \\ (E_0 - \frac{b}{a}I_0)e^{(a-b)t} \end{bmatrix} \quad (3.17)$$

Back into (E, I) coordinates:

$$\begin{bmatrix} E(t) \\ I(t) \end{bmatrix} = \frac{a}{a-b}(I_0 - E_0) \begin{bmatrix} \frac{b}{a} \\ 1 \end{bmatrix} + \frac{a}{a-b}(E_0 - \frac{b}{a}I_0)e^{(a-b)t} \begin{bmatrix} 1 \\ 1 \end{bmatrix} \quad (3.18)$$

So for this linear system, when $a - b < 0$, initial imbalance of the excitatory and inhibitory rates leads to a stationary relation of the form $E = \frac{b}{a}I$.

Now, consider the case in which linearized nullcline slopes are slightly different with the following Jacobian:

$$A = \begin{pmatrix} a - \mu & -(b + \epsilon) \\ a & -b \end{pmatrix}$$

Here, $TR = \lambda_1 + \lambda_2 = (a - b) - \mu$ and $det = \lambda_1\lambda_2 = a\epsilon + \mu b$. Based on the sign of determinant and trace of the Jacobian at the fixed point, stability type is determined (see Fig.35).

Under the condition that $b + \mu > a$ and $\epsilon > -\frac{b}{a}\mu$, both eigenvalues are negative : $\lambda_1 = \frac{b\mu - a\epsilon}{b - a}$ and $\lambda_2 = (a - b) + \frac{2a(\epsilon - \mu)}{a - b}$. We also have $|\lambda_1| \ll |\lambda_2|$ for small differences in the slopes.

Eigenvectors corresponding to these eigenvalues are :

$$\begin{aligned} u_1 &= \left(\frac{b}{a} + \lambda_1, 1 \right) \\ u_2 &= (1 + \lambda_2, 1) \end{aligned}$$

Therefore, the dynamics in the linear regime would be projected to the slow stable manifold u_1 . One can approximately write down the evolution of the rates as in equation (3.18).

$\epsilon > -\frac{b}{a}\mu$ corresponds to the case in which the slope of the excitatory nullcline is higher than the inhibitory nullcline (stronger inhibitory feedback $W_{EI}W_{IE} > W_{II}W_{EE}$) and y-intercept of the excitatory nullcline is slightly lower, i.e sufficient external input. Moreover, this is the case when W_{II} is high enough to guarantee $b > a$ condition. When all these requirements are met, the fixed point in the linear segment is stable and we observe an asynchronous low to medium firing state as in Fig.24 and Fig.33. Around this regime, an increase in W_{EE} will increase μ , and a change in ρ_{Ext}^E moves the fixed point along the linear section. The intersection in the linear regime transcends to higher rates by increasing W_{EE} . This decreases the determinant while the trace increases, which eventually destabilizes the fixed point. In the vicinity of the low BT point, based on the value of W_{II} , in the linear section either a weakly stable or a weakly unstable fixed point surrounded by a limit cycle appears. In both cases, the eigenvalue close to zero with the eigenvector u_1 governs the slow dynamics around this point.

Consider the case of imaginary eigenvalues of the Jacobian, $\lambda_{\pm} = \sigma \pm i\omega$ with eigenvectors $v_{\pm} = v_r \pm v_i$, which satisfy:

$$A[v_r v_i] = [v_r v_i] \begin{pmatrix} \sigma & \omega \\ -\omega & \sigma \end{pmatrix}$$

By defining the transformation matrix $T = [v_r v_i]$, the linearized matrix is $Q = T^{-1}AT = \begin{pmatrix} \sigma & \omega \\ -\omega & \sigma \end{pmatrix}$ and the solution of the linear system is of the form:

$$e^{At}x_0 = T e^{\sigma t} \begin{pmatrix} \cos(\omega t) & \sin(\omega t) \\ -\sin(\omega t) & \cos(\omega t) \end{pmatrix} T^{-1}x_0$$

By using the coordinate transformation $u = T^{-1}x$, we can write down the evolution of $\dot{u} = Qu$ with $u_0 = T^{-1}x_0$. Linearized dynamic predicts

damped oscillation of frequency $\omega = \sqrt{\det - \frac{Tr^2}{4}}$ when $\sigma < 0$. At the Hopf bifurcation point when $\sigma = 0$, frequency of oscillation will be $\omega = \sqrt{\det_H}$. At the nullcline intersections on the linear segments close to the Hopf bifurcation, oscillation frequency is close to the imaginary part of the eigenvalues, $\sqrt{\det - \frac{Tr^2}{4}}$.

Along the slow manifold, inhibitory and excitatory rates vary linearly as $I = \frac{a}{b}E \approx \frac{k_{ee}W_{ee}}{k_{ei}W_{ei}}$. This relation balances the average current to each population. Therefore, near the BT bifurcation point, dynamics of the slow field, $E - I$, can be written as :

$$\frac{d(E - I)}{dt} = \epsilon(E - I) + c(1 - \frac{a}{b})^{-1}(E - I)^2 + \frac{1}{\sqrt{N}}(1 - \frac{a}{b})^{\frac{1}{2}}(E + I)^{\frac{1}{2}}\eta(t) \quad (3.19)$$

In which, ϵ is close to zero, the first nonlinear term of Taylor expansion has been taken into account and $\eta(t)$ is a white noise added to the microscopic equation based on the Poisson firing assumption. This Langevin equation for the slow field matches the one for the directed percolation if we add a simple diffusive term to it. We will have a closer look at this equation in section (6).

3.6. Characteritics of Avalanches. For the values of W_{EE} near the BT point at the low firing rate, there exists a range of external input strength for which the firing pattern is quasi-periodic with the excitatory avalanches followed by the inhibitory ones. Mean escape time from the basin of attraction of the quiescent fixed point reduces when the external input increases, thus, the frequency of avalanches increases. Further increase of external input leads to the stability loss of the quiescent state and appearance of higher frequency oscillations in the medium range of rates.(see Fig.36)

In the avalanche regime, membrane potential shows sub-threshold oscillations as can be seen in Fig.33 and Fig.34. In the down phase of the cycle, neurons stay near resting potential while at the Up-state they reside closer to the threshold, but in a distance from it that permits high variability of firing. The membrane potential of a single neuron is depicted in Fig.37, which shows aperiodic firing and up-down states of membrane potential.

While avalanches occur quasiperiodically, in most of them only a fraction of neurons fire. As shown in (Fig.38 and Fig.39) neurons fire with the CV close to one in the lower W_{EE} regime, close to the BT point. Variability in the size of avalanches is another interesting factor to investigate. The size distribution of avalanches has a longer tail approaching the BT point. It follows power-law distribution of size of avalanche $P(S) \propto S^{-\tau}$ with slope $\tau = -1.5$ close to the BT point, see Fig.38 and Fig.39(Top-left). Further away from the critical point, avalanches have characteristic average size and

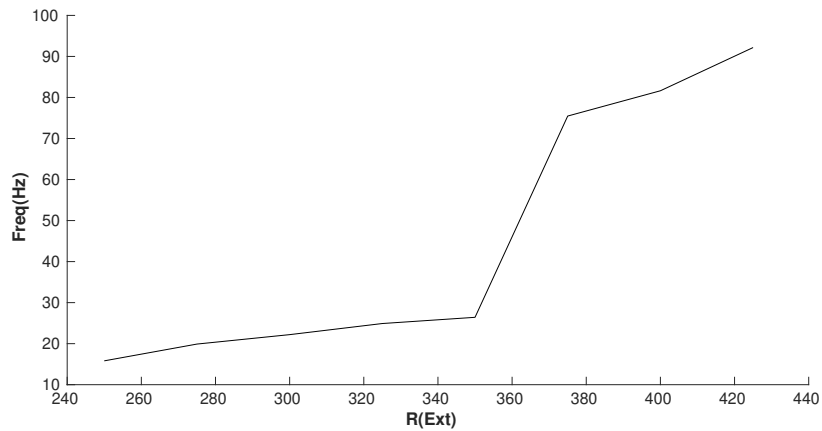


FIGURE 36. Frequency of avalanches and oscillatory activity increase by increase in the input strength. In the lower values of the excitatory external input, the limit cycle solution is very close to the origin and the system shows avalanches. By increasing the external drive, the limit cycle moves away from the origin (quiescent state) and becomes stable. Oscillations have a higher frequency at higher external input rates with semi-linear relations in both regions.

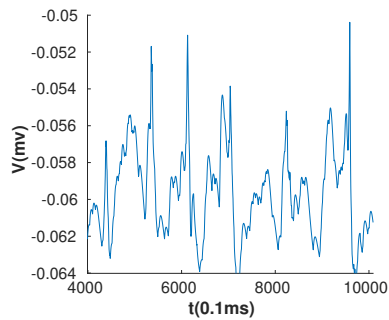


FIGURE 37. Membrane potential track of a single neuron during the avalanche dynamic of Fig.33.

their size probability density moves away from the power-law distribution. Furthermore, the probability distribution of duration of avalanches follows power-law with an exponent close to $\eta = -2$ near the BT point.

Branching ratio can be an indicator of the scale-free avalanche dynamics. When inhibition and excitation are balanced and the system resides near a quiescent state, the branching parameter stays close but below one which is an indicator of a stronger inhibitory feedback. As can be seen in

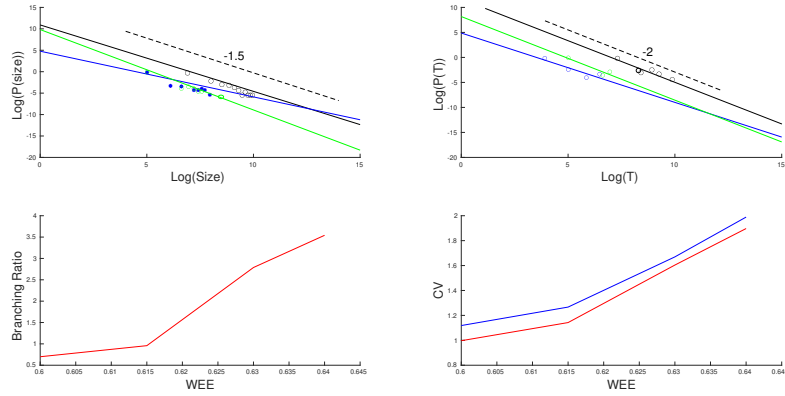


FIGURE 38. Same as Fig.33 with $W_{EI} = 2, W_{II} = 2, W_{IE} = 0.75, \rho_{Ext}^{inh} = 150\text{Hz}, \rho_{Ext}^{exc} = 230\text{Hz}$ with different value of $W_{EE} \in (0.6, 0.65)$. Top panels are the avalanches size and duration probability distributions in a log-log plot with the linear fit. Green line ($W_{EE} = 0.63$), black ($W_{EE} = 0.615$) and blue ($W_{EE} = 0.6$). (Bottom left) Branching ratio and (Bottom right) CV of firing time intervals of individual neurons. (red for excitatory neurons and blue for excitatory ones)

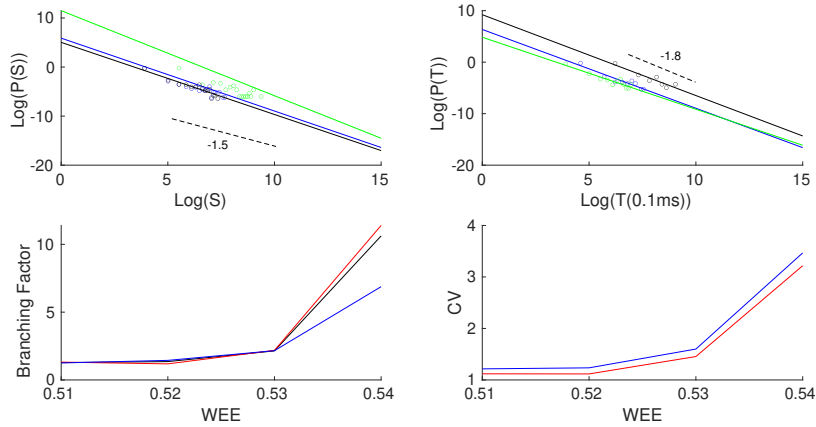


FIGURE 39. Characteristic of avalanches for the model with $W_{EI} = 2, W_{II} = 1.5, W_{IE} = 0.75, \rho_{Ext}^{inh} = 150\text{Hz}, \rho_{Ext}^{exc} = 280\text{Hz}$ and $W_{EE} \in (0.516, 0.54)$ as in Fig.34. Top panels are the avalanches size and duration distributions in a log-log plot with their corresponding least square error linear fit. Green line ($W_{EE} = 0.54$), black ($W_{EE} = 0.53$) and blue ($W_{EE} = 0.51$). (Bottom-Left) Branching ratio and (Bottom-Right) CV of interspike time intervals of individual neurons. (red for excitatory neurons and blue for excitatory ones).

Fig.38 and Fig.39, this value is lower in the parameter regime close to the BT point and becomes higher than one further away from it.

Branching ratio can be defined as the average number of postsynaptic neurons of a specific neuron that fire by receiving the synaptic current from that neuron. Here, we assume that by synchronous activation of n_E neurons, the postsynaptic neurons which are connected to these neurons will receive both excitation and inhibition currents caused by the synchronous input. Each neuron receives a fraction k_{EE} of excitatory and k_{EI} of inhibitory currents produced by active neurons in the populations. The average potential change among neurons will be:

$$\langle \Delta V \rangle = \langle k_{EE} n_E \rangle \frac{1}{C} g_0 w_{EE} \tau (V_{Rexc} - V_E) + \langle k_{EI} n_I \rangle \frac{1}{C} g_0 w_{EI} \tau (V_{Rinh} - V_E)$$

Close to the bifurcation point, there exists a tight dynamic balance between excitatory and inhibitory rates, following equation (3.18), which sets $\langle \Delta V \rangle = 0$. Based on the assumption that neurons fire with Poisson statistics, we can write down variance of the potential change in the postsynaptic neuron pool as:

$$\langle \Delta V^2 \rangle = \tau^2 g_0^2 (\langle k_{EE} n_E \rangle w_{EE}^2 (v_{Rexc} - V_{th})^2 + \langle k_{EI} n_I \rangle (w_{EI})^2 (v_{Rinh} - V_{th})^2). \quad (3.20)$$

On the other hand, the number of postsynaptic neurons that fire by receiving an increase in voltage of value ΔV would be :

$$\sigma = N_{Exc} \int_{V_{th} - \Delta V}^{V_{th}} P(V, t = \infty) \approx - \frac{N_{exc} \Delta V^2}{2} \frac{\partial p(v^E, t = \infty)}{\partial v} \Big|_{v^E = V_{th}} \quad (3.21)$$

From equation (2.16) for the stationary probability density we have :

$$\frac{\partial p(v^E, t = \infty)}{\partial v} \Big|_{v^E = V_{th}} = - \frac{2C^2 \rho_{exc}}{D_e (v_{Rexc} - V_{th})^2 + D_i (v_{Rinh} - V_{th})^2} \quad (3.22)$$

Inserting equation (3.22) in equation (3.21) and averaging σ over different realizations of the synchronous firing using equation (3.20) and dividing by $\langle n_E \rangle$ leads to :

$$\sigma^E \approx \frac{\tau^2 g_0^2 [w_{EE}^2 \rho_{exc}^{st} (v_{Rexc} - V_{th})^2 + \rho_{exc}^{st} \frac{\langle n_I \rangle}{\langle n_E \rangle} w_{EI}^2 (v_{Rinh} - V_{th})^2]}{D_e (v_{Rexc} - V_{th})^2 + D_i (v_{Rinh} - V_{th})^2} \quad (3.22)$$

Average number of active inhibitory and excitatory neurons $\langle n_I \rangle$ and $\langle n_E \rangle$, relates to stationary rates as $\frac{\langle n_I \rangle}{\langle n_E \rangle} = \frac{\rho_I}{\rho_E}$. Inserting this relation to equation (3.22), we find out that the branching ratio is close to one near the

BT point. Because of a slightly stronger inhibitory feedback, it would be slightly below one.

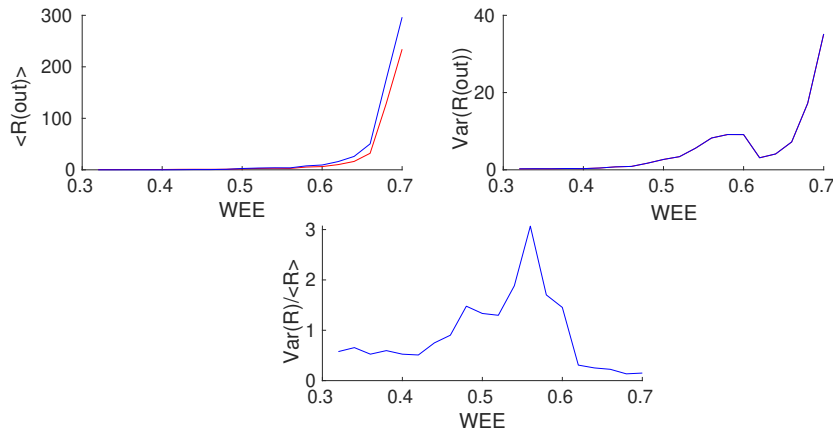


FIGURE 40. Stationary population rates (Blue for Inh. and Red for Exc.), variance and normalized variance for the EI population vs. W_{EE} at a fixed value of $\rho_{Ext} = 250Hz$. Other parameters were set to $W_{IE} = 0.75, \rho_{Inh} = 150Hz$, $W_{II} = W_{EI} = 2$.

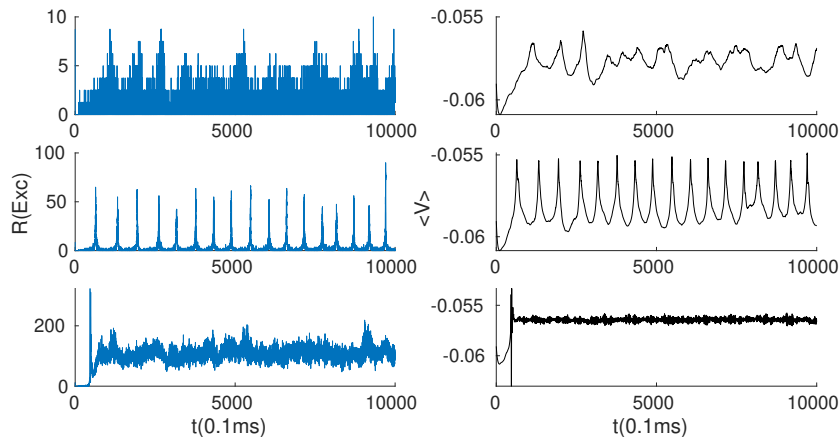


FIGURE 41. Excitatory population rate (Right plots) and average membrane potential (Left plots) corresponding to states slightly below the Hopf bifurcation point (Top), slightly above Hopf bifurcation point (Middle), and after saddle-node bifurcation point (Bottom) with the same parameters as in the Fig.40.

Excitatory neurons stay in a low firing regime with the average membrane potential close to the middle point of firing threshold and resting-state potentials, i.e. at $V \sim -57mv$. At this point, sufficient fraction of neurons

are close to the threshold, whose activation can cause a series of firing. On the other hand, inhibitory neurons, which have a lower stationary membrane potential because of lower external input, provide negative feedback with a delay that depends on the resting initial state and the strength of the connection between inhibitory and excitatory sub-networks. The dynamic balance of excitation and inhibition in the linear Up-state leads to the critical behavior. As the average currents to the cells are balanced far from the firing threshold, fluctuations in these currents have a larger effect and therefore, the size of events and their durations would have higher variabilities.

Moreover, let us consider the onset of avalanche dynamics in the EI population receiving external input with fixed rates by selecting W_{EE} as the only dynamic parameter, see Fig.40 . By increasing W_{EE} , a second-order phase transition happens at the Hopf bifurcation. Around this value, normalized variance of the population rate is maximized and oscillation appears in the system. In Fig.40, this happens at value $W_{EE} \approx 0.57$. Further increase of W_{EE} results in a saddle-node bifurcation which produces a stable high firing rate state at values around $W_{EE} \approx 0.67$. Fig.41 shows the firing state of the network in these three distinct regimes.

Although the activity is noise-driven, the state of the system depends on the synaptic weights, which determines the response to the external input. There must be a self-organizing mechanism, which in a wider range of the input strengths and initial configuration of synaptic weights tune the system close to the BT point.

4. Long Term and Short Term Synaptic Plasticity rules Tune the EI Population Close to the BT Bifurcation Point

4.1. Long Term Synaptic Plasticity by STDP Tunes Synaptic Weights Close to the Balanced State. A typical neuron in the cortex has $10^3 - 10^4$ synaptic connections with 80% of them of the excitatory type and 20% of the inhibitory type. On the other hand, even in the resting state, neurons on average have a non-zero firing rate with an average rate of $1Hz$ and their spike trains are very noisy with exponential inter-spike interval distribution indicating the spiking of individual neurons to be a Poisson point process. Yet another experimental fact about synaptic strength between neurons states that usually, 10 – 20 presynaptic synchronous spikes are enough to set a typical neuron to the firing threshold. If we take $\tau_m = 20ms$ as the membrane potential decay time constant, then during this time window a typical neuron receives 20 – 200 excitatory spikes, which are enough for the neuron to periodically spike with a very high rate. To avoid this, the inhibitory input in this time window should cancel the excitatory current to a large portion. Therefore, for the average currents to maintain the average membrane potential below the threshold in order to avoid a high firing state and produce high variability in the spike trains, inhibitory and excitatory currents should be balanced. Dynamical balance of excitation and inhibition ensures a low level of activity, i.e. asynchronous firing state. In the following, we present a synaptic plasticity rule which tunes the average synaptic weights to the balanced state. We will analyze and simulate a network in which neurons will adapt their connections according to the Synaptic Time-Dependent Plasticity (STDP) paradigm, which is at the foundation of temporal coding [116]. We derive an equation for the evolution of the average and the variance of weights between excitatory and inhibitory neurons during the plasticity period.

In STDP, the weight of a connection is modified depending on the time interval between pairs of pre- and post-synaptic spikes. For every pair, the weight of the synapse changes according to the following equations:

$$\Delta w(\Delta t) = \begin{cases} f_+(w)K_+(\Delta t) & \text{if } \Delta t \geq 0 \\ -f_-(w)K_-(\Delta t) & \text{if } \Delta t < 0 \end{cases} \quad (4.1)$$

where $\Delta t = t_{post} - t_{pre}$ is the time difference between the postsynaptic spike and the presynaptic one. The functions f_+ and f_- model the dependence of the weight change on the current value of the synaptic weights. K_+ and K_- are called STDP kernels which are usually decaying functions of time which reflects the fact that closer pre and post-synaptic spikes generate a stronger change in the weights. Usually, we model the kernels by a single exponential such as $K_+ = A_+ e^{-\frac{|\Delta t|}{\tau_{s+}}}$ and $K_- = e^{-\frac{|\Delta t|}{\tau_{s-}}}$. As it is evident from equation (4.1) when the postsynaptic neuron fires after the presynaptic neuron the strength of the connection increases and vice versa. We assume

the same type of the STDP rule for both inhibitory and excitatory connections although with different kernels. In the following, we suppose that the dependence of STDP on the synaptic weight is negligible and therefore replacing functions f_+ and f_- by a constant which is then absorbed to the kernels. In this case, we have to assume saturation level for the maximum strength of the synapses, w_{max}^E and w_{max}^I .

STDP changes synaptic weights on a very slow time scale compared to firing dynamics of the neurons, therefore, during a time period of $[t, t + \Delta t]$ where Δt is long in comparison with inter-spike time interval but small enough that the change in the weight w_{ij} of the synapse from neuron j to neuron i is infinitesimal, one can write down:

$$\begin{aligned} \Delta w_{ij} = & \int_t^{t+\Delta t} \int_0^{\text{inf}} S_j(s) S_i(s + \delta) f_+(w_{ij}) K_+(\delta) d\delta ds \\ & + \int_t^{t+\Delta t} \int_0^{\text{inf}} S_i(s) S_{out}(s - \delta) f_-(w_{ij}) K_-(\delta) d\delta ds \end{aligned}$$

Where $S_i(t)$ and $S_{out}(t)$ are the presynaptic and the postsynaptic neurons' spike trains. Assuming that during this period, the firing rate of the output neuron is constant on average and there exist many pre and post synaptic spikes, we can write down the mean change in the incoming synaptic weights to the neuron i as:

$$\begin{aligned} \frac{\langle \Delta w_{ij} \rangle_j}{\Delta T} = & \int_0^{\text{inf}} \langle S_j(s) S_i(s + \delta) \rangle_j K_+(\delta) d\delta \\ & - \int_0^{\text{inf}} \langle S_j(s) S_i(s - \delta) \rangle_j K_-(\delta) d\delta \end{aligned}$$

We want to investigate the evolution of the synaptic weights in the EI population in an asynchronous irregular state. Therefore, we assume that in the regime of the spontaneous activity neurons are firing as a Poisson process. Moreover, to estimate the cross-correlation of pre and post-synaptic spike train we would argue that the excitatory input to the cell has a positive correlation with preceding spikes in the target neuron. The magnitude of this excess correlation would depend on the weight of the synapse and it is restricted to the time window before the firing of the postsynaptic neurons. With this in mind, we use the following approximation introduced in Luz et al. and Van Rossum et al. [117, 118] for the cross-correlations of spike trains to account for the causal contributions of presynaptic spikes to the postsynaptic ones:

$$\begin{aligned}
\langle S_{pre}^E(s)S_{post}^E(s+\delta) \rangle &= r_{pre}^E r_{post} + r_{pre}^E w_i \gamma^E(\delta) \\
\langle S_{pre}^I(s)S_{post}^E(s+\delta) \rangle &= r_{pre}^I r_{post} - r_{pre}^I w_i \gamma^I(\delta)
\end{aligned} \tag{4.2}$$

As second terms in both equations encode the excess correlation(anticorrelation) of the presynaptic excitatory(inhibitory) input preceding the firing at the postsynaptic neuron, we set $\gamma^I = \gamma^E(\delta) = 0$ for $\delta < 0$. For positive values of δ , this function which is independent of the rates and the weights of the synapses encodes the causal effect of the presynaptic spike which arrives δ unit of time before firing of the postsynaptic neuron. Therefore, it is a decaying function of δ . Moreover, we have assumed the dependence on the weight of the synapse to be of a linear form, which is a good approximation in the regime of small synaptic weights.

Inserting the above approximation and labeling STDP kernels of EE and IE synapses as K^E and STDP kernels of II and EI synapses as K^I , we can write down the evolution of the average excitatory and inhibitory synaptic strength to the neuron i as:

$$\begin{aligned}
\frac{d\langle w_{ij}^E \rangle}{dt} &= \langle r_j^E \rangle r_i (\bar{K}_+^E - \bar{K}_-^E) + \langle r_j^E \rangle \langle w_{ij}^E \rangle \bar{K}_+^E \gamma^E \\
\frac{d\langle w_{ik}^I \rangle}{dt} &= \langle r_k^I \rangle r_i (\bar{K}_+^I - \bar{K}_-^I) - \langle r_k^I \rangle \langle w_{ik}^I \rangle \bar{K}_+^I \gamma^I
\end{aligned}$$

Here, bars denote integrals of the kernels on the positive or negative real lines. In the population of sparsely connected and sufficiently homogeneous neurons, in terms of the number of connections of each neuron, and the regime of asynchronous homogeneous firing state, i.e all the neurons fire with the same average rate but with a random phase of firing among them, average weights evolve as :

$$\begin{aligned}
\frac{dw_{EE}}{dt} &= r_E^2 \hat{K}^E + r_E w_{EE} K_+^{\bar{E}} \gamma^E \\
\frac{dw_{EI}}{dt} &= r_E r_I \hat{K}^I - r_I w_{EI} K_+^{\bar{I}} \gamma^I \\
\frac{dw_{IE}}{dt} &= r_E r_I \hat{K}^E + r_E w_{IE} K_+^{\bar{E}} \gamma^E \\
\frac{dw_{II}}{dt} &= r_I^2 \hat{K}^I - r_I w_{II} K_+^{\bar{I}} \gamma^I
\end{aligned} \tag{4.3}$$

From the above equations, it is straightforward to see when $\hat{K}^E := \bar{K}_+^E - \bar{K}_-^E < 0$ and $\bar{K}^I := \bar{K}_+^I - \bar{K}_-^I > 0$, the stationary solutions satisfy :

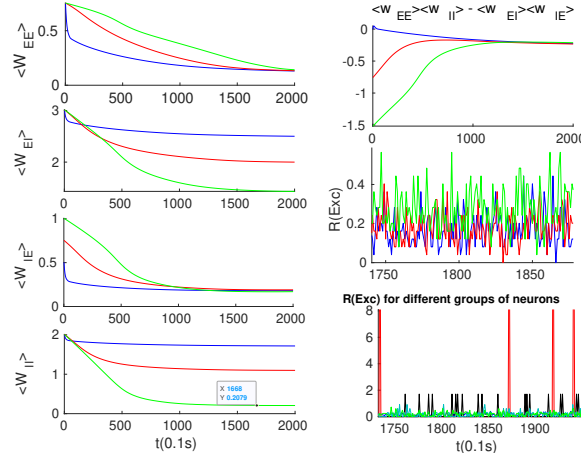


FIGURE 42. Effect of the synaptic plasticity on the network with three different initial weight configurations. (Left plots) Evolution of the average synaptic weights by STDP. (Top-Right) Change in the balance condition by STDP. Slopes of the Exc. and the Inh. nullclines approach each other under STDP in all three configurations. (Middle right) The final state of the average neuron firing rates for these three networks lies below 1Hz. (Bottom-right) Network activity for different clusters of neurons with different overall average inward synaptic weights. STDP results in clusters with different overall connectivity strengths and correspondingly different average rates.

$$\frac{w_{EI}^{st}}{w_{EE}^{st}} = \frac{\hat{K}^I \overline{K_+^E \gamma^E}}{\hat{K}^E \overline{K_+^I \gamma^I}} = \frac{w_{II}^{st}}{w_{IE}^{st}} \quad (4.4)$$

The above condition brings the slopes of the excitatory and the inhibitory nullclines close to each other leading to intersection in the semi-linear regime and proportionality of the excitation and the inhibition.

$$\frac{r_I^{st}}{r_E^{st}} \approx \frac{k_{EE} w_{EE}}{k_{EI} w_{EI}}$$

As the system lies around the BT point, a high amount of the synaptic plasticity occurs when neurons are in a higher (here the linear) firing regime. At this state, rates vary co-linearly as the above equation. On the other hand, synaptic plasticity rules for w_{II} and w_{EI} , i.e. second and fourth lines in equation (4.3), lead to a relation for stationary weights in the form of: $\frac{w_{II}}{w_{EI}} = \frac{r_I^{st}}{r_E^{st}}$. Comparing these last two equations, we arrive at $k_{EE} w_{EE}^{st} = k_{EI} w_{EI}^{st}$. Assuming $k_{II} = k_{EI}$, the mentioned relation adjusts

the trace of the Jacobian at the fixed point in the linear section to be near zero. Therefore, the plasticity rule in addition to the dynamics near-linear regime stabilizes the system near the BT point.

Fig.42 shows that STDP brings the network of EI populations to the avalanche regime. As STDP leads to an increase in the variance of weight distribution, some groups of the neurons become highly connected to the others while other groups show less overall connectivity strength. These groups of neurons will have different average rates as can be seen in Fig.42(Bottom Right).

4.2. Short-term plasticity and Up-Down states transition. Neurons' membrane potential in the spontaneous regime show transitions between up and down levels of depolarization. In the low state, the potential is close to the resting potential of the neuron and the firing rate is very low. On the other hand, in the up-state, the membrane potential stays closer to the threshold, and the neuron fires with rates of the order of few Herz to few tens of Herz. The mechanism that generates this bi-stability can be of an intrinsic and internal type such as non-linearity in the voltage-dependent synaptic current or can be originated from network dynamics. The switch between these bi-stable regimes might be due to the internal or the external noise or an adaptive mechanism that regulates the gain of the network. In the following, firstly, we discuss the adaptive role of short-term synaptic plasticity in bringing the network of EI population to the avalanche regime. Afterward, we will discuss how internal or external noise close to the BT point can also cause the switch between the quiescent(Down) and the low firing(UP) states. We will discuss that the Up-Down states' transition by short-term depression can be achieved either through a switch between bi-stable states or bringing the system close to the BT point by dampening the overall excitation.

In our model, short-term depression of the excitatory synapses reduces outgoing synaptic efficacy of excitatory synapses to an excitatory neuron in case of a high rate of presynaptic activity. To model the STP effect, we consider that the effective utility of the excitatory synapses of neuron j to the other neurons is proportional to the fraction of the available synaptic resources u . Decrease of neurotransmitters at the synapses and depression in release probability due to consecutive uses of neurotransmitters in previous spikes of the presynaptic neuron is the source of STP. We assume by each spike of presynaptic neuron u would reduce by the factor qu and then recovers with time constant τ_{STP} which is of order $100ms$ to few seconds. Therefore, synaptic efficacy of the postsynaptic synapse of neuron j evolves as:

$$\frac{du_j}{dt} = \frac{1}{\tau_{STP}}(1 - u_j) - qu_j \sum_k \delta(t - t_k^j) \quad (4.5)$$

Here, we just consider the short-term plasticity of synapses between excitatory to excitatory neurons. This type of plasticity might occur in other types of synapses as well, however, we would not discuss it here. Because there exist numerous input synapses and we have assumed homogeneous connectivity, each neuron senses a large sample of the network activity and is connected with an overall average weight with a small variance to the excitatory neuron pool. Based on these assumptions and structural homogeneity, we can write down the dynamic of the average synaptic weights to the neuron i in the state of the network with excitatory and inhibitory population firing rates of the magnitude ρ_E and ρ_I , respectively, as:

$$\frac{dw_{EE}}{dt} = \frac{w_{EE}^0 - w_{EE}(t)}{\tau_{STP}} - w_{EE}q\rho_E \quad (4.6)$$

Rate equations for the EI population are of the following form:

$$\begin{aligned} \frac{d\rho_E}{dt} &= -\frac{1}{\tau_m}(\rho_E(t) - f(\rho_E(t), \rho_I(t), w_{EE})) \\ \frac{d\rho_I}{dt} &= -\frac{1}{\tau_m}(\rho_I(t) - g(\rho_E(t), \rho_I(t))) \end{aligned}$$

Taking the time scale of short term plasticity to be much larger than the EI-network activity decay time constant, i.e. $\tau_{STP} \gg \tau_m$, we can rewrite the dynamic in terms of fast, d/dt^f and slow time d/dt^s evolution. Here, $t_f = t/\tau_m$ and $t_s = t/\tau_{STP}$. Defining $\mu = t_s/t_f$ and $\rho = \begin{pmatrix} \rho^E \\ \rho^I \end{pmatrix}$, we arrive at:

$$\begin{aligned} \frac{d\rho}{dt^f} &= -(\rho - f(\rho, w_{EE})) \\ \frac{dw_{EE}}{dt^f} &= \mu(w_{EE}^0 - w_{EE}) - q\tau_m w_{EE}\rho^E \end{aligned} \quad (4.7)$$

This set of equations can have a stable fixed point or an oscillatory behavior.

Average synaptic efficacy in the stationary state with the average excitatory rate ρ_E^* would be :

$$\langle W_{EE} \rangle_{St} = \frac{w_{EE}^0}{1 + \tau q \rho_E^*} \quad (4.8)$$

In case that there exist a fixed point or a stable limit cycle solution around this point in the $(\rho_E, \rho_I, \langle W_{EE} \rangle_{st})$ phase space, system might settle down at this solution (Fig.43-left). Dynamics of the EI population near

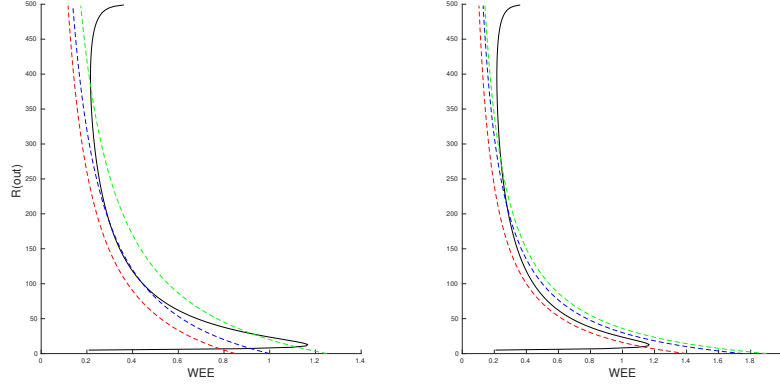


FIGURE 43. Output excitatory rates as a function of W_{EE} and the corresponding graphs for the average synaptic efficacy $\langle W_{EE} \rangle_{St}$ at three values of q (dashed red curve belongs the largest and dashed green curve is for the lowest value). Based on the value of W_{EE}^0 , two different scenarios can happen. In the left plot by decreasing q , through saddle-node bifurcation stable and unstable fixed points appear at low and high values of the rates. In the right plot, with higher W_{EE}^0 , by decreasing q after the Hopf bifurcation of low firing rate fixed point, oscillatory solution for (u, ρ_{out}) emerges.

this region ,(with slow-fast assumption) can be written as:

$$\begin{aligned} \rho_E^{st} &= f(k_{EE}\rho_E^{st}, k_{EI}\rho_I^{st}, \lambda_E^{Ex}, \lambda_I^{Ex}, \frac{w_{EE}^0}{1 + \tau q \langle \rho^{st} \rangle}) \\ \rho_I^{st} &= g(k_{EI}\rho_E^{st}, k_{II}\rho_I^{st}, \lambda_E^{Ex}, \lambda_I^{Ex}) \end{aligned} \quad (4.9)$$

This mechanism is shown to be effective to bring the system close to the BT point. Short synaptic plasticity is a method of gain control that can bring the system from a wide range of input and initial states to the low activity background state. In Fig.44, STP brings the system initially away from the BT point close to the avalanche regime. The average synaptic efficacy $\langle u \rangle$ in these cases does not oscillate significantly. In Fig.44, the network is in the parameter regime similar to the Fig.34 with $W_{EE}^0 = 0.56$ and four different values of ρ_{Ext} . Without STP, the system in the first three cases show a high firing rate oscillatory activity with an average rate of around $300Hz$.

STP brings all of them closer to the avalanche regime. Fig.45 shows excitatory and inhibitory stationary rates of the EI population subjected to external rates in the range $[200-500]Hz$. As it can be seen, STP leads to low firing rate states and prevents overactivation.

Fig.46(Left) shows avalanche size distribution in a log-log plot for the final state in the Fig.44 which shows avalanche. The slope of the linear regression line is very close to -1.5 . The branching ratio for the final state

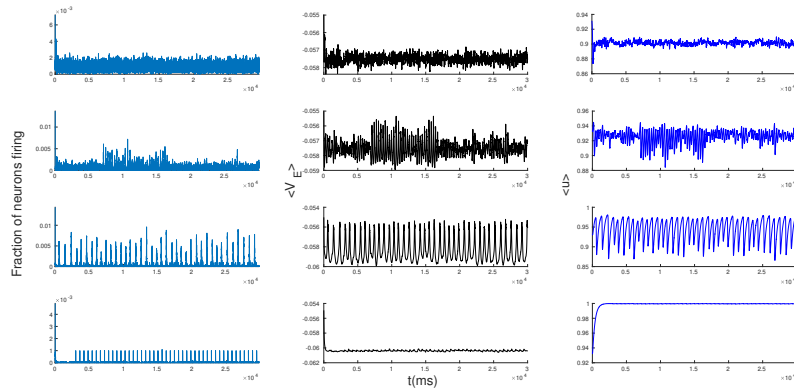


FIGURE 44. EI population with short term plasticity. $W_{EI} = 2, W_{II} = 1.5, W_{IE} = 0.75, W_{EE}^0 = 0.55$ $\rho_{Ext}^{inh} = 150\text{Hz}$ and $\rho_{Ext}^{exc} = [380, 280, 240, 180]\text{Hz}$. STP parameters are: $q = 0.3, \tau_{STP} = 10 * \tau_{syn}$. Top panel is the system with the highest external input rate and the bottom panel is the one with the lowest. Left plots are the excitatory population rates, middle plots are the population average membrane potential and right plots are the average excitatory synaptic efficacy $\langle u \rangle$.

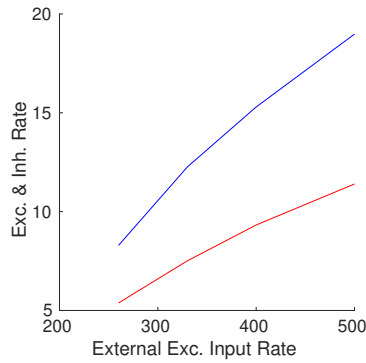


FIGURE 45. The final excitatory (red) and inhibitory (blue) output rates for the system in Fig.44. STP works as a gain control mechanism.

of the system is shown in Fig.46(Right). For $\rho_{Ext} = 240$, the branching ratio is slightly less than one which is in agreement with our prediction in the avalanche regime.

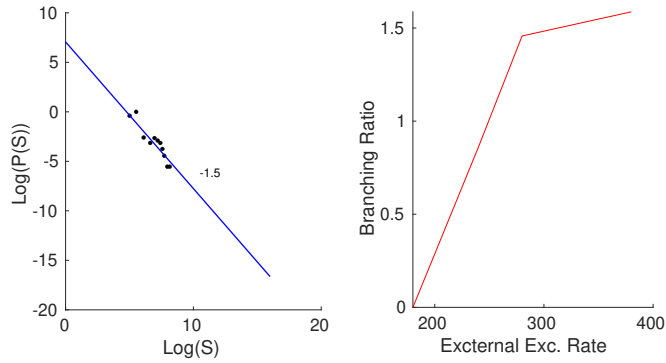


FIGURE 46. (Left)Avalanche size distribution in a log-log plot for the network in Fig.44 (Third Panel). (Right)Branching ratio in the network states shown in the Fig.44.

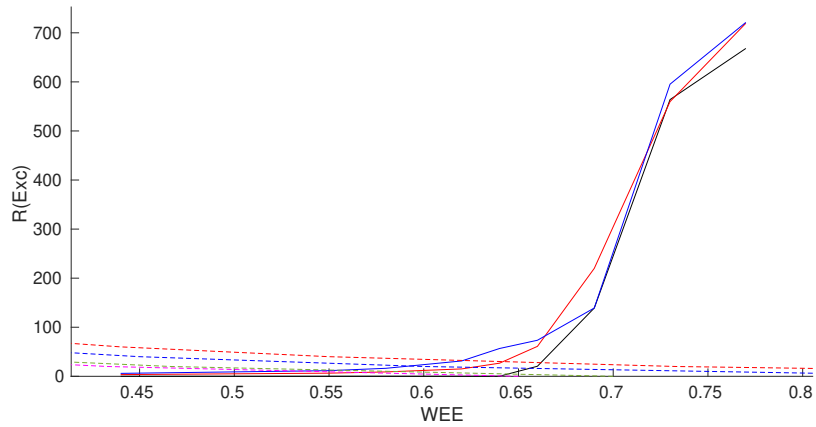


FIGURE 47. Solid curves are the output rates for three different external input strengths vs. W_{EE} : Blue ($400Hz$), red ($310Hz$), and black ($220Hz$). Dashed curves are average stationary synaptic weight, $\langle W_{EE} \rangle$, in the network with STP with different maximum synaptic efficacies: $W_{EE}^0 = 1.3$ (red) , 0.9 (blue), 0.7 (green), and 0.65 (magenta). Intersections of the dashed and the solid curves are the fixed points of the EI network with STP for the corresponding control parameters. These fixed points are located in the low firing rate regime close to the avalanche region(see Fig.40).

Moreover, Fig.47 shows final output rates in the case of a stable fixed point for u for three different values of the external Excitatory rates and W_{EE}^0 .

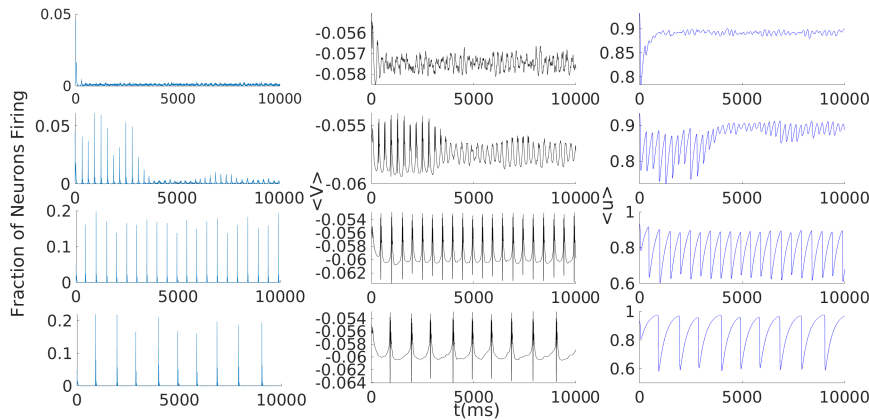


FIGURE 48. EI population with short term plasticity. Network parameters are : $W_{EI} = 2, W_{II} = 2, W_{IE} = 0.75, W_{EE}^0 = 0.74, \rho_{Ext}^{inh} = 150$ Hz, $\rho_{Ext}^{exc} = [400, 330, 270, 225]$ Hz and STP parameters are: $q = 0.4, \tau_{STP} = 10 * \tau_{syn}$. Left plots are the excitatory rates, middle plots are the average membrane potential and right plots are the average synaptic efficacy $\langle u \rangle$.

Another way that STP can cause a switch between two distinct firing states is in the EI population which possesses bi-stability. In this case change of u can make each of the bi-stable nodes unstable while the system resides near them. Decrease of u in the up-state makes the Up-state fixed point unstable at some value of $u(t)$ (and accordingly w_{EE}). Therefore, the system will jump to the remaining stable fixed point in a low or quiescent state. In the very low firing regime (the quiescent state), u will recover to its asymptotic value, and average synaptic weight increases towards w_{EE}^0 . If the quiescent state is unstable when u approaches its maximum value, we observe a transition to the high state. Moreover, if the volume of the basin of attraction of the quiescent fixed point is small, external and internal noise can also induce the transition to the high rate fixed point and the quiescent fixed point doesn't need to become unstable at w_{EE}^0 . For high values of u , the up-state fixed point is the stable point of the fast system but an unstable point of the slow one. Therefore, following the slow path up-state loses stability and the fast system remains with only a stable low fixed point. The trajectory of the slow u would be oscillatory in this case.

Fig.48 shows both ways that STP can produce synchronous avalanche behavior in the system. When $W_{EE} = w^0$, the system is close to the constraints on the alignment of the semi-linear segments of the EI-nullclines which results in the presence of a high firing state as a unique fixed point of the system. In the high input rate case, ($\rho_{Ext} = 400$ Hz, corresponding to the top panel of Fig.48 and Nullcline diagram of Fig.49(Left), due to

STP, the system moves from a high state of activity to a limit cycle solution in lower firing rates. This final state is shown in Fig.48 top panel and nullclines arrangements in this state are depicted in Fig.49(Right). Here, there is an unstable source in the linear branch sector which is surrounded by a limit cycle. Moreover, oscillations in $\langle u \rangle$ have a low amplitude because of the temporal averaging. On the other hand, the two bottom panels in Fig.48 are related to the situation of switch between the high fixed point and the quiescent node. As it is shown in nullclines graphs in Fig.50, at high synaptic efficacy in the left diagram, high firing state is the only stable fixed point, however, high firing rate results in a fast decline of the synaptic efficacy which brings the system to the state with nullcline map of the right plot in Fig.50 which has a stable quiescent fixed point. The final state activity, in this case, is composed of avalanches with a high rate of firing in the short window of an avalanche. Decreasing the q factor can result in a longer up-state period. Also, $\langle u \rangle$ oscillates between two limits in these cases.

In this particular case, necessary conditions for up to down transition are:

$$k_{EE}W_{EE}^0 > k_{EI}W_{EI} \quad (4.10)$$

$$k_{EE} \frac{w_{EE}^0}{1 + \tau q \rho^H} < k_{EI}W_{EI}$$

The first condition is related to the slope of the excitatory nullcline being smaller than the inhibitory one, which indicates a stable high firing fixed point. The second condition states that at this high firing state the stationary weight is not accessible before a stability loss. The slope of nullcline increases by the decrease of effective W_{EE} which causes the high state to lose stability either through Hopf bifurcation or saddle-node bifurcation.

Finally, the second top panel in Fig.48 is related to the case where STP brings the system close to the BT point that shows low to medium size avalanches with higher variability.

To sum up, transition from a quiescent state to a high firing state can be of two distinct nature. One way is that by increasing W_{EE} , the LF fixed point and the unstable saddle move toward each other and in this way the basin of attraction of the LF fixed point shrinks and noise can initiate the escape from this fixed point to the high firing state. The other way is that fixed point loses stability through Hopf bifurcation either before or after the emergence of a saddle-node in the middle branch.

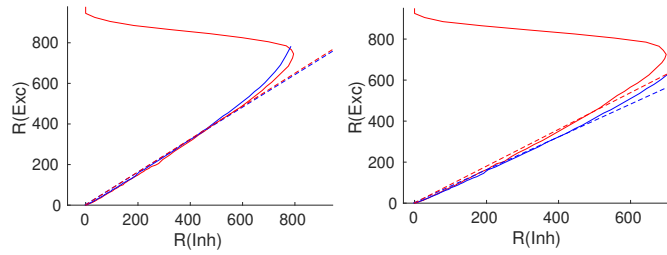


FIGURE 49. Nullclines plot for the system with the parameters same as Fig.48 top panel. (Left) Corresponding to the system before STP with $W_{EE} = 0.74$. (Right) The nullcline map after STP makes the high fixed point unstable and lower down average effective Exc.-Exc. synaptic weights ($\langle W_{EE} \rangle$).

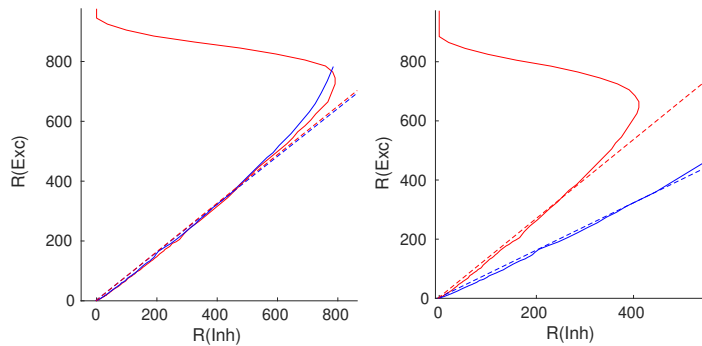


FIGURE 50. Nullclines plot for the system with parameters same as in Fig.48-Bottom. (Left) Here, $W_{EE} = 0.74$ which corresponds to the system being at the Up-state when the synaptic efficacy is fully recovered. (Right) The nullcline map in the Down-state with low synaptic efficacy.

5. Interconnected network of EI populations :Wilson-Cowan Neural Field Model

The model of Wilson and Cowan for the dynamics of the Spatio-temporal mean fields of the excitatory and the inhibitory population rates, $E(x, t)$ and $I(x, t)$ in a 2D model of the cortex was introduced in the '70s. In this

model at each point x , $E(x, t)$ is the density of the active neurons at time t in a sphere of radius Γ around x . Take a as the average distance between a neuron and its neighbors and ξ as the correlation length of the activity of neurons. Selecting $a \ll \Gamma < \xi$ guarantees that $E(x, t)$ is well defined and the number of neurons in each block is large enough to take the limit over the size of local population. $E(x, t)$ is defined as :

$$E(x, t) = \lim_{N \rightarrow \infty} \frac{n_{active}(x, t)}{N}$$

Considering a high number density of neurons, we assume that fluctuations in the number of the active neurons around this mean value are negligible. Furthermore, to derive the dynamics of this field we have to write down the input-output relation for each population of neurons at position x . In the mean-field approximation, we assume that each neuron receives the same input, which implies that each neuron is connected to all other neurons, and the weights of connections depend only on the distance $x - x'$ between two neurons. This can be a valid approximation if the connections between adjacent neurons are dense and the heterogeneity in the network structure is minimal. Now, assuming that neurons in each population would relax to the non-active state in the absence of input with relaxation constant τ , in general one can consider the following equation for the activity field $E(x, t)$:

$$\tau \frac{dE(x, t)}{dt} = -E(x, t) + (k_e - r_e E(x, t)) * S_e(i_E(x, t)) \quad (5.1)$$

$i_E(x, t)$ is the input to the excitatory population at x at time t which consists of both inhibitory and currents from both the self-activity of neurons in the population and other neurons in the adjacent population. S_e is a nonlinear input-output function that generally would depend on the response of the individual neurons, distribution of the membrane voltage, and the heterogeneity in weights.

In the following just as in Landau Ginzburg modeling for phase transition, we will assume the field $E(x, t)$ and $I(x, t)$ are very small so we can perform an expansion in form of power series. Furthermore, since these are average fields, we would assume that they vary slowly and smoothly in space, therefore, we neglect fast fluctuations and write down a phenomenological model for the current to excitatory population as :

$$\begin{aligned}
i_E(x, t) &= \int_V E(x', t) w_{EE}(|x' - x|) + I(x', t) w_{EI}(|x' - x|) dV + i_E^{ext} \\
&= E(x, t) \int w_{EE} dV + \nabla E \cdot \int (x' - x) w_{EE}(|x' - x|) dV \\
&\quad + \frac{1}{2} \int (x' - x) H_E(x) (x' - x) w_{EE}(|x' - x|) dV \\
&\quad + I(x, t) \int w_{EI} dV + \nabla E \cdot \int (x' - x) w_{EI}(|x' - x|) dV \\
&\quad + \frac{1}{2} \int (x' - x) H_I(x) (x' - x) w_{EI}(|x' - x|) dV \\
&= 2\pi E(x, t) \int r w_{EE}(r) dr + 2\pi I(x, t) \int r w_{EI}(r) dr \\
&\quad + \pi \nabla^2 E \int r^3 w_{EE}(r) dr + \pi \nabla^2 I \int r^3 w_{EI}(r) dr + i_E^{ext}
\end{aligned}$$

we can expand S^E around $I_0^e = 2\pi E(x, t) \overline{r w_{EE}} + 2\pi I(x, t) \overline{r w_{EI}} + i_E^{ext}$ and write down :

$$\begin{aligned}
\tau \frac{\partial E(x, t)}{\partial t} &= -E(x, t) + \tag{5.2} \\
&\quad (k_e - r_e E(x, t)) [S^E(I_0^e) + \pi S_{I_0^e}^{E'} (\nabla^2 E \langle r^3 w_{EE} \rangle + \nabla^2 I \langle r^3 w_{EI} \rangle)]
\end{aligned}$$

The same equation holds for the inhibitory field by expanding S^I around $I_0^i = 2\pi E(x, t) \overline{r w_{IE}} + 2\pi I(x, t) \overline{r w_{II}} + i_I^{ext}$:

$$\begin{aligned}
\tau \frac{\partial I(x, t)}{\partial t} &= -I(x, t) \tag{5.3} \\
&\quad + (k_i - r_i I(x, t)) * (S^I(I_0^i) + \pi S_{I_0^i}^{I'} (\nabla^2 E \langle r^3 w_{IE} \rangle + \nabla^2 I \langle r^3 w_{II} \rangle))
\end{aligned}$$

Equations (5.2) and (5.3) are of the reaction-diffusion type for the inhibitory and the exciatory fields in a two dimensional space. Defining $V(x, t) = \begin{pmatrix} E(x, t) \\ I(x, t) \end{pmatrix}$, D as the diffusion matrix and $f : R^2 \rightarrow R^2$ as the gain function, one can rewrite above equations in this form:

$$\tau \frac{\partial V(x, t)}{\partial t} = D \nabla^2 V(x, t) + f(V(x, t)) \tag{5.4}$$

The ODE part of this equation is the dynamic of a single EI population. The corresponding low firing fixed point (E_0, I_0) is stable in a specific parameter regime. It usually loses stability either via a saddle-node or Hopf bifurcation which leads to either a region of bi-stability of low and high firing state or the emergence of oscillations. However, still far away from the bifurcation point since the diffusion matrix is not a scalar multiple

of identity the Turing instabilities can occur in the system. It means that the homogeneous state of $[E(x, t), I(x, t)] = [E_0, I_0]$ can become unstable. In other words, when the diffusion coefficients of the inhibition and the excitation are sufficiently different, the homogenous steady state becomes unstable because of the diffusion.

To see this, consider the above ODE has a homogeneous solution at $V_0 = [E_0, I_0]$, by linearization of the equation around the fixed point, i.e. $V(x, t) = V_0 + v(x, t)$ and plugging in the ansatz $v(x, t) = e^{ikx + \lambda(k)t}\psi$ we arrive at :

$$\begin{pmatrix} -D_{EE}K^2 + \partial_{E|V_0}f_E, -D_{EI}K^2 + \partial_{I|V_0}f_E \\ -D_{IE}K^2 + \partial_{E|V_0}f_I, -D_{II}K^2 + \partial_{I|V_0}f_I \end{pmatrix} \psi = \lambda\psi \quad (5.5)$$

Assume L to be the Jacobian of an isolated EI population rate equations at $K = 0$, then the condition for the stability of the fixed point reads as :

$$\begin{aligned} \partial_E f_E + \partial_I f_I &< 0 \\ \det(L) = \partial_E f_E \partial_I f_I - \partial_I f_E \partial_E f_I &> 0 \end{aligned} \quad (5.6)$$

For the occurrence of Turing instability at a critical k_c the eigenvalues $\lambda(k)$ which satisfies the characteristic equation below should become positive for some real value of k :

$$\lambda^2 + ((D_{EE} + D_{II})k^2 - (\partial_E f_E + \partial_I f_I)\lambda + R(k^2)) = 0 \quad (5.7)$$

with $R(k^2)$ defined as:

$$R(k^2) = \alpha k^4 - k^2(D_{EE}\partial_I f_I + D_{II}\partial_E f_E - D_{IE}\partial_I f_E - D_{EI}\partial_E f_I) + \det(L) \quad (5.8)$$

In which $\alpha := D_{EE}D_{II} - D_{EI}D_{IE}$. Since the coefficient of λ in the equation (5.7), i.e minus the sum of eigenvalues, is positive, the necessary condition for the turing instability is that $R(k^2) < 0$ for some k . When $\alpha > 0$, which is a fair assumption as the inhibitory connections are more local than excitatory ones, if $\beta := D_{EE}\partial_I f_I + D_{II}\partial_E f_E - D_{IE}\partial_I f_E - D_{EI}\partial_E f_I > 0$ then $R(K^2)$ can become negative. In general $\frac{\beta}{\alpha}$ should be positive and instability of the homogenous state occurs at value $k_0^2 = \frac{\beta}{2\alpha}$ for which $R(k)$ becomes zero for the first time. In the following, we consider the case of the local inhibitory connection and therefore, we take D_{II} and D_{EI} to be very small. Furthermore, we assume to be in the regime of positive α , i.e $D_{EE} > D_{IE}$ and $D_{II} \approx D_{EI} \ll D_{EE}$. With these assumptions, which are intuitively valid based on the connectivity structure in the cortex, the condition on positive β converts to :

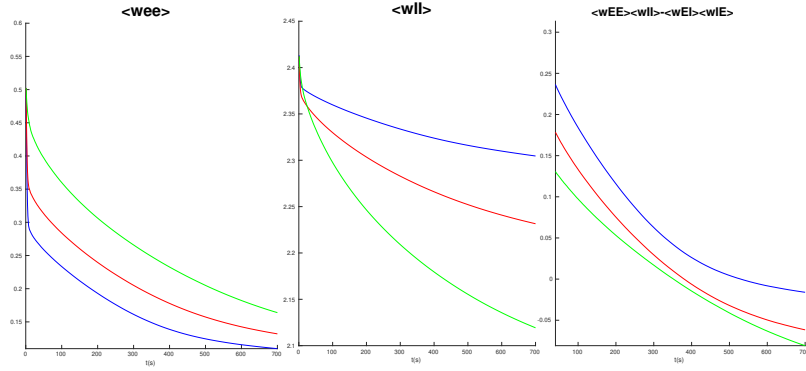


FIGURE 51. STDP changes values of connections' strengths in a way that sufficient conditions for emergence of Turing patterns, i.e. Eq.(5.10), are satisfied. (Left) $\langle W_{EE} \rangle$, (Middle) $\langle W_{II} \rangle$ and (Right) $W_{EE} | W_{II} | -W_{IE} | W_{EI} |$, for three different initial sets of values. Network's parameters evolve by STDP and at their final states satisfy conditions of Eq.(5.10).

$$D_{EE}\partial_I f_I - D_{IE}\partial_I f_E > 0$$

This holds when D_{IE} and $|\partial_I f_E|$ are sufficiently large which means the excess inhibition will produce a larger effect on the excitatory connection than the inhibitory one. This happens when the average stationary state potential distribution for neurons is close to the threshold, at which the effect of inhibition is larger than excitation. Therefore, conditions for Turing instability to occur are :

$$\begin{aligned} |\partial_I f_E| &> \frac{D_{EE}}{D_{IE}} |\partial_I f_I| & (5.9) \\ |\partial_I f_I| &> \partial_E f_E \\ \partial_E f_I &> \frac{\partial_E f_E |\partial_I f_I|}{|\partial_I f_E|} \end{aligned}$$

Considering the fact that D_{EE} and D_{IE} are proportional to W_{EE} and W_{IE} and the partial derivatives in the first approximations are equal to the average strength of connection, the necessary conditions for the Turing instability reduce to :

$$\begin{aligned} W_{IE} | W_{EI} | &> W_{EE} | W_{II} | & (5.10) \\ W_{EE} - | W_{II} | &< 0 \end{aligned}$$

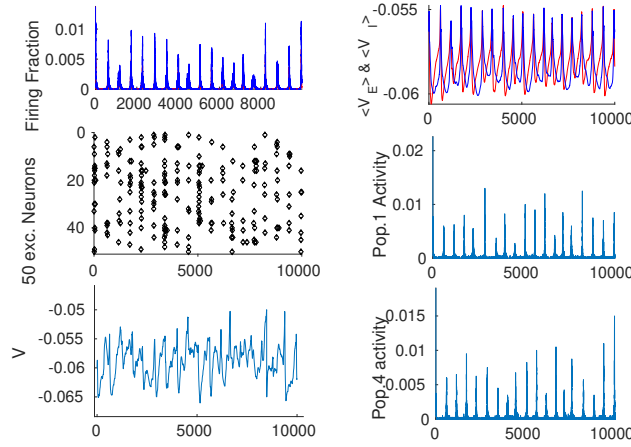


FIGURE 52. Simulation result of 20 interconnected EI populations each of size $N_E = 10000$ arranged on a ring. Average synaptic weights between two different EI subnetworks decays with the phase difference of them. Parameters of synaptic weights in each EI population are : $W_{EE} = 0.6$, $W_{EI} = 2, W_{II} = 2, W_{IE} = 0.75$, $\rho_{Ext}^E = 230Hz$ and $\rho_{Ext}^I = 150Hz$. (Top-Left) The average firing rate of the whole network. (Middle-Left) Raster plot of the subpopulation of 50 neurons in one single EI subnetwork. Although neurons fire at avalanche times, they don't fire in all of them, which leads to high variability in their interspike interval times. (Bottom-Left) The membrane potential of a single neuron, which is in a constant transition between a state closer to the threshold and a state close to the resting potential. (Top-Right) The average membrane potential of an EI-population (red for Exc. and blue for Inh.). (Middle and Bottom-right) The activity of two distinct EI subpopulation which shows high variability in sizes of avalanches in both of them.

As can be seen in Fig.51 and discussions at the end of section(4.1), synaptic plasticity rule of section (4.1) lead to the regime where above mentioned conditions are satisfied.

Moreover, taking $\partial_E f_I \propto W_{IE}$ and ρ_{ext} as the free parameters, one can obtain the boundary of the Turing instability region defined by $\min(R(k^2)) = 0$ at some value $k = k_c$. In this Turing instability region, stripe-like stationary patterns of activity with spatial frequencies close to $k = k_c$ appears in the system and the homogeneous solution becomes unstable.

Besides Turing instabilities, it can also happen that the fixed point itself loses its stability at $k = 0$ through Hopf bifurcation, where real part of the eigenvalues of L become zero:

$$\begin{aligned}\partial_E f_E + \partial_I f_I &= 0 \\ \det(L) = \partial_E f_E \partial_I f_I - \partial_I f_E \partial_E f_I &> 0\end{aligned}$$

Furthermore, exactly at the BT point, we would also have $\det(L) = 0$. Fig.52 shows the activity of 20 interconnected EI-populations each operating close to the BT point. Overall activity in this system is of synchronous avalanches type. Up-down state transitions also become synchronized. We can model weakly interconnected EI populations in the avalanche regime which shows oscillation of frequency ω_i as pulse-coupled oscillators and therefore investigate conditions on synchronization and traveling wave solutions. This analysis is out of the scope of the current work. Another approach is supplementing the macroscopic field equation with appropriate noise term to derive the mesoscopic equation. As can be seen from Fig.52, the overall network activity is of avalanche style. It is another evidence that avalanches are scale-free and occur in different temporal and spatial scales. However, our neural field model still lacks the internal finite-size fluctuation effects, inhomogeneities, and cross-correlation between individual neurons, and also inter-populations correlations.

6. Stochastic Neural Field

6.1. Finite size fluctuations in a single EI population. So far we have analyzed mean-field models which were based on neglecting finite system size, inhomogeneities in the synaptic connections, and stochastic effects. Far from bifurcations of the mean-field equations, the behavior of the average rates of the stochastic system follows predictions of MF accurately. In this case, basins of attractions of the fixed points are separated enough and stochastic effects do not lead to a change in the macroscopic behavior of the system. However, close to the bifurcation points of the macroscopic system, internal and external fluctuations can make the stochastic system evolve differently than predictions of MF models. For example, it can cause transitions between different fixed points.

Let us consider a homogeneous network in which temporal and spatial variances in the firing rates of neurons would be minimal. In this network, fluctuations in the finite system firing rates in the steady-state will be proportional to $O(\frac{1}{\sqrt{N}})$. To model the finite-size stochastic effects, we need to write down dynamics of micro-states evolution that match the mean-field upon coarse-graining. As we have seen, the operating region of the EI population is around a low firing state where neurons fire with high variability of inter-spike intervals indicating that we can model neurons' spiking as a Poisson process. In this regime of activity, the Poisson neuron assumption enables us to write down the microscopic evolution of a model neuron with two active and inactive states. Rate of active to inactive transition, α would model vanishing of the postsynaptic potentiation, and the rate of inactive to active transition depends on the input and is denoted by $f(i)$. We want to model the system in the statistical homogenous state, in which the probability that one neuron fires depend only on the number of active neurons and it is the same for every neuron in the population.

In the following, we consider population of N_E excitatory and N_I inhibitory neurons, in which neurons change their states independently. Let us take $P(E, I, t)$ as the probability density of the EI population being in a state with E number of active excitatory and I number of active inhibitory neurons at time t . The following master equation describes the microscopic evolution of the system :

$$\begin{aligned}
 \frac{\partial P(E, I, t)}{\partial t} = & -\alpha[(EP(E, I, t) + IP(E, I, t))] & (6.1) \\
 & + \alpha[(E + 1)P(E + 1, I, t) + (I + 1)P(E, I + 1, t)] \\
 & + (N_E - E + 1)f(\kappa_{EE}w_{EE}(E - 1), \kappa_{EI}w_{EI}I)P(E - 1, I, t) \\
 & - (N_E - E)f(\kappa_{EE}w_{EE}E, \kappa_{EI}w_{EI}I)P(E, I, t) \\
 & + (N_I - I + 1)g(\kappa_{IE}w_{EE}E, \kappa_{II}w_{EI}(I - 1))P(E - 1, I, t) \\
 & - (N_I - I)g(\kappa_{EE}w_{EE}E, \kappa_{EI}w_{EI}I)P(E, I, t)
 \end{aligned}$$

In which $\kappa_{xy} = \frac{K_{xy}}{N_x}$, with K_{xy} being the number of incoming connections to a neuron in the population x from the population y . In the following, we write down $c_{xy} = \kappa_{xy}w_{xy}$. We use the system size expansion method [119] for truncating moment hierarchy based on taking an ansatz on the order of the finite size fluctuation in the system. Assuming fluctuations around the deterministic (average field) trajectory to be of order $O(N)$, we can rewrite our stochastic variables in terms of a deterministic and a fluctuating term as:

$$\begin{aligned} E &= N_E \rho_E + N_E^{1/2} \epsilon \\ I &= N_I \rho_I + N_I^{1/2} i \end{aligned} \quad (6.2)$$

Defining $P(E, I, t) = Q(\epsilon, i, t)$, we can rewrite the l.h.s of the master equation in terms of the new parameters as :

$$\frac{\partial P(E, I, t)}{\partial t} = \frac{\partial(\epsilon, i, t)}{\partial t} - N_E^{1/2} \frac{d\rho_E(t)}{dt} \frac{\partial Q}{\partial \epsilon} - N_I^{1/2} \frac{d\rho_I(t)}{dt} \frac{\partial Q}{\partial i}$$

Defining ladder operators $Z_E f(E) = f(E+1)$ and $Z_E^{-1} f(E) = f(E-1)$ and expanding them in powers of ϵ , we arrive at:

$$Z_E = 1 + N_E^{-1/2} \frac{\partial}{\partial \epsilon} + \frac{1}{2} N_E^{-1} \frac{\partial^2}{\partial \epsilon^2} + \dots$$

$$Z_E^{-1} = 1 - N_E^{-1/2} \frac{\partial}{\partial \epsilon} + \frac{1}{2} N_E^{-1} \frac{\partial^2}{\partial \epsilon^2} + \dots$$

We define the same ladder operators for the inhibitory population states. Plugging all these equations into the master equation(6.1), we have:

$$\begin{aligned} &\frac{\partial Q(\epsilon, i, t)}{\partial t} - N_E^{1/2} \frac{d\rho_E(t)}{dt} \frac{\partial Q}{\partial \epsilon} - N_I^{1/2} \frac{d\rho_I(t)}{dt} \frac{\partial Q}{\partial i} = \\ &\alpha(Z_E - 1)[(N_E \rho_E + N_E^{1/2} \epsilon)Q(\epsilon, i, t)] \\ &+ (Z_E^{-1} - 1)[N_E(1 - \rho_E - N_E^{-1/2} \epsilon)f(c_{EE}N_E(\rho_E + N_E^{-1/2} \epsilon), c_{EI}N_I(\rho_I + N_I^{-1/2} i))Q(\epsilon, i, t)] \\ &+ \alpha(Z_I - 1)[(N_I \rho_I + N_I^{1/2} i)Q(\epsilon, i, t)] \\ &+ (Z_I^{-1} - 1)[N_I(1 - \rho_I - N_I^{-1/2} i)g(c_{IE}N_E(\rho_E + N_E^{-1/2} \epsilon), c_{II}N_I(\rho_I + N_I^{-1/2} i))Q(\epsilon, i, t)] \end{aligned} \quad (6.3)$$

Expanding the inactive to inactive transition rates as :

$$\begin{aligned} f(c_{EE}N_E(\rho_E + N_E^{-1/2} \epsilon), c_{EI}N_I(\rho_I + N_I^{-1/2} i)) &= f(c_{EE}N_E \rho_E, c_{EI}N_I \rho_I) + \\ &N_E^{-1/2} \frac{\partial f}{\partial \rho_E} \epsilon + N_I^{-1/2} \frac{\partial f}{\partial \rho_I} i + \dots \end{aligned}$$

Using the same expansion for ladder operators, we can sort the right and the left sides of (6.3) in powers of N_E and N_I . Equating terms of the order $O(N_E^{1/2})$ and $O(N_I^{1/2})$ leads to the macroscopic equation:

$$\begin{aligned} -\frac{d\rho_E(t)}{dt} &= \alpha\rho_E(t) - (1 - \rho_E(t))f(\kappa_{EE}w_{EE}N_E\rho_E, \kappa_{EI}w_{EI}\rho_I) \\ -\frac{d\rho_I(t)}{dt} &= \alpha\rho_I(t) - (1 - \rho_I(t))g(\kappa_{IE}w_{IE}N_I\rho_I, \kappa_{II}w_{II}\rho_I) \end{aligned}$$

Equating terms of order $O(N^0)$ leads to a linear FPE for $Q(\epsilon, i, t)$ of the following form:

$$\begin{aligned} \frac{\partial Q(\epsilon, i, t)}{\partial t} &= (\alpha - (1 - \rho_E))\frac{\partial f}{\partial \rho_E} + f)\frac{\partial}{\partial \epsilon}\epsilon Q \\ &+ (\alpha - (1 - \rho_I))\frac{\partial g}{\partial \rho_I} + f)\frac{\partial}{\partial i}i Q \\ &- (1 - \rho_E)\frac{\partial f}{\partial \rho_I}\frac{\partial}{\partial \epsilon}i Q \\ &- (1 - \rho_I)\frac{\partial g}{\partial \rho_E}\frac{\partial}{\partial i}\epsilon Q \\ &+ \frac{1}{2}(1 - \rho_E)f\frac{\partial^2}{\partial \epsilon^2}Q + \frac{1}{2}(1 - \rho_I)g\frac{\partial^2}{\partial i^2}Q \end{aligned}$$

Defining matrices A and B as :

$$\begin{aligned} \begin{pmatrix} A_{11} & A_{12} \\ A_{21} & A_{22} \end{pmatrix} &= \begin{pmatrix} -\alpha + (1 - \rho_E)\frac{\partial f}{\partial \rho_E} - f & (1 - \rho_E)\frac{\partial f}{\partial \rho_I} \\ (1 - \rho_I)\frac{\partial g}{\partial \rho_E} & -\alpha + (1 - \rho_I)\frac{\partial g}{\partial \rho_I} - g \end{pmatrix} \\ B &= \begin{pmatrix} (1 - \rho_E)f & 0 \\ 0 & (1 - \rho_I)g \end{pmatrix} \end{aligned}$$

The amplitude of fluctuating term evolves as :

$$\frac{\partial}{\partial t} \begin{pmatrix} \langle \epsilon \rangle \\ \langle i \rangle \end{pmatrix} = \begin{pmatrix} A_{11} & A_{12} \\ A_{21} & A_{22} \end{pmatrix} \begin{pmatrix} \langle \epsilon \rangle \\ \langle i \rangle \end{pmatrix} \quad (6.4)$$

And the covarianc matrix $C = \begin{pmatrix} \langle \langle \epsilon^2 \rangle \rangle & \langle \langle \epsilon i \rangle \rangle \\ \langle \langle \epsilon i \rangle \rangle & \langle \langle i^2 \rangle \rangle \end{pmatrix}$ satisfies :

$$\frac{\partial}{\partial t} C = AC + CA^t + B \quad (6.5)$$

If the determinant of matrix A is positive and its trace is negative at the stationary point of the macroscopic equation (i.e. A has two negative eigenvalues), then the averages of fluctuation terms go to zero. At the stationary point of the macroscopic equation, we would have :

$$\begin{pmatrix} A_{11} & 0 & A_{12} \\ 0 & A_{22} & A_{21} \\ A_{21} & A_{12} & A_{11} + A_{22} \end{pmatrix} \begin{pmatrix} \langle\langle \epsilon^2 \rangle\rangle_{st} \\ \langle\langle i^2 \rangle\rangle_{st} \\ \langle\langle \epsilon i \rangle\rangle_{st} \end{pmatrix} = -\frac{\alpha}{2} \begin{pmatrix} \rho_E^{st} \\ \rho_I^{st} \\ 0 \end{pmatrix}$$

which has the following solution :

$$\begin{aligned} \langle\langle \epsilon^2 \rangle\rangle_{st} &\approx c((A_{11}A_{22} - A_{21}A_{12} + A_{22}^2)\rho_E + A_{12}^2\rho_I) \\ \langle\langle i^2 \rangle\rangle_{st} &\approx c((A_{11}A_{22} - A_{21}A_{12} + A_{11}^2)\rho_I + A_{21}^2\rho_E) \\ \langle\langle \epsilon i \rangle\rangle_{st} &\approx -c(A_{11}A_{12}\rho_I + A_{21}A_{22}\rho_E) \end{aligned} \quad (6.6)$$

$$\text{with } c = \frac{-\alpha}{2(A_{11} + A_{22})(A_{11}A_{22} - A_{21}A_{12})}.$$

Average population rate and fluctuation around the macroscopic state are as follows:

$$\begin{aligned} \langle \frac{E}{N_E} \rangle &= \rho_E & \langle\langle \frac{E}{N_E} \rangle\rangle &= \frac{\langle\langle \epsilon^2 \rangle\rangle}{N_E} \\ \langle \frac{I}{N_I} \rangle &= \rho_I & \langle\langle \frac{I}{N_I} \rangle\rangle &= \frac{\langle\langle i^2 \rangle\rangle}{N_I} \end{aligned} \quad (6.7)$$

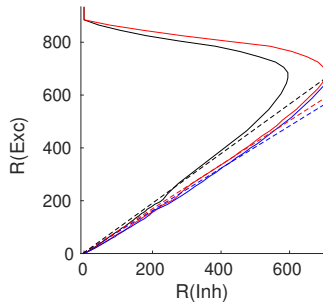


FIGURE 53. Nullclines graphs for the system with parameters: $W_{EI} = 2, W_{II} = 1.5, W_{IE} = 0.75, \rho_{Ext}^I = 150Hz, \rho_{Ext}^E = 280Hz, w_{EE} = 0.53$ (red) and 0.48 (black). Blue curve is the inhibitory nullcline and dashed lines are linear approximations of the corresponding nullclines. Both excitatory nullclines have intersection with the inhibitory nullcline in the semi-linear section.

From equation (6.7), it can be seen that close to the bifurcation of the macroscopic equation, i.e. the BT point, where both trace and determinant of the Jacobian are close to zero, magnitudes of fluctuations increase. Exactly at the bifurcation point, the mentioned system size expansion fails because the average of the noise term is unbounded, therefore, we cannot assume fluctuating term in equation (6.2) to be of order $N^{1/2}$. Figures (53-55) show characteristics of an EI population activity in the Poisson regime. Fig.53 is the nullcline graph related to two different strengths of W_{EE} both of them adjusting the system to have a stable fixed point on the semi-linear part of the nullclines. The one with a higher W_{EE} has a higher firing rate fixed point. Fig.54 shows how the average and the variance of the membrane potential, the average rates, and the inter-spike intervals' CV follow the prediction that neurons fire with Poisson statistics, asynchronously and independently. Dashed lines in Fig.54 are the approximation based on considering neurons to fire with Poisson statistics and independently with the same rates that we observe in the simulation of the network. Dashed lines in the bottom-left plot show the rate approximation based on considering the membrane potential distribution as Gaussian with the mean and the variance as predicted in the top panel. Fig.55 shows the variance and the covariance of the excitatory and the inhibitory rates in the simulation match the values derived from the microscopic model discussed above, i.e. equations (6.6) and (6.7).

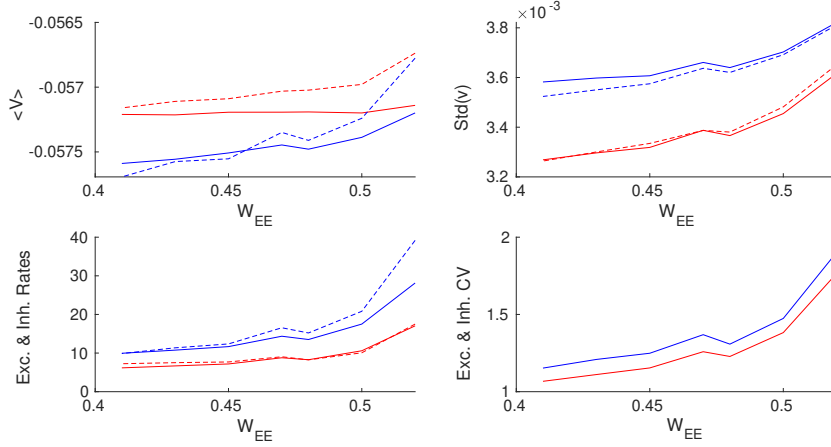


FIGURE 54. Characteristics of the network activity for systems with weight parameters as in Fig.42 with $W_{EE} \in [0.41, 52]$. Red curves show excitatory quantities and blue is for inhibitory ones. Dashed lines are the prediction from the Poisson assumption and solid lines are the simulation results. (Top-Left) Average membrane potential. (Top-Right) The standard deviation of the membrane potential. (Bottom-Left) Output rates. Here, dashed lines are the firing rates derived from the Gaussian approximation of the potential distribution based on values of the average and the variance of the membrane potential in the top panel of this figure. (Bottom-Right) Interpike intervals' CV in the simulation.

6.2. Stochastic Neural Field with a Tuning Mechanism to the Critical State. We have considered that the inhibition effect in the network is local and we have seen that the system is tuned in a way that the inhibitory feedback in the local EI population balances the average excitatory current in a way that neurons' firing is fluctuation driven. Consider the effect of the inhibitory current to be instantaneous, we can use proportionality of excitatory and inhibitory current to write down rate dynamics of the excitatory population in terms of stochastic field equation when both inhibitory feedback and fluctuations are local. From equation (3.18), we know that near the BT point, there is a linear relation between rates, i.e $I \approx \frac{k_{EE}W_{EE}}{k_{EI}W_{EI}}E$. Therefore, the average current to the excitatory population close to the BT point can be written as $\epsilon = k_{EE}W_{EE}E - k_{EI}W_{EI}I \approx 0$. Second derivative in the expansion of gain function for the excitatory population from equation (5.4) in the region of low activity is :

$$\frac{1}{2} \frac{\partial^2 f}{\partial E^2} E^2 + \frac{\partial^2 f}{\partial EI} EI + \frac{1}{2} \frac{\partial^2 f}{\partial I^2} I^2$$

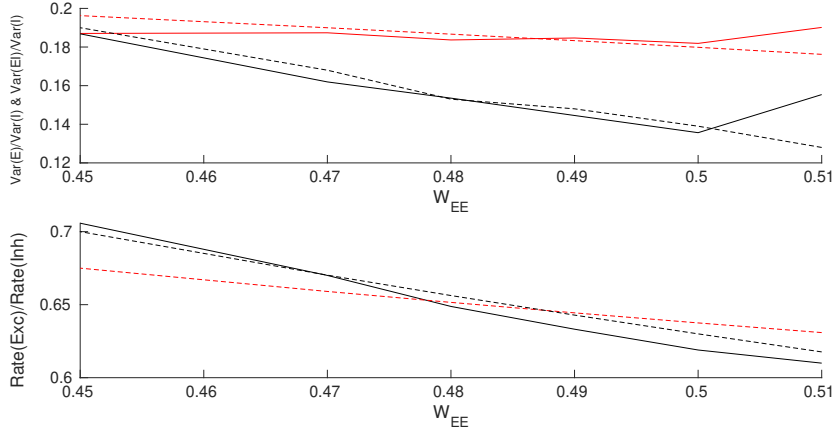


FIGURE 55. (Top) ratio of $\text{var}(E)$ to $\text{var}(I)$ (red) and $\text{var}(EI)$ to $\text{var}(I)$ (black) in the stationary state of the above mentioned systems. Dashed lines are the approximation derived from the Poisson assumption and solid lines are the simulation results of the spiking neuron network. (Bottom) The ratio of the excitatory to the inhibitory stationary rates varies vs. W_{EE} . Dashed line is $\frac{k_{EI}W_{EI}}{k_{EE}W_{EE}}$ and the solid line is the simulation result.

With following approximations for the gain function derivatives:

$$\begin{aligned}\frac{\partial^2 f}{\partial I^2} &\propto W_{EI}^2 \\ \frac{\partial^2 f}{\partial E^2} &\propto W_{EE}^2 \\ \frac{\partial f}{\partial I \partial E} &\propto -W_{EE}W_{EI}\end{aligned}$$

Using the proportionality relation of inhibitory and excitatory rates in the above equations and the fact that fluctuations in the average population activity, Eq.(6.7), is linearly dependent on the rate, we can write down stochastic field equation for excitatory rate in the region of small ϵ :

$$\begin{aligned}\frac{\partial E(x, t)}{\partial t} &= \epsilon E(x, t) + D\Delta E(x, t) - |u|E^2(x, t) + \psi(x, t) \quad (6.8) \\ \langle \psi(x, t)\psi(x', t') \rangle &= 2\sigma\sqrt{\frac{1}{N}}E(x, t)\delta(x - x')\delta(t - t')\end{aligned}$$

Here $u < 0$ is the coefficient related to synaptic weights that can be explicitly derived by assuming a certain form of the gain function and proportionality of the rates. This stochastic partial differential equation after

appropriate rescaling $E(x, t) = \frac{\sigma}{|u|\tau} S(x, t)$ agrees with the Langevin description of directed percolation introduced in the introduction and is rewritten below:

$$\begin{aligned} \frac{\partial S(x, t)}{\partial t} &= (-\epsilon' + D'\Delta)S(x, t) - u'S^2(x, t) + \psi(x, t) \\ &< \psi(x, t)\psi(x', t') > = 2u'S(x, t)\delta(x - x')\delta(t - t') \end{aligned} \quad (6.9)$$

At $\epsilon' = 0$, the above system shows an absorbing state phase transition. Thus, from any active state system relaxes by avalanches with a power-law size distribution to an inactive state.

In an isolated EI population, external drive to the inhibitory and the excitatory population should be present to counterbalance the dissipation by the leaking currents and therefore, sets average membrane potential in these neurons at a state above the resting threshold. The aforementioned Taylor expansion is performed around this point. External excitatory input to the excitatory population is slightly higher than the external drive to the inhibitory population which leads to slightly higher average membrane potential in the excitatory population. Furthermore, we can assume that the external spike train to each neuron is Poisson as well. The external drive itself would not lead to significant firing in the individual neurons but the strengths of the internal connections between them are tuned in a way that bursts of activity occur in the excitatory population which is then followed by the inhibitory ones. The internal feedback inhibition is strong enough to kill the excitatory burst. In a slightly inhibition-dominated regime, we have sharp synchronous responses to the external input in a short time window. On the other hand, the network has a safe margin from an overly active state. In the absence of the input distinguished from random external noise, the system shows scale-free avalanches because of the maintenance of the inhibition-excitation balance.

However, the external drive must compensate for the dissipation for the system to be at the critical point. Without mechanisms like short-term plasticity, the external drive should be fine-tuned for the system to show criticality. However, short-term plasticity in a network in which synaptic weights are already near slightly inhibition dominated regime broadens the range of the external drive strength which leads to critical avalanches. We can extend the model in the section (4.2) to a continuum field equation by defining a field of excitatory synaptic efficacy $\Omega(x, t) \propto \langle W_{EE} \rangle(x, t)$ with local dynamics of equation (4.6) :

$$\tau_m \frac{\partial E(x, t)}{\partial t} = (-\alpha + \Omega(x, t))E(x, t) + D\Delta E(x, t) - |u|E^2(x, t) + \psi(x, t) \quad (6.10)$$

$$\frac{\partial \Omega(x, t)}{\partial t} = \frac{1}{\tau_{STP}}(\Omega^0 - \Omega) - q\Omega E(x, t)$$

$$\langle \psi(x, t)\psi(x', t') \rangle = 2\sigma \sqrt{\frac{1}{N}} E(x, t)\delta(x - x')\delta(t - t')$$

Here α represents both the decay of the activity by leaky currents of the cells and the inhibition feedback which varies linearly with the excitatory rate. Dynamic excitatory synaptic strength brings the coefficient of the linear term to a value near zero. To see this, assume this set of equations have a stationary synaptic efficacy solution of the following value:

$$\Omega_{st} = \frac{\Omega^0}{1 + q\tau_{STP}E_{st}}$$

On the other hand in the active phase, stationary homogeneous rate is:

$$E_{st} = \frac{-\alpha + \Omega_{st}}{|u|}$$

Assuming $|u|$ is a very small quantity and E_{st} is also small in the low firing rate regime then $-\alpha + \Omega_{st} \approx 0$ and $E_{st} = \frac{1}{q\tau_{STP}}\left(\frac{\Omega^0}{\alpha} - 1\right)$.

Long-term synaptic plasticity tune Ω^0 so that the coefficient of the linear term is close to zero and moderate value of short-term depression would be adequate to bring the system to the critical point. Altogether, equation (6.10) is the description of an EI interconnected spiking neurons network tuned to the critical point of balancing inhibition and excitation both by long-term synaptic plasticity and short-term synaptic depression. System wanders around the phase transition point and shows avalanche dynamics with scale-free size and time distributions, the proportionality of inhibition and excitation, up and down states transition of membrane potential and population activity rates, and oscillation of order of $10Hz$ resembling ubiquitous alpha-band oscillation.

7. Conclusion

In this work, we have proposed a self-organizing model for the cortical dynamics which tunes the system to the regime of low firing avalanche dynamics corresponding to the ongoing intrinsic activity in the cortex. We have seen that in a large sparse network of spiking neurons the input to the cells in the state of asynchronous firing is Poisson and investigated conditions on Poisson firing at the single neuron level. We chose the conductance-based leaky integrate and fire model to take the strong dependence of inhibitory postsynaptic current on voltage level into consideration. Next, we introduced linearization of the neuron gain function in the Poisson firing regime and presented a linear Poisson neuron model which we used to analyze interconnected networks of the excitatory and the inhibitory neurons.

The network of spiking neurons with the assumption of homogeneity, large size, and sparse connectivity can be modeled by the dynamics of the mean fields. Excitatory and Inhibitory mean-field equations are a set of nonlinear equations with free parameters among them the average synaptic strength between different types of neurons. Taking a set of these free parameters as control parameters of the model one can analyze the bifurcation patterns in the system. We took the excitatory external drive and the synaptic weight between excitatory to excitatory neurons as control parameters. The latter regulates the strength of the inhibitory feedback in the local population and the former controls the level of forced activity from other populations. The qualitative picture of the bifurcation patterns does not change by the choice of different synaptic weights as the control parameter. In analyzing the bifurcation diagram, our interest is mainly focused on the loss of the stability of the quiescent state. This can happen through saddle-node or Hopf bifurcation by either increasing external drive or W_{EE} . At a certain point called Bogdanov-Takens point, saddle-node and Hopf bifurcation lines meet each other. We have seen that near this point there is a tight balance of the inhibitory and the excitatory average currents to the cells. This balance cancels out the high amplitude excitatory and inhibitory currents to each cell to a great portion and results in the average membrane potential of the neurons in the population being adequately away from the threshold. In this regime, the activity of the spiking neurons is fluctuation driven which makes the firing time intervals highly variable. In this case, the statistics of the firing would be close to the Poisson Point process matching the experimental findings. On the other hand, the balance of excitation and inhibition leads to the avalanche style dynamics near the BT point. Slow oscillations emerge at the Hopf bifurcation line and through saddle-node bifurcation, a pair of low firing stable and unstable fixed points come into existence. We showed that long-term synaptic plasticity tunes the synaptic weights to achieve the internal balance of inhibition and excitation. On the other hand, short-term synaptic depression would lead to tuning the system for the wide range of the strength of the external drive.

In the vicinity of the bifurcation point, fluctuation effects are manifested strongly and mean-field solutions would not adequately describe the dynamics. Especially internal and external noises which were neglected in the mean-field analysis would lead to state transitions in the proximity of the saddle-node line. On the other hand, in the vicinity of the Hopf bifurcation line, fluctuations lead to higher variability in the amplitude of avalanches. In the vicinity of the BT point, by analyzing the linear stability of the quiescent fixed point, slow dynamics can be projected to the nonlinear stable manifold. We wrote down dynamics in terms of the excitatory field only by assuming a fast linear inhibitory feedback. The dynamical equation for the excitatory field matches the description of directed percolation. At the balance line, the coefficient of the linear term in the field equation vanishes which puts the system at the critical point of the percolation phase transition. In a system with dissipation external load has to be fine-tuned to compensate for the dissipation to be at the critical point. Short-term depression of excitatory synapses allows this tuning for a wider range of external drives.

Bibliography

- [1] Klaus Linkenkaer-Hansen, Vadim V. Nikouline, J. Matias Palva and Risto J. Ilmoniemi *Long-Range Temporal Correlations and Scaling Behavior in Human Brain Oscillations*, Journal of Neuroscience 15 February 2001
- [2] Kai J. Miller ,Larry B. Sorensen,Jeffrey G. Ojemann,Marcel den Nijs *Power-Law Scaling in the Brain Surface Electric Potential*, PLoS computational Biology 2009
- [3] Richard Hardstone, Simon-Shlomo Poil, Giuseppina Schiavone, Rick Jansen, Vadim V. Nikulin, Huibert D. Mansvelder and Klaus Linkenkaer-Hansen *Detrended fluctuation analysis: a scale-free view on neuronal oscillations*, Front. Physiol., 30 November 2012
- [4] Manfred G. Kitzbichler,Marie L. Smith,Søren R. Christensen,Ed Bullmore *Broadband Criticality of Human Brain Network Synchronization*, PLoS computational Biology 2009
- [5] Dong-Ping Yang ,Hai-Jun Zhou,Changsong Zhou *Co-emergence of multi-scale cortical activities of irregular firing, oscillations and avalanches achieves cost-efficient information capacity*, PLoS Comput Biol . 2017
- [6] C M Gray , P König, A K Engel, W Singer *Oscillatory responses in cat visual cortex exhibit inter-columnar synchronization which reflects global stimulus properties*, Nature,1989.
- [7] Daido H, *Onset of cooperative entrainment in limit-cycle oscillators with uniform all-to-all interactions: Bifurcation of the order function*, Physica D Nonlinear Phenomena ,March 1996
- [8] Daido H, *A solvable model of coupled limit-cycle oscillators exhibiting partial perfect synchrony and novel frequency spectra*, Physica D Nonlinear Phenomena,December 1993.
- [9] Gong P, Nikolaev AR, van Leeuwen C *Scale-invariant fluctuations of the dynamical synchronization in human brain electrical activity.*, Neuroscience Letters, 01 Jan 2003
- [10] Christian Meisel, Eckehard Olbrich, Oren Shriki and Peter Achermann *Fading Signatures of Critical Brain Dynamics during Sustained Wakefulness in Humans*, Journal of Neuroscience 30 October 2013
- [11] Steriade, M., Timofeev, I. and Grenier, F. *Natural waking and sleep states: a view from inside neocortical neurons*. J. Neurophysiol. 85, 1969–1985 (2001).
- [12] Thomas T G Hahn, Bert Sakmann and Mayank R Mehta *Phase-locking of hippocampal interneurons' membrane potential to neocortical up-down states* Nature Neuroscience(2006).
- [13] Maria V. Sanchez-Vives, and David A. McCormick *Cellular and network mechanisms of rhythmic recurrent activity in neocortex* Nature Neuroscience(2000).
- [14] Compte A, Sanchez-Vives MV, McCormick DA, Wang XJ *Cellular and network mechanisms of slow oscillatory activity (~ 1 Hz) and wave propagations in a cortical network model*. J Neurophysiol 89(2003).
- [15] Rosa Cossart, Dmitriy Aronov and Rafael Yuste *Attractor dynamics of network UP states in the neocortex*, Nature volume 423, pages283–288(2003)
- [16] Kenet T, Bibitchkov D, Tsodyks M, Grinvald A, Arieli A *Spontaneously emerging cortical representations of visual attributes.*, Nature 425: 954–956(2003)

- [17] Lampl I, Reichova I, Ferster D *Synchronous membrane potential fluctuations in neurons of the cat visual cortex.*, Neuron 22,1999.
- [18] Deco G, Marti D, Ledberg A, Reig R, Sanchez-Vives MV *Effective reduced diffusion-models: a data driven approach to the analysis of neuronal dynamics.*, PLoS Comput Biol,2009.
- [19] Daniel Jercog , Alex Roxin, Peter Bartho, Artur Luczak, Albert Compte, Jaime de la Rocha *UP-DOWN cortical dynamics reflect state transitions in a bistable network* , eLife, 2017.
- [20] David Holcman ,Misha Tsodyks *The Emergence of Up and Down States in Cortical Networks*, Plos Computational Biology, 2006
- [21] Daniel Millman, Stefan Mihalas, Alfredo Kirkwood and Ernst Niebur *Self-organized critical neural networks*, Nature Physics volume 6, pages801–805(2010)
- [22] Elisa M. Tartaglia and Nicolas Brunel *Bistability and up/down state alternations in inhibition-dominated randomly connected networks of LIF neurons*, Scientific Reports volume 7, Article number: 11916 (2017)
- [23] Néstor Parga, and Larry F. Abbott. *Network Model of Spontaneous Activity Exhibiting Synchronous Transitions Between Up and Down States*, Front Neurosci. 2007
- [24] John M. Beggs and Dietmar Plenz. *Neuronal Avalanches in Neocortical Circuits*, Journal of Neuroscience,2003.
- [25] Thomas Petermann, Tara C. Thiagarajan, Mikhail A. Lebedev, Miguel A. L. Nicolelis. *Spontaneous cortical activity in awake monkeys composed of neuronal avalanches*, PNAS September 15, 2009.
- [26] Tiago L. Ribeiro, Mauro Copelli, Fábio Caixeta, Hindiael Belchior, Dante R. Chialvo, Miguel A. L. Nicolelis, Sidarta Ribeiro *Spike Avalanches Exhibit Universal Dynamics across the Sleep-Wake Cycle*, PLoS one,2010.
- [27] Gerald Hahn , Thomas Petermann, Martha N Havenith, Shan Yu, Wolf Singer, Dietmar Plenz, Danko Nikolic *Neuronal avalanches in spontaneous activity in vivo*, J Neurophysiol,2010.
- [28] Nir Friedman, Shinya Ito, Braden A. W. Brinkman, Masanori Shimono, R. E. Lee DeVille, Karin A. Dahmen, John M. Beggs, and Thomas C. Butler *Universal Critical Dynamics in High Resolution Neuronal Avalanche Data*, Phys. Rev. Lett. 108,2012.
- [29] Alberto Mazzoni ,Frédéric D. Broccard ,Elizabeth Garcia-Perez ,Paolo Bonifazi, Maria Elisabetta Ruaro, Vincent Torre *On the Dynamics of the Spontaneous Activity in Neuronal Networks*, PLoS one ,2007.
- [30] Andreas Klaus , Shan Yu, Dietmar Plenz *Statistical analyses support power law distributions found in neuronal avalanches*, PLoS One,2011 .
- [31] Yahya Karimipannah , Zhengyu Ma , Jae-Eun Kang Miller , Rafael Yuste , Ralf Wessel. *Neocortical activity is stimulus- and scale-invariant*, PLoS One , 2017.
- [32] Christian Tetzlaff , Samora Okujeni, Ulrich Egert, Florentin Wörgötter, Markus Butz *Self-organized criticality in developing neuronal networks*, PLoS Comput Biol . 2010
- [33] Per Bak,Chao Tang kurt Wiesenfeld *Self-organized criticality*, Physical review A(1988).
- [34] Henrik Jeldtoft Jensen, Kim Christensen, and Hans C. Fogedby *If noise, distribution of lifetimes, and a pile of sand*, Phys. Rev. B 40, (1991).
- [35] S.Manna *Critical exponents of the sand pile models in two dimensions*, Physica A (1991).
- [36] S Zapperi, Bakgaard Lauritsen K, HE Stanley *Self-organized branching processes: Mean-field theory for avalanches*, Phys Rev Lett . 1995
- [37] Per Bak and Chao Tang *Mean field theory of self organized critical phenomena*, Journal of Statistical Physics volume 51, pages797–802(1988).
- [38] G. Grinstein *Generic scale invariance in classical nonequilibrium systems* , Journal of Applied Physics 69, 5441 (1991)

- [39] Juan A Bonachela, Sebastiano de Franciscis, Joaquín J Torres and Miguel A Muñoz *LaTeX: Self-organization without conservation: are neuronal avalanches generically critical?*, Journal of Statistical Mechanics: Theory and Experiment, Volume 2010, February 2010
- [40] Juan A Bonachela and Miguel A Muñoz *Self-organization without conservation: True or just apparent scale-invariance?*, Journal of Statistical Mechanics: Theory and Experiment, 2009.
- [41] Alessandro Vespignani, Ronald Dickman, Miguel A. Muñoz, and Stefano Zapperi *Driving, Conservation, and Absorbing States in Sandpiles*, Phys. Rev. Lett. 81 (1998)
- [42] Ronald Dickman, Alessandro Vespignani and Stefano Zapperi. *Self-organized criticality as an absorbing-state phase transition*, Phys. Rev. E 57, 1998.
- [43] Ronald Dickman , Miguel A. Muñoz , Alessandro Vespignani and Stefano Zapperi *Paths to Self-Organized Criticality*, Brazilian Journal of Physics 30, 27 (2000).
- [44] M. Doi, *Second quantization representation for classical many-particle systems*, J. Phys. A, 9 (1976), pp. 1465–1477.
- [45] L. Peliti, *Path integral approach to birth-death processes on a lattice*, J. Phys., 46 (1985),
- [46] H.K. Janssen, *Renormalized Field-Theory of Dynamical Percolation*, Z. Phys. B: Cond. Mat. 58, 311 (1985).
- [47] H.K. Janssen, *On the Non-Equilibrium Phase-Transition in Reaction-Diffusion Systems with an Absorbing Stationary State*, Z. Phys. B: Cond. Mat. 42, 151 (1981).
- [48] H Hinrichsen, *Non-equilibrium critical phenomena and phase transitions into absorbing states*, Advances in physics, 2000
- [49] Á Corral, CJ Pérez, A Díaz-Guilera, A Arenas *Self-organized criticality and synchronization in a lattice model of integrate-and-fire oscillators*, Phys Rev Lett . 1995
- [50] S. Bottani *Pulse-Coupled Relaxation Oscillators: From Biological Synchronization to Self-Organized Criticality*, Phys Rev Lett . 1995
- [51] Christian W. Eurich, J. Michael Herrmann, and Udo A. Ernst *Finite-size effects of avalanche dynamics*, Phys. Rev. E 66, 2002
- [52] Daniel B. Larremore, Marshall Y. Carpenter, Edward Ott and Juan G. Restrepo *Statistical properties of avalanches in networks*, Physical Review E, 2012.
- [53] Levina, Anna; Herrmann, J. Michael and Geisel, Theo. *Phase Transitions towards Criticality in a Neural System with Adaptive Interactions*, Physical Review Letters, vol. 102, 2009
- [54] Levina, Anna; Herrmann, J. Michael and Geisel, Theo. *Dynamical synapses causing self-organized criticality in neural networks* , Nature Physics volume 3(2007)
- [55] Jiayi Peng, John M. Beggs *Attaining and maintaining criticality in a neuronal network model*, Physica A: Statistical Mechanics and its Applications, 2013
- [56] Serena di Santo, Pablo Villegas, Raffaella Burioni, and Miguel A. Muñoz *LaTeX: A Landau–Ginzburg theory of cortex dynamics: Scale-free avalanches emerge at the edge of synchronization*, PNAS February 13, 2018
- [57] Stefan Bornholdt, Torsten Roehl *Self-organized criticality occurs in non-conservative neuronal networks*, Phys. Rev. E 67 (2003)
- [58] Matthias Rybarsch, Stefan Bornholdt *Avalanches in Self-Organized Critical Neural Networks: A Minimal Model for the Neural SOC Universality Class* PLoS One , 2014.
- [59] Christian Meisel, Thilo Gross *Adaptive self-organization in a realistic neural network model*, Physical Review Letters, vol. 102, 2009
- [60] Ludmila Brochini, Ariadne de Andrade Costa, Miguel Abadi, Antônio C. Roque, Jorge Stolfi and Osame Kinouchi *Phase transitions and self-organized criticality in networks of stochastic spiking neurons*, Scientific Reports volume 6 (2016)

- [61] Marc Benayoun ,Jack D. Cowan,Wim van Dronghelen,Edward Wallace *Avalanches in a Stochastic Model of Spiking Neurons* PLoS One , 2010.
- [62] Z Olami, HJS Feder, K Christensen *Self-organized criticality in a continuous, non-conservative cellular automaton modeling earthquakes*, Physical review letters 68 (8), 1992.
- [63] B Drossel, F Schwab *Self-organized critical forest-fire model*, Physical review letters, 1992
- [64] P. Grassberger, *Critical Behaviour of the Drossel-Schwabl Forest Fire Model*, New J. Phys. 4, 17 (2002)
- [65] J. X. de Carvalho and C. P. C. Prado, *Self-Organized Criticality in the Olami-Feder-Christensen model*, Phys. Rev. Lett. 84, 4006 (2000).
- [66] N Brunel , V Hakim *Fast global oscillations in networks of integrate-and-fire neurons with low firing rates*, Neural Comput, 1999.
- [67] N Brunel *Dynamics of Sparsely Connected Networks of Excitatory and Inhibitory Spiking Neurons* , Journal of Computational Neuroscience 8, 183–208 (2000)
- [68] Nicolas Brunel , Vincent Hakim *Sparsely synchronized neuronal oscillations*, chaos,2008
- [69] D. H. Hubel and T. N. Wiesel *Receptive fields, binocular interaction and functional architecture in the cat's visual cortex*, J. Neurosci., 3 (1962)
- [70] H R Wilson, J D Cowan *Excitatory and inhibitory interactions in localized populations of model neurons*, Biophys J, 1972.
- [71] H R Wilson, J D Cowan *A mathematical theory of the functional dynamics of cortical and thalamic nervous tissue*, Kybernetik volume 13, pages55-80(1973)
- [72] S Amari *Dynamics of pattern formation in lateral-inhibition type neural fields*, Biol Cybern . 1977
- [73] Pinto D and Ermentrout G B *Spatially structured activity in synaptically coupled neuronal networks:Traveling fronts and pulses* , SIAM J. Appl. Math. 62 206–25,2001
- [74] Troy W C and Shusterman V *Patterns and features of families of traveling waves in large-scale neuronal networks* SIAM J. Appl. Dyn. Syst. 6 263–92,2007
- [75] Pinto D and Ermentrout G B *Spatially structured activity in synaptically coupled neuronal networks:Lateral inhibition and standing pulses*, SIAM J. Appl. Math. 62 206–25,2001
- [76] Ermentrout G B and Cowan *A mathematical theory of visual hallucination patterns* Biol. Cybern. 34 137–50,1979
- [77] Bard Ermentrout *Neural networks as spatio-temporal pattern-forming systems*, Reports on Progress in Physics, Volume 61,1998.
- [78] PC Bressloff *Spatiotemporal dynamics of continuum neural fields*, Journal of Physics A: Mathematical and Theoretical 45,2011.
- [79] Iris Ginzburg and Haim Sompolinsky *Theory of correlations in stochastic neural networks*, Phys. Rev. E 50, 1994.
- [80] C. van Vreeswijk, H. Sompolinsky *Chaos in Neuronal Networks with Balanced Excitatory and Inhibitory Activity*, Science, 1996.
- [81] C. van Vreeswijk, H. Sompolinsky *Chaotic balanced state in a model of cortical circuits*, Neural Comput, 1998.
- [82] C. Meyer and C. van Vreeswijk, *Temporal correlations in stochastic networks of spiking neurons*, Neural Comput., 14 (2002), pp. 369–404.
- [83] J.Touboul,G.Hermann And O. Faugeras *LaTeX: Noise-Induced Behaviours in Neural Mean Field Dynamics*, SIAM Journal on Applied Dynamical Systems, Volume 11, Issue 1, 2015.
- [84] H. Soula and C. C. Chow *Stochastic dynamics of a finite-size spiking neural network*, Neural Comput., 19 (2007), pp. 3262–3292.

- [85] Michael A Buice , Jack D Cowan *Field-theoretic approach to fluctuation effects in neural networks* Phys Rev E Stat Nonlin Soft Matter Phys,2007.
- [86] PC Bressloff *Stochastic neural field theory and the system-size expansion* SIAM J. Appl. Math,2000.
- [87] L. Peliti, *Stochastic neural field model of stimulus-dependent variability in cortical neurons*, PLoS One , 2019.
- [88] D Cowan, J Neuman, B Kiewiet and W van Drongelen *Self-organized criticality in a network of interacting neurons* J. Stat. Mech. (2013) .
- [89] Softky, W R and Koch, C *The highly irregular firing of cortical cells is inconsistent with temporal integration of random EPSPs.*, The Journal of Neuroscience 1993
- [90] Shu, Y, Hasenstaub, A and McCormick, D A *Turning on and off recurrent balanced cortical activity* The Journal of Neuroscience 2003
- [91] Haider, B; Duque, A Hasenstaub, A R and McCormick, D A *Neocortical network activity in vivo is generated through a dynamic balance of excitation and inhibition.*, The Journal of Neuroscience 2006
- [92] Haider, B Häusser, M and Carandini, M *Inhibition dominates sensory responses in the awake cortex*, Nature, 2013.
- [93] M. Okun, I. Lampl *Instantaneous correlation of excitation and inhibition during ongoing and sensory-evoked activities*, Nat. Neurosci., 11 (2008).
- [94] T P Vogels , H Sprekeler, F Zenke, C Clopath, W Gerstner *Inhibitory plasticity balances excitation and inhibition in sensory pathways and memory networks*, science.1211095, 2011.
- [95] Ashok Litwin-Kumar And Brent Doiron *Slow dynamics and high variability in balanced cortical networks with clustered connections*, Nature Neuroscience volume 15, 2012.
- [96] Paolo Moretti And Miguel A. Muñoz *Griffiths phases and the stretching of criticality in brain networks*, Nature Communications volume 4, 2013.
- [97] Jheng-Jun Wang and Changsong Zhou *Hierarchical modular structure enhances the robustness of self-organized criticality in neural networks*, New Journal of Physics, Volume 14, February 2012
- [98] Paolo Massobrio, Valentina Pasquale And Sergio Martinoia *Self-organized criticality in cortical assemblies occurs in concurrent scale-free and small-world networks*, Scientific Reports volume 5, 2015.
- [99] Mikail Rubinov ,Olaf Sporns,Jean-Philippe Thivierge,Michael Breakspear *Neurobiologically Realistic Determinants of Self-Organized Criticality in Networks of Spiking Neurons*, PLoS Comput Biol,2011.
- [100] Wesley Cota, Géza Ódor And Silvio C. Ferreira *Griffiths phases in infinite-dimensional, non-hierarchical modular networks*, Scientific Reports volume 8, 2018.
- [101] Woodrow L. Shew, Hongdian Yang, Thomas Petermann, Rajarshi Roy and Dietmar Plenz *Neuronal Avalanches Imply Maximum Dynamic Range in Cortical Networks at Criticality*, Journal of Neuroscience 9 December 2009
- [102] Woodrow L. Shew, Hongdian Yang, Shan Yu, Rajarshi Roy and Dietmar Plenz *Information Capacity and Transmission Are Maximized in Balanced Cortical Networks with Neuronal Avalanches*, Journal of Neuroscience 5 January 2011,
- [103] Hongdian Yang, Woodrow L. Shew, Rajarshi Roy and Dietmar Plenz *Maximal Variability of Phase Synchrony in Cortical Networks with Neuronal Avalanches*, Journal of Neuroscience 18 January 2012,
- [104] Simon-Shlomo Poil, Richard Hardstone, Huibert D. Mansvelder and Klaus Linkenkaer-Hansen *Critical-State Dynamics of Avalanches and Oscillations Jointly Emerge from Balanced Excitation/Inhibition in Neuronal Networks*, Journal of Neuroscience 18 July 2012

- [105] F Lombardi , H J Herrmann , L de Arcangelis *Calance of excitation and inhibition determines 1/f power spectrum in neuronal networks*, Chaos,2017.
- [106] Nicholas M. Timme, I, Najja J. Marshall, Nicholas Bennett, Monica Ripp, Edward Lautzenhiser, and John M. Beggs. *Criticality Maximizes Complexity in Neural Tissue*, Front Physiol. 2016
- [107] Viola Priesemann , Michael Wibral , Mario Valderrama , Robert Pröpper , Michel Le Van Quyen , Theo Geisel , Jochen Triesch , Danko Nikolić , Matthias H J Munk *Spike avalanches in vivo suggest a driven, slightly subcritical brain state*, Front Syst Neurosci . 2014
- [108] Viola Priesemann ,Oren Shriki *Can a time varying external drive give rise to apparent criticality in neural systems?*, PLoS Comput Biol . 2018
- [109] Matteo Martinello, Jorge Hidalgo, Amos Maritan, Serena di Santo, Dietmar Plenz, and Miguel A. Muñoz *Neutral Theory and Scale-Free Neural Dynamics* Phys. Rev. X 7,2017
- [110] Pablo Villegas, Serena di Santo, Raffaella Burioni, Miguel A. Muñoz *Time series thresholding and the definition of avalanche size*, Phys. Rev. E 100, 012133 (2019)
- [111] Jonathan Touboul and Alain Destexhe *Power-law statistics and universal scaling in the absence of criticality* , Phys. Rev. E 95,19
- [112] Alain Destexhe and Jonathan D. Touboul *Is There Sufficient Evidence for Criticality in Cortical Systems?*, ENEURO.2021
- [113] Wulfram Gerstner, Richard Naud, Liam Paninski *Neuronal Dynamics From Single Neurons to Networks and Models of Cognition* , Cambridge University Press,2014.
- [114] Arnold J. F. Siegert *On the First Passage Time Probability Problem*, Phys. Rev. 81, 617 –1951.
- [115] R M Borisyuk, A B Kirillov *Bifurcation analysis of a neural network model*, Biol Cybern . 1992.
- [116] Gerstner, W., Kempter R., van Hemmen J.L., and Wagner H. *A neuronal learning rule for sub-millisecond temporal coding.*, Nature, 386:76-78. (1996).
- [117] Yotam Luz , Maoz Shamir *The Effect of STDP Temporal Kernel Structure on the Learning Dynamics of Single Excitatory and Inhibitory Synapses*, PLoS Comput Biol, 2010.
- [118] M. C. W. van Rossum, G. Q. Bi and G. G. Turrigiano *Stable Hebbian Learning from Spike Timing-Dependent Plasticity*, Journal of Neuroscience 1 December 2000.
- [119] N.G Van Kampen *Stochastic Processes in Physics and Chemistry*, A volume in North-Holland Personal Library Book, Third Edition, 2007.

Bibliographische Daten

Self-organized Criticality in Neural Networks
by Inhibitory and Excitatory Synaptic Plasticity
(Selbstorganisierte Kritikalität in neuronalen Netzwerken
durch inhibitorische und exzitatorische synaptische Plastizität)

Ehsani, Masud

Universität Leipzig, Dissertation, 2021

122 Seiten, 55 Abbildungen, 119 Referenzen

Daten zum Autor

Name:	Masud Ehsani
Geburtsdatum:	01.07.1990 in Mashhad, Iran
10/2008 - 10/2013	Studium der Elektrotechnik (B. Sc.) Universität Scharif-Universität für Technologie Teheran, Iran
10/2013 - 1/2016	Studium der Physik (M. Sc.) Universität Scharif-Universität für Technologie Teheran, Iran
seit 02/2017	Doktorand Max-Planck-Institut für Mathematik in den Naturwissenschaften Leipzig, Germany